

DELFT UNIVERSITY OF TECHNOLOGY

FACULTY OF ELECTRICAL ENGINEERING, MATHEMATICS & COMPUTER SCIENCE
MSc SUSTAINABLE ENERGY TECHNOLOGY

MASTER THESIS PROJECT

Aerodynamic Design Optimization of Floating Wind Turbines for In Situ Hydrogen Production

Ioannis Voultzos
Student Number: 5347742

Project Duration:
November 2021-July 2022

Thesis Committee:
Prof. dr. Dominic Von Terzi (Chairman & Supervisor)
As. Prof. dr. Riccardo Ferrari (Committee)
ir. Ricardo Elisbao Martins Amaral (Daily Supervisor)
ir. Mihir Mehta (Daily Supervisor)

July 13, 2022

Preface

This report is written as fulfillment of my thesis project in order to obtain the degree of Master of Science in Sustainable Energy Technology at the Delft University of Technology. Over the course of the project, I enriched my knowledge on various technical topics and useful software packages, which will be essential for my future career.

I would like to thank my supervisor, Dominic Von Terzi for his guidance during my thesis project. In particular, being at his supervision for nine months, gave me the opportunity to work on a such an interesting topic and useful for my career in the years to come. At the same time, the knowledge I obtained from him during our meetings, broadened my horizons on various technical topics.

Moreover, I would like to express my regards on my PhD supervisors, Ricardo Amaral and Mihir Mehta. I was pleased by the cooperation with both, because I admired their way of guiding me to understand the topic and to take decisions. In particular, I enjoyed the learning process they used, according to which, they subtly lead me take decisions in a methodical and knowledge-enriching way.

In addition, sincere thanks to my girlfriend, Catherine, who supported me during the project and was always free to hear my thoughts and to give me an alternative in difficult times.

Last but not least, I feel the need to thank my family for their love and support over my educational years. They were available whenever I need them and did their best for me.

Delft, July 13, 2022

Ioannis Voultos

Summary

The energy transition towards carbon neutrality requires a rapid electrification of all energy sectors by 2050. In the EU-27, the REPowerEU strategy, initiated in March 2022, is pursuing this target even more ambitiously. However, in order to achieve the aforementioned goals, the increasing demand for green hydrogen will cause an increase of the renewable energy needs as early as 2030. In this way, offshore wind can be a solid supplier of the renewable energy for green hydrogen production. However, since nearly 80% of the worldwide wind energy potential is situated in deep waters, floating offshore wind turbines (FOWT) can be used to cover those energy needs. In addition, the literature review showed that when green hydrogen production via FOWT is considered, the most economically and energy efficient layout is the in situ topology, where hydrogen is locally produced on the FOWT.

Although FOWT and green hydrogen production via FOWT have been lately examined in literature, a literature gap was found. More specifically, no attention was given on the performance change of a turbine when it is adapted from a bottom fixed (BF) application to a FOWT. Also, the effect of the in situ hydrogen plant to the FOWT performance was not considered. Thus, the aim of this project is to highlight if FOWT for in situ hydrogen production should be aerodynamically redesigned to improve their performance or to tackle possible energy losses. In this direction, several sub-questions should be answered, including the selection of turbine, floater type and site to be investigated, the effect of the floater design on the FOWT performance, the performance change of a turbine due to its adaptation as FOWT and the effect of the added mass of the hydrogen plant on the FOWT performance. Lastly, in case of a proven FOWT performance deterioration, solutions should be provided so as to regain performance.

Aligned with the previous goals, the IEA 15 MW reference wind turbine on top on the UMaine Voltorn US-S semi-submersible floater is simulated in OpenFAST under steady and turbulent wind fields, according to wind & wave conditions of a typical US East Coast site. In addition, the in situ hydrogen plant is incorporated in the model using a simplified approach. The results suggest that in the whole partial load region, the FOWT experiences power losses due to the static floater pitch angle, which reduces the inflow wind speed seen by the rotor. However, between 9 and 12 m/s, a peak shaving routine is incorporated in the FOWT controller, which results in early power shedding and contributes, together with the static floater pitch, to considerable power losses. Furthermore, the simulations conducted using the OpenFAST FOWT model, which incorporated the hydrogen plant, suggest that it has a negligible effect on the FOWT performance and can be omitted from the model.

Finally, the comparison of the FOWT and of the BF turbine under turbulence, highlights the fact that the FOWT exhibits a spanwise aerodynamic torque reduction and a spanwise airfoil aerodynamic inefficiency in terms of angle of attack, that can be solved via an aerodynamic redesign. As a result, a variety of blade twist angle and airfoil chord length profiles are developed, tested and evaluated using the FOWT annual energy production (AEP) as an indicator. The results point out that all solutions result in a slight FOWT AEP gain, compared to the original FOWT design, at the expense of increased rotor loading, which effectively increases the static floater pitch. Thus, the aerodynamic redesign approach requires a more cautious approach.

Table of Contents

Preface	iii
Summary	iv
List of Symbols	vii
List of Abbreviations	x
List of Figures	xvi
List of Tables	xvii
1 Introduction	1
1.1 Motivation	1
1.2 Project Scope	3
1.3 Report Structure	4
2 FOWT and Hydrogen Production Technology	5
2.1 Offshore Wind Hydrogen Production Configurations	5
2.2 Technical Characteristics of the FOWT In Situ Hydrogen Plant	8
2.3 Comparison of Floater Designs	9
2.4 FOWT Description	11
2.5 Dimensioning of the In Situ Hydrogen Production Plant	11
3 Research Methodology	14
3.1 Software Description	14
3.2 Simulation Setup	15
3.2.1 General Information	15
3.2.2 Convergence Analysis	18
3.3 Environmental Conditions	20
3.4 Controller Description	22
3.5 Incorporation of the In Situ Hydrogen Plant on OpenFAST Model	24
4 Simulation Results	28
4.1 Effect of Wind Shear	28
4.2 Effect of Static Floater Pitch Angle on the FOWT Power	29
4.2.1 Variable Static Floater Pitch Angle Simulations	30
4.2.2 Constant Static Floater Pitch Angle Simulations	33
4.3 Effect of the In Situ Hydrogen Production Plant on the FOWT Performance	35
4.4 Turbulent Wind Simulations	36
4.4.1 Effect of the Turbulence Intensity on the FOWT Performance	37
4.4.2 Comparison of the FOWT and BF Performance-Turbulent Conditions	40
5 Aerodynamic Redesign	47
5.1 Aerodynamic Redesign Methodology	47
5.2 Section Twist Angle Variation	49
5.3 Chord Length Variation	59
5.4 Section Twist Angle and Chord Length Variation	68

6 Conclusions and Recommendations	71
References	74
Appendix	79
A ElastoDyn Inputs for Blade Twist Angle Profiles	79
A.1 Elastodyn Inputs for Twist Angle Profile #1	79
A.2 Elastodyn Inputs for Twist Angle Profile #2	80
A.3 Elastodyn Inputs for Twist Angle Profile #3	81
A.4 Elastodyn Inputs for Twist Angle Profile #4	82
B Supportive Figures For Blade Twist	83
B.1 Power Curves of Twist Profiles 1-4	83
C ElastoDyn Inputs for Blade Chord Length Profiles	84
C.1 Elastodyn Inputs for Profile #1	84
C.2 Elastodyn Inputs for Profile #2	85
C.3 Elastodyn Inputs for Profile #3	86
C.4 Elastodyn Inputs for Profile #4	87
D Supportive Figures for Blade Twist and Chord Length Redesign	88
D.1 Relative Wind Speed Variation	88
D.2 Inflow Angle Variation	89
D.3 Axial Induction Factor Variation	89
D.4 Angle of Attack Variation	90
D.5 Aerodynamic Torque and Thrust Variation	91

List of Symbols

$\bar{\theta}_{fl,pitch}$	Average floater non-zero pitch angle
Δt	Turbulence simulation duration
η_{tot}	Total floating wind turbine efficiency (incl. electrical and mechanical efficiencies)
γ	Power law exponent
α	Angle of attack
a	Axial induction factor
a'	Tangential induction factor
dF_N	Out-of-plane (Thrust) force per unit length
dQ	In-plane (Torque) force per unit length
Ω	Rotor rotational speed
ρ	Air density
ρ_{water}	Sea water density
σ_x	x-direction turbulence
σ_y	y-direction turbulence
σ_z	z-direction turbulence
θ	Wind/wave misalignment angle
θ_{pitch}	Collective blade pitch angle
θ_{twist}	Local blade twist angle
φ	Inflow angle
B	Number of blades
$B_{pon,total}$	Total buoyancy force of the floater pontoons
B_{total}	Total buoyancy force of the floater
c	Airfoil local chord length
C_D	Airfoil drag coefficient
C_L	Airfoil lift coefficient
c_{max}	Maximum spanwise blade chord length

d	Floater draft
$d_{x,\max}$	Maximum acceptable Mann turbulence box x-direction step
d_x	Mann turbulence box x-direction step
d_y	Mann turbulence box y-direction step
d_z	Mann turbulence box z-direction step
dt_{sim}	OpenFAST simulation time step
$F_{\text{pretension}}$	Vertical pretension force due to mooring line weight
h	Height above mean sea level
H_{hub}	Reference height above mean sea level
H_s	Significant wave height
M_{FOWT}	All inclusive FOWT mass
$M_{\text{total,new}}$	Total mass of the augmented floater,excluding the wind turbine
M_i	Mass of each floater component
n_x	Mann turbulence box nodes in x-direction
n_y	Mann turbulence box nodes in y-direction
n_z	Mann turbulence box nodes in z-direction
P_{FOWT}	Floating wind turbine generator power
R	Rotor radius
r	Radial position of blade elements
$S_{\text{col,total}}$	Area of the platform cylindrical columns
t	Simulation time
T_p	Peak spectral period
U	Undisturbed wind speed
$U(h)$	Wind speed at height h
$U_{\text{box,max}}$	Maximum wind speed of each Mann turbulence box
$U_{\text{box,min}}$	Minimum wind speed of each Mann turbulence box
$U_{fl,pitch}$	Actual inflow wind speed due to an average floater non-zero pitch angle
U_{ref}	Wind speed at reference height
U_{rel}	Relative wind speed
V_{disp}	Volume of water displace by the FOWT
$z_{\text{CoG},i}$	Z-axis coordinate of the centre of gravity of each hydrogen component
z_{CoG}	Z-axis coordinate of the augmented floater center of gravity

C_p	Turbine power coefficient
g	Gravitational acceleration
H_i	Height of each hydrogen component
$I_{x,i}$	Mass moment of inertia of each hydrogen component in respect to the x axis of their reference frame
$I_{y,i}$	Mass moment of inertia of each hydrogen component in respect to the y axis of their reference frame
$I_{z,i}$	Mass moment of inertia of each hydrogen component in respect to the z axis of their reference frame
L_i	Length of each hydrogen component
$U_{\text{cut-in}}$	Turbine cut-in wind speed
$U_{\text{cut-out}}$	Turbine cut-out wind speed
U_{rated}	Turbine rated wind speed
W_i	Width of each hydrogen component

List of Abbreviations

AC	Alternating Current
AEP	Annual Energy Production
AoA	Angle of Attack
BEM	Blade Element Momentum
BF	Bottom-Fixed Wind Turbine
BNEF	Bloomberg New Energy Finance
CAPEX	Capital Expenditure
CF	Capacity Factor
CoB	Center of Buoyancy
CoG	Center of Gravity
DC	Direct Current
DLC	Design Load Case
DTU	Technical University of Denmark
FAST	Fatigue,Aerodynamics,Structure and Turbulence
FOWT	Floating Offshore Wind Turbine
HVAC	High Voltage Alternating Current
HVDC	High Voltage Direct Current
IEA	International Energy Agency
LCoE	Levelised Cost of Electricity
LCoH	Levelised Cost of Hydrogen
MSL	Mean Sea Level
NREL	National Renewable Energy Laboratory
OLAF	cOnvecting LAgrangian Filaments
OPEX	Operational Expenditure
PI	Proportional-Integral
RES	Renewable Energy Systems
RNA	Rotor-Nacelle Assembly
RO	Reverse Osmosis
RWT	Reference Wind Turbine
SS	Steady State
TI	Turbulence Intensity
TLP	Tension Leg Platform
TSR	Tip Speed Ratio

List of Figures

- 2.1 Centralised onshore hydrogen production layout. 6
- 2.2 Centralised offshore hydrogen production layout. 7
- 2.3 Decentralised offshore hydrogen production layout. 7
- 2.4 Types of floaters used for FOWT. Left: Spar buoy. Middle: Semi-submersible platform. Right: Tension-leg platform. Source:[42]. 9

- 3.1 Time-varying error compared to the steady state value of for all simulation variables considered in the convergence analysis, under steady wind conditions. . . . 19
- 3.2 Time-varying error compared to the steady state value of all simulation variables considered in the convergence analysis, under a TI value of 20%. 20
- 3.3 Time-varying error compared to the steady state value of all simulation variables considered in the convergence analysis, under a TI value of 10%. 20
- 3.4 Weibull probability density function with a scale parameter of 10.33 m/s and a shape parameter of 2.12. 22
- 3.5 C_p surface of the IEA 15 MW RWT for steady conditions. Black dashed curve: PI blade pitch control schedule for maximizing power at region 1.5. Red point: Optimal C_p and TSR values, tracked by the controller at region 2. Blue dashed curve: C_p and TSR variation under blade pitch actuation at region 3. Source: [78] 23
- 3.6 Dimensions of UMaine Voltturn US-S semi-submersible floater. The red parts of the floater are below the MSL, whereas the yellow ones are above. Source: [47]. . 25
- 3.7 Overlapping positioning of the hydrogen production components on the floater, considering the OpenFAST reference frame. 26

- 4.1 Power curves of the IEA 15 MW UMaine semi-sub FOWT for the three power law exponents examined. Blue curve: Uniform inflow, Red curve: Sheared inflow with $\gamma=0.11$. Yellow curve: Sheared inflow with $\gamma=0.3$ 29
- 4.2 Description of the 6 degrees of freedom of the IEA 15 MW FOWT on top of the UMaine semi-submersible floater in the coordinate system of OpenFAST. Source [47]. 30
- 4.3 Average floater pitch angles observed during the fully-coupled FOWT simulations for a uniform wind profile and for wind speeds ranging from 4 m/s to 24 m/s. 31
- 4.4 Comparison of the power curves of the IEA 15 MW RWT under BF configuration and under two scenarios:(i) fixed static floater pitch angle of 0° , (ii) variable static pitch angle according to wind speed. Blue curve: Scenario (i). Red curve: Scenario (ii). 31
- 4.5 Percent difference of the generated power and the of the rotor averaged wind speed in x-axis of the BF turbine under a non-zero variable static pitch, compared to the zero degree case. 32
- 4.6 Comparison of the power curves of the IEA 15 MW RWT under BF configuration for wind speeds 6 to 12 m/s under a constant floater pitch angle, ranging from 0° to 10° 33

4.7	Percent difference of the generated power and the of the rotor averaged wind speed of the BF turbine under a fixed static floater pitch angle for all wind speeds, compared to the zero° case. Blue curve: 2°. Orange curve: 4°. Yellow curve: 6°, Purple curve: 8°. Green curve: 10°.	34
4.8	Comparison of the power curves of the IEA 15 MW RWT under FOWT configuration for wind speeds 6 to 12 m/s under a constant static floater pitch angle, ranging from 0° to 10°.	34
4.9	Comparison of the power curves of the original of the augmented FOWT, which incorporates the in situ hydrogen production plant. Red solid curve: Original FOWT design. Blue dashed curve: Augmented FOWT design.	35
4.10	Comparison of the static floater pitch angle of the original FOWT and the augmented FOWT, which incorporates the in situ hydrogen production plant. Red solid curve: Original FOWT design. Blue dashed curve: Augmented FOWT design.	36
4.11	Comparison of the power curves of the IEA 15 MW FOWT on the UMaine semi-submersible floater for turbulence intensity values 5% to 20% with a step of 5% and for wind speeds 6-14 m/s. Black dashed curve: Steady wind. Green solid curve: TI=5%. Blue dashdotted curve: TI=10%. Yellow dotted curve: TI=15%. Red dashed curve: TI=20%.	38
4.12	Spanwise angle of attack variation of the IEA 15 MW FOWT for TI values 5% and 20% and for wind speeds 6 m/s and 9 m/s. Solid red error bars: AoA standard deviation. Dotted red errorbars: AoA 2x standard deviation. Black dashed line: Optimal AoA. Grey area: Stall region for the different airfoils.	39
4.13	Comparison of the time series of the rotor averaged wind speed and of the wind speed estimate of the ROSCO controller for an average wind speed of 11 m/s and for TI values 5% to 20%. Blue curves: Rotor averaged wind speed. Orange curves: Wind speed estimate.	40
4.14	Comparison of the average blade pitch and of the average floater pitch angles of the IEA 15 MW FOWT on the UMaine semi-submersible floater for turbulence intensity values 5% to 20% with a step of 5% and for wind speeds 6-14 m/s. Black dashed curve: Steady wind. Green solid curve: TI=5%. Blue dashdotted curve: TI=10%. Yellow dotted curve: TI=15%. Red dashed curve: TI=20%.	40
4.15	Comparison of the power curves and of the percent power reduction of the IEA 15 MW reference wind turbine under FOWT and BF configurations and under turbulent wind conditions with TI=10%. Red curve: FOWT. Blue curve: BF turbine.	41
4.16	Average tip speed ratio and rotational speed as a function of the wind speed for the IEA 15 MW reference wind turbine under FOWT and BF configurations and under turbulent wind conditions with TI=10%. Red curve: FOWT. Blue curve: BF turbine.	42
4.17	Average blade pitch and floater pitch angles as a function of the wind speed for the IEA 15 MW reference wind turbine under FOWT and BF configurations and under turbulent wind conditions with TI=10%. Red curve: FOWT. Blue curve: BF turbine.	42
4.18	Absolute and relative wind speed deficit of the IEA 15 MW reference wind turbine under FOWT and BF configurations under turbulent wind conditions with TI=10%. Red curve: FOWT. Blue curve: BF turbine.	43
4.19	Spanwise inflow angle variation of the the IEA 15 MW RWT under FOWT and BF configurations, under turbulent wind conditions with TI=10% and for an average wind speeds of 9 and 10.5 m/s. Red curve: FOWT. Blue curve: BF turbine.	45

4.20	Spanwise angle of attack variation of the the IEA 15 MW RWT under FOWT and BF configurations, under turbulent wind conditions with TI=10% and for an average wind speeds of 9 and 10.5 m/s. Red curve: FOWT. Blue curve: BF turbine. Dashed black line: Optimal angle of attack. Grey area: Stall region. . . .	46
4.21	Spanwise torque per unit length variation of the the IEA 15 MW RWT under FOWT and BF configurations, under turbulent wind conditions with TI=10% and for an average wind speeds of 9 and 10.5 m/s. Red curve: FOWT. Blue curve: BF turbine.	46
5.1	Typical velocity triangle for a random radial position along the blade span. . . .	48
5.2	Comparison of the spanwise blade twist profiles for the aerodynamic redesign of the IEA 15 MW FOWT. Solid blue curve: Original blade twist angle variation. Solid orange curve: Inboard twist angle equal to original profile, midboard blade twist decrease of 1°, followed by an outboard 0.3° decrease. Dotted yellow curve: Inboard and midboard twist angle decrease of 1° followed by a 0.3° decrease towards the tip. Dashed purple curve: Inboard twist angle equal to original twist angle variation, midboard twist angle decrease of 1°, followed by a 0.5° twist angle decrease towards the tip. Dashed green curve: Midboard twist angle reduction by 1°, inboard and outboard twist angle equal to original values. . . .	51
5.3	Power generation of the IEA 15 MW FOWT according to the original and the redesigned blade twist angle profiles for the average wind speeds of 9 and 10.5 m/s respectively. Blue curve: Original blade twist angle profile. Orange curve: Blade twist profile 1. Orange curve: Blade twist profile 2. Purple curve: Blade twist profile 3. Green curve: Blade twist profile 4.	53
5.4	Variation of the static floater pitch angle of the IEA 15 MW FOWT according to the original and the redesigned blade twist angle profiles for average wind speeds between 9 and 12 m/s. Blue curve: Original blade twist angle profile. Orange curve: Blade twist profile 1. Orange curve: Blade twist profile 2. Purple curve: Blade twist profile 3. Green curve: Blade twist profile 4.	54
5.5	Variation of the relative wind speed at the radial position of 0.715 of the IEA 15 MW FOWT according to the original and the redesigned blade twist angle profiles for average wind speeds of 9 and 10.5 m/s. Blue curve: Original blade twist angle profile. Orange curve: Blade twist profile 1. Orange curve: Blade twist profile 2. Purple curve: Blade twist profile 3. Green curve: Blade twist profile 4.	54
5.6	Spanwise inflow angle variation of the IEA 15 MW FOWT according to the original and the redesigned blade twist angle profiles for average wind speeds of 9 and 10.5 m/s. Blue curve: Original blade twist angle profile. Orange curve: Blade twist profile 1. Orange curve: Blade twist profile 2. Purple curve: Blade twist profile 3. Green curve: Blade twist profile 4.	55
5.7	Spanwise variation of the axial induction factor of the IEA 15 MW FOWT according to the original and the redesigned blade twist angle profiles for average wind speeds of 9 and 10.5 m/s. Blue curve: Original blade twist angle profile. Orange curve: Blade twist profile 1. Orange curve: Blade twist profile 2. Purple curve: Blade twist profile 3. Green curve: Blade twist profile 4.	56
5.8	Rotor averaged wind speeds of the IEA 15 MW FOWT according to the original and the redesigned blade twist angle profiles for average wind speeds of 9 and 10.5 m/s. Blue curve: Original blade twist angle profile. Orange curve: Blade twist profile 1. Orange curve: Blade twist profile 2. Purple curve: Blade twist profile 3. Green curve: Blade twist profile 4.	57

5.9	Spanwise angle of attack variation of the IEA 15 MW FOWT blades according to the original and the redesigned blade twist angle profiles for the average wind speeds of 9 and 10.5 m/s respectively. Blue curve: Original blade twist angle profile. Orange curve: Blade twist profile 1. Orange curve: Blade twist profile 2. Purple curve: Blade twist profile 3. Green curve: Blade twist profile 4.	58
5.10	Spanwise torque and thrust variation of the IEA 15 MW FOWT blades according to the original and the redesigned blade twist angle profiles for the average wind speed of 9 m/s. Blue curve: Original blade twist angle profile. Orange curve: Blade twist profile 1. Orange curve: Blade twist profile 2. Purple curve: Blade twist profile 3. Green curve: Blade twist profile 4.	59
5.11	Spanwise torque and thrust variation of the IEA 15 MW FOWT blades according to the original and the redesigned blade twist angle profiles for the average wind speed of 10.5 m/s. Blue curve: Original blade twist angle profile. Orange curve: Blade twist profile 1. Orange curve: Blade twist profile 2. Purple curve: Blade twist profile 3. Green curve: Blade twist profile 4.	59
5.12	Comparison of the spanwise chord length profiles for the aerodynamic redesign of the IEA 15 MW FOWT. Solid blue line: Original chord length variation. Dashed orange line: 6% chord length increase in the inboard blade part. Dashdotted yellow : 6% chord length increase in the whole blade. Solid purple and solid green curves: 9% and 12% spanwise chord length increase respectively.	61
5.13	Power curves and static floater pitch angles of the original and the redesigned FOWT, according to the chord length increase profiles studied in this project and for wind speeds between 9 and 12 m/s. Blue curves: Original chord length profile. Orange curves: Chord length profile 1. Yellow curves: Chord length profile 2. Purple and Green curves: Chord length profiles 3 and 4 respectively. .	62
5.14	Variation of the relative wind speed of the original and the redesigned FOWT at the radial position of 0.715, according to the chord length increase profiles studied in this project for an average wind speeds of 9 m/s and 10.5 m/s. Blue curves: Original chord length profile. Orange curves: Chord length profile 1. Yellow curves: Chord length profile 2. Purple and Green curves: Chord length profiles 3 and 4 respectively.	64
5.15	Variation of the spanwise inflow angles of the original and the redesigned FOWT, according to the chord length increase profiles studied in this project for an average wind speeds of 9 m/s and 10.5 m/s. Blue curves: Original chord length profile. Orange curves: Chord length profile 1. Yellow curves: Chord length profile 2. Purple and Green curves: Chord length profiles 3 and 4 respectively. .	64
5.16	Variation of the spanwise axial induction factors of the original and the redesigned FOWT, according to the chord length increase profiles studied in this project for an average wind speeds of 9 m/s and 10.5 m/s. Blue curves: Original chord length profile. Orange curves: Chord length profile 1. Yellow curves: Chord length profile 2. Purple and Green curves: Chord length profiles 3 and 4 respectively.	65
5.17	Variation of the rotational speed and blade pitch angle of the original and the redesigned FOWT, according to the chord length increase profiles studied in this project for average wind speeds between 9 and 12 m/s. Blue curves: Original chord length profile. Orange curves: Chord length profile 1. Yellow curves: Chord length profile 2. Purple and Green curves: Chord length profiles 3 and 4 respectively.	65

5.18	Spanwise angle of attack variation of the original and the redesigned FOWT, according to the chord length increase profiles studied in this project and for an average wind speeds of 9 and 10.5 m/s. Blue curves: Original chord length profile. Orange curves: Chord length profile 1. Yellow curves: Chord length profile 2. Purple and Green curves: Chord length profiles 3 and 4 respectively. Black dashed line: Spanwise optimal AoA.	66
5.19	Spanwise variation of the per unit length torque and thrust of the original and the redesigned FOWT, according to the chord length increase profiles studied in this project and for an average wind speed of 9 m/s. Blue curves: Original chord length profile. Orange curves: Chord length profile 1. Yellow curves: Chord length profile 2. Purple and Green curves: Chord length profiles 3 and 4 respectively.	67
5.20	Spanwise variation of the per unit length torque and thrust of the original and the redesigned FOWT, according to the chord length increase profiles studied in this project and for an average wind speed of 10.5 m/s. Blue curves: Original chord length profile. Orange curves: Chord length profile 1. Yellow curves: Chord length profile 2. Purple and Green curves: Chord length profiles 3 and 4 respectively.	68
5.21	Power curves of the original and the redesigned FOWT, according to blade twist profile 2, chord length profile 2 and the combination of the two profiles, for wind speeds between 9 and 12 m/s . Blue curve: Power curve according to the original chord length profile, Orange curve: Power curve according to blade twist profile 2. Yellow curve: Power curve according to chord length profile 2. Purple line: Power curve according to the combination of the two profiles respectively.	70
5.22	Static floater pitch angle variation of the original and the redesigned FOWT, according to blade twist profile 2, chord length profile 2 and the combination of the two profiles, for wind speeds between 9 and 12 m/s . Blue curve: Static floater pitch according to the original chord length profile, Orange curve: Static floater pitch according to blade twist profile 2. Yellow curve: Static floater pitch according to chord length profile 2. Purple line: Static floater pitch according to the combination of the two profiles respectively.	70
B.1	Power Curves of the IEA 15 MW FOWT according to the original and redesigned blade twist angle profiles for average wind speeds between 9 and 12 m/s. Blue curve: Original blade twist angle profile. Orange curve: Blade twist profile 1. Orange curve: Blade twist profile 2. Purple curve: Blade twist profile 3. Green curve: Blade twist profile 4.	83
D.1	Relative wind speed variation of the original and the redesigned FOWT at the radial position of 0.715, according to blade twist profile 2, chord length profile 2 and the combination of the two profiles, for wind speeds 9 m/s and 10.5 m/s. Blue curves: Original profiles, Orange curves: Blade twist profile 2. Yellow curves: Chord length profile 2. Purple curves: Combination of the two profiles.	88
D.2	Spanwise inflow angle variation of the original and the redesigned FOWT, according to blade twist profile 2, chord length profile 2 and the combination of the two profiles, for wind speeds 9 m/s and 10.5 m/s. Blue curves: Original profiles, Orange curves: Blade twist profile 2. Yellow curves: Chord length profile 2. Purple curves: Combination of the two profiles.	89

D.3	Spanwise axial induction factor variation of the original and the redesigned FOWT, according to blade twist profile 2, chord length profile 2 and the combination of the two profiles, for wind speeds 9 m/s and 10.5 m/s. Blue curves: Original profiles, Orange curves: Blade twist profile 2. Yellow curves: Chord length profile 2. Purple curves: Combination of the two profiles.	89
D.4	Spanwise angle of attack variation of the original and the redesigned FOWT, according to blade twist profile 2, chord length profile 2 and the combination of the two profiles, for wind speeds 9 m/s and 10.5 m/s. Blue curves: Original profiles, Orange curves: Blade twist profile 2. Yellow curves: Chord length profile 2. Purple curves: Combination of the two profiles. Dashed black line: Spanwise optimal AoA.	90
D.5	Spanwise torque and thrust per unit length variation of the original and the redesigned FOWT, according to blade twist profile 2, chord length profile 2 and the combination of the two profiles, for a wind speed of 9 m/s. Blue curves: Original profiles, Orange curves: Blade twist profile 2. Yellow curves: Chord length profile 2. Purple curves: Combination of the two profiles.	91
D.6	Spanwise torque and thrust per unit length variation of the original and the redesigned FOWT, according to blade twist profile 2, chord length profile 2 and the combination of the two profiles, for a wind speed of 10.5 m/s. Blue curves: Original profiles, Orange curves: Blade twist profile 2. Yellow curves: Chord length profile 2. Purple curves: Combination of the two profiles.	91

List of Tables

- 2.1 Physical dimensions, weight and power consumption of components constituting the in situ hydrogen production plant,added on the FOWT considered in this project. 13
- 3.1 Mann Turbulence box parameters for the three wind speed classes examined. . . 17
- 3.2 Most expected combinations of wind speed U , significant wave height H_s , peak spectral period T_p and wind/wave misalignment θ of the general US East Coast site considered in this project. Source: [72]. 21
- 3.3 Comparison of design parameters, relevant for the modelling of FOWT in OpenFAST, for the original and the augmented floater, with differences owing to the consideration of the in situ hydrogen production plant. 27
- 5.1 Description and reasoning of the four twist angle profiles used for the aerodynamic redesign of the IEA 15 MW RWT FOWT considered in this project. 52
- 5.2 Comparison of the AEP, the AEP increase compared to the original FOWT and the AEP deficit compared to the BF wind turbine for the original FOWT and the redesigned FOWT, according to the four blade twist profile variations. 52
- 5.3 Description and reasoning of the four chord length profiles used for the aerodynamic redesign of the IEA 15 MW RWT FOWT considered in this project. 61
- 5.4 Comparison of the AEP, the AEP increase compared to the original FOWT and the AEP deficit compared to the BF wind turbine for the original FOWT and the redesigned FOWT, according to the four chord length profile variations. 62
- 5.5 Comparison of the AEP, the AEP increase compared to the original FOWT and the AEP deficit compared to the BF wind turbine for the original FOWT and the redesigned FOWT, according to the blade twist profile 2,chord length profile 2 and the combination of the two profiles. 69
- A.1 ElastoDyn OpenFAST input data for twist angle profile #1. 79
- A.2 ElastoDyn OpenFAST input data for twist angle profile #2. 80
- A.3 ElastoDyn OpenFAST input data for twist angle profile #3. 81
- A.4 ElastoDyn OpenFAST input data for twist angle profile #4. 82
- C.1 ElastoDyn OpenFAST input data for chord length profile #1. 84
- C.2 ElastoDyn OpenFAST input data for chord length profile #2. 85
- C.3 ElastoDyn OpenFAST input data for chord length profile #3. 86
- C.4 ElastoDyn OpenFAST input data for chord length profile #4. 87

1 | Introduction

1.1 Motivation

The world's transition towards a sustainable future mandates that the global increase in temperature should be limited at 2°C, with the view to reducing it to 1.5°C [1]. However, to achieve this target, all countries-members of the Paris Agreement, should pursue the decarbonisation of all energy sectors, with the help of renewable energy systems (RES) [2]. According to the most aggressive energy transition scenario proposed by IRENA, by 2050, more than 50% of the total final energy consumption will be represented by renewable electricity [3]. However, due to the REPowerEU strategy, initiated in March 2022, countries of the EU-27 will further accelerate the electrification of all sectors, including industry [4]. The goal of this effort is to ensure the EU countries' energy safety and to tackle the volatility of energy prices [4].

Nevertheless, the increased share of green electricity requires its conversion to other forms, so as to enhance the flexibility of energy systems. In addition, electricity from RES should be used in the transportation and in the heating sectors. A promising means to achieve both requirements is hydrogen [5]. Hydrogen can be used locally, near the production site or can be distributed at large distances via pipelines or tanker vessels, thus increasing the energy systems flexibility [2]. In addition, as described by the International Energy Agency (IEA), hydrogen will have a crucial role in guaranteeing zero net emissions by 2050 [6]. This will result in an approximately twofold increase in hydrogen demand as early as 2030. Yet, due to the REPowerEU strategy, the hydrogen demand is expected to boom even more, due to substitution of natural gas via hydrogen [4]. In addition, the proposed rapid development of hydrogen infrastructure such as production plants, storage facilities and distribution hubs is likely to be an additional incentive for a larger hydrogen demand [4].

It should be noted that the environmental footprint of hydrogen is associated with its production technique. As a result, the most carbon-neutral form of hydrogen is green hydrogen, which is produced from RES via electrolysis [2]. The green hydrogen demand is predicted to boom as early as 2030, with the view of having a near 50 % share in the total hydrogen demand by 2050 [7]. Still, more-carbon intensive forms of hydrogen, such as blue hydrogen or grey hydrogen, which are both produced from natural gas, are generally estimated to have a lower levelised cost of hydrogen (LCoH) than that of green hydrogen [2, 8]. This is caused by the electricity costs for green hydrogen production, which are higher than those of natural gas in the case of blue or grey hydrogen.

In case that the price of the renewable electricity for green hydrogen production falls under 17 €/MWh, green hydrogen will be cost competitive with other forms of hydrogen [6]. Still, according to a study of Bloomberg New Energy Finance (BNEF), as of March 2022, the natural gas price spikes, not only did not affect the green hydrogen prices, but also green hydrogen is currently cheaper than both blue and grey hydrogen [9, 10]. It is evident that green hydrogen is likely to be the dominant hydrogen type in the years to come, not only due to the fact that it is more environmentally friendly, but also it is not subjected to the volatility of fossil fuel prices.

Since a boom of green hydrogen demand will occur in the years to come, the renewable electricity capacity should be able to supply the required electrolysis energy inputs. At the same time, green hydrogen production costs, described by the levelised cost of electricity (LCoE) input, should be at the same level or even lower than conventional forms of energy [11]. In this direction, the offshore wind potential can be a major contributor in supplying the energy needs since it is fairly unexploited [12]. In addition, approximately 80% of the worldwide wind potential is situated in deep waters (depth > 60 m) [12], where conventional monopile offshore wind turbines cannot be installed in an economically viable way [13]. Hence, it is evident that the wind resource in waters with depth ranging from 60 m to 200 m, can be exploited solely by floating offshore wind turbines (FOWT). FOWT will rapidly grow this decade, as approximately 36 GW of FOWT power are estimated to be commissioned worldwide by 2030 [14]. By 2050, the FOWT installed power is predicted to increase approximately 30 times, compared to 2030 [15].

In addition, the REPowerEU strategy will try to further boost the introduction of new RES in order to reduce natural gas dependence [4]. Although, the LCoE of FOWT is estimated to be higher than the that of the bottom-fixed (BF) wind turbines, the FOWT ability of gaining access to the unexploited wind potential at deep waters, makes them essential for supplying the renewable energy demand for green hydrogen. This is also justified by examining the capacity factors (CF) of FOWT and BF offshore wind farms; In 2020, the average capacity factor of Hywind Tampen FOWT wind farm was 57%, while the average CF for BF offshore farms is 40% [16]. Therefore, from the aforementioned analysis, it can be deduced that FOWT, starting from this decade, are to be major players in the RES field, because they will be used to further exploit the wind potential and to generate a high amount of renewable electricity. This observation underlines that they should be closely examined and studied by the scientific community.

FOWT consist of a wind turbine, which is commonly designed for BF offshore applications, placed on a floater. As far as hydrogen production is concerned, the FOWT will supply their generated electricity to a hydrogen production plant. In this direction, three topologies are studied in literature [7, 11]: (i) centralised offshore hydrogen production, where clusters of FOWT supply electricity to a large scale green hydrogen production plant, situated at a large offshore platform, (ii) onshore hydrogen production, which is the same as (i) but the electrolyser is situated onshore and (iii) decentralised (in situ) hydrogen production by a cluster of electrolysers, situated on the floaters and/or inside the turbines. From those solutions, in situ hydrogen production is estimated to be the most cost-effective, since the pipelines needed for distributing green hydrogen onshore are cheaper than high voltage AC (HVAC) or high voltage DC (HVDC) cabling [17]. Also, pipelines result in less energy losses than HVAC or HVDC lines [11]. As a result, in this thesis project, the green hydrogen production plant will be integrated on the FOWT, thereby leading to in situ hydrogen production layout.

The literature review showed that FOWT are thoroughly studied by the scientific and academic community. Robertson et al. (2014) developed a semi-submersible floater to accommodate the National Renewable Energy Laboratory (NREL) 5 MW reference wind turbine [18]. Zhao et al. (2021), modeled a state-of-the-art semi submersible floater to be used with the Technical University of Denmark (DTU) 10 MW wind turbine [19]. Mazarakos et al. (2021) investigated the effect of combined wind and wave loading on a tension-leg platform, developed for the DTU 10 MW wind turbine [20]. Mahfouz et al. (2020) developed and simulated two floater designs for the IEA 15 MW reference wind turbine [21].

Nevertheless, in the aforementioned works, the coupling of the wind turbine with the floater did not consider the effect of the floater motion in the design and the operation of the wind turbine. Instead, ultimate and fatigue limit state analyses were conducted for the loads sustained by the floater and the turbine, under wind and wave conditions described by IEC 61400-3 standard

[22]. Furthermore, when in situ hydrogen production is considered, works like those of Ibrahim et al. (2022) [11] and Calado and Castro (2021) [23] provided recommendations on the layout and the components constituting the plant but they did not consider the effect of the added weight of the hydrogen production plant on the FOWT performance.

Thus, this thesis project will try to bridge the aforementioned literature gaps by setting a twofold goal. Firstly, the impacts of the floater motion, of the adaptation of a turbine, originally designed for BF application, as a FOWT and of the added mass of the in situ hydrogen production on the turbine performance will be evaluated and quantified. Secondly, in case a FOWT performance deterioration is observed under the three aforementioned cases, an aerodynamic redesign of the FOWT will be undertaken. The ultimate goal of this effort will be to bring the FOWT performance near to its BF counterpart, thus tackling energy losses and boosting its annual energy production. Consequently, the produced electricity LCoE and potentially the green hydrogen LCoH may be decreased owing to the FOWT performance gains.

1.2 Project Scope

Considering the aforementioned problem analysis, the main research question of this project can be formulated as:

Should floating offshore wind turbines for in situ hydrogen production be aerodynamically redesigned?

To answer the research question, several sub-questions need to be answered as well:

1. What is the combination of wind turbine, floater type and installation site, which are going to be considered as the baseline scenario for this project?
2. What is the impact of the floater design on the performance of the FOWT?
3. In which way does the hydrogen production plant impact the performance of the FOWT?
4. How does the performance of the wind turbine change when it is adapted from the original BF offshore application to the floating one?
5. What are the benefits of a possible aerodynamic redesign of the wind turbine?

As already described, this project will try to shed light on the way a wind turbine, which was originally designed for BF application, is affected by its placement on a moving floater. At a second step, the effect of the added mass of the in situ hydrogen plant on the FOWT performance will be evaluated. Therefore, the core of this project will be the wind turbine itself, in order to decide if an aerodynamic redesign of the wind turbine should be undertaken to reduce potential performance penalties. More specifically, the simulations that will be conducted during this project will focus on whether the power production characteristics of the turbine change in case of a conversion from a BF to a FOWT. Attention will be also given on the blade loading, which is likely to change due to the dynamic floater displacement and different turbine controller dynamics. It should be noted that, although a structural redesign of the turbine and of the floater are also solutions for boosting the energy production of the FOWT, they will not be examined in this thesis project.

As far as hydrogen production is concerned, since this project will focus mainly on the aerodynamic performance of the rotor, it will be simplified to a great extent via reasonable assumptions. More specifically, the in situ hydrogen plant will be dimensioned according to the wind turbine's rated power and not with the view of meeting a specified hydrogen load. In addition, following the rationale of Ibrahim et al. (2022) [11], the combined operation of the wind tur-

bine and of the hydrogen production plant will not be examined. Instead, as proposed in the aforementioned work, hydrogen production will be considered as a black box, determined by the individual components efficiencies and rated outputs.

1.3 Report Structure

This report is structured as follows. Chapter 2 describes the in situ hydrogen plant and the FOWT, with the view of justifying choices made for this project about the selected FOWT design and the hydrogen plant topology and its physical dimensions. Then, Chapter 3 delves into the methodology and the theoretical background used for the problem approach, i.e the software and its inputs, the environmental conditions and the logic behind the incorporation of the in situ hydrogen plant in the FOWT model. Chapter 4 provides the simulation results for all the topics studied in this project, which are mainly aligned with sub-questions 2,3 and 4. Moreover, Chapter 5 provides an answer to the main research question of this project by highlighting the benefits and culprits of possible aerodynamic redesign solutions, while Chapter 6 concludes this report and provides recommendations for further research. Non-essential results, which may be useful for the reader, are presented into the Appendix of this report.

2 | FOWT and Hydrogen Production Technology

The goal of this chapter is to justify the choices and assumptions made about the FOWT and the hydrogen production layout respectively, therefore answering sub-question 1. More specifically, Section 2.1 explains why in situ hydrogen production via FOWT is considered in this project, while Section 2.2 tries to shed light on the components, which comprise the aforementioned hydrogen production layout. Furthermore, in Section 2.3, a comparison of the existing floater designs for FOWT is presented, with the view of highlighting which is the more suitable for accommodating the hydrogen plant of this project. Then, Section 2.4 focuses on the combination of the wind turbine and the floater, constituting the FOWT modeled in this project, culminating in Section 2.5, where a dimensioning of the in situ hydrogen plant components is conducted.

2.1 Offshore Wind Hydrogen Production Configurations

According to literature, the LCoH of hydrogen production from offshore wind turbines is influenced by the configuration of the energy conversion system [7, 23]. Therefore, it is useful to investigate which configuration leads to lower costs and therefore lower LCoH. In this regard, the following system architectures are proposed for producing hydrogen from FOWT [7, 23]: (i) centralised onshore hydrogen production, (ii) centralised offshore hydrogen production and (iii) decentralised (in situ) offshore hydrogen production, on the floater of the wind turbines. Each configuration will be thoroughly examined to highlight its characteristics, advantages and disadvantages, with the scope of determining which is the most economically effective solution to be implemented in this project.

First, in the centralized onshore hydrogen production configuration, hydrogen is produced by a main plant, which is situated onshore. A schematic of this system is shown in Figure 2.1. More specifically, the final product of the floating offshore wind turbines is HVAC power, which is supplied to shore after being stepped up to minimize power losses. Once onshore, it is converted to DC power to supply the electrolyser and to lower voltage AC power for powering the necessary ancillary devices of the plant. Then, the hydrogen produced by the plant, enters the distribution network (pipelines or trucks) or it is stored in hydrogen-compatible tanks. An advantage of this layout is its simplicity and its viability because the whole hydrogen plant is placed under enclosed premises, so that adverse weather conditions are not an issue [7]. In addition, the maintenance of the hydrogen production plant can be easy and less costly than in other configurations because they are not dependent on weather windows [23].

However, the transfer of HVAC power via cables over long distances incurs losses due to reactive power, which are up to 5% for a distance 50-100 km from shore [24, 25]. It is evident that losses increase even more when the FOWT are installed at distances higher than 100 km from shore. One possible solution to this issue would be the power transfer via high voltage direct current (HVDC) lines because, although having higher costs than the HVAC ones, they can lead to lower losses [23]. It should be noted that the two power transfer configurations are in parity in

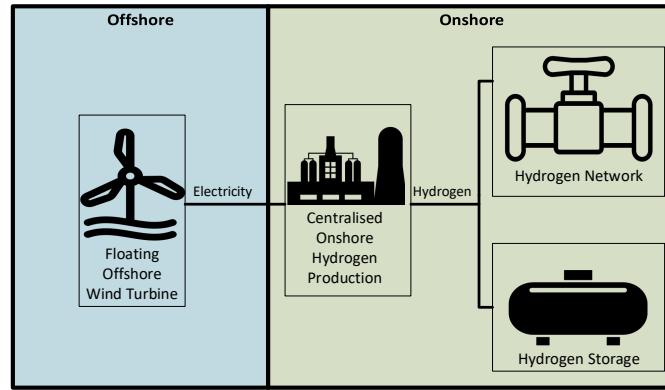


Figure 2.1: Centralised onshore hydrogen production layout.

terms of costs and losses when high power applications are concerned, which involve power transfer distances higher than 100 km from shore [26]. Nevertheless, even the HVDC power transfer leads to significant power losses, which are in the range of 2%-4%, depending on the power level and cable length [24, 25].

Thus, it is evident that the centralized onshore hydrogen production configuration using FOWT is not economically attractive due to its high costs and losses [7]. It should be noted that, since electrolysis requires water as an input, the onshore layout will create conflicts on water use and it is not suitable for areas suffering from droughts and inadequate water supply [27].

As far as the offshore layouts are concerned, for both centralised and decentralised offshore hydrogen production, hydrogen is transferred onshore via pipelines instead of HVAC or HVDC lines. Pipelines are not only cheaper than HVAC and HVDC cabling, but also they are associated with lower energy losses than electrical lines. Hence, hydrogen pipelines are able to reduce the projects' capital expenditure (CAPEX), while making them more energy efficient, thus maximizing the economic benefit from the hydrogen plant. More specifically, the all-inclusive cost for constructing and installing a pipeline is estimated at approximately 1.2 M€/km while the total cost for a HVAC or HVDC cabling is in excess of 3.5 M€/km [17]. In addition, existing natural gas pipelines can be converted for pure hydrogen transport because it can be easily and cheaply modified for use with hydrogen [28]. However, in both new and existing pipelines, losses are at maximum 0.1%, which are significantly lower than those of the HVAC and HVDC power transfer [29].

Furthermore, the literature review showed that both offshore layouts employ the same components to produce electricity from FOWT [7, 17]. However, the components' size varies substantially for the two layouts in question, since, in the decentralised solution, the hydrogen production system comprises of a multitude of small-scale subsystems, installed on the FOWT floaters. It is evident that, since the hydrogen plant will be fed with desalinated seawater, the offshore layouts are not bound to water use considerations and they do not create conflicts between different water uses [30].

In the centralised offshore hydrogen production system, the FOWT supply electricity to a main hydrogen production facility, which is situated on a large offshore platform. Hydrogen is produced at a large scale and, after being compressed, it is transferred via pipelines to the onshore hydrogen distribution network, or it is stored in tanks. A schematic of this layout is presented in Figure 2.2. On the other hand, the decentralised offshore hydrogen production layout, which is depicted in Figure 2.3, consists of small-scale hydrogen production facilities, located on the floater of the FOWT. Then, hydrogen from each platform flows to small risers,

which are connected to a large manifold and is transported to shore via pipelines in the same way as in the centralised layout [7]. However, it should be noted that the decentralised offshore solution is economically viable for wind turbines with a rated power over 10 MW because larger electrolysers can be installed, thus incurring cost reductions due to economies of scale [31].

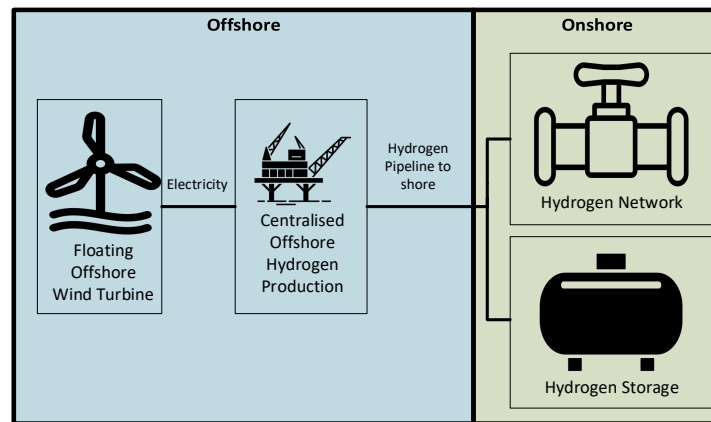


Figure 2.2: Centralised offshore hydrogen production layout.

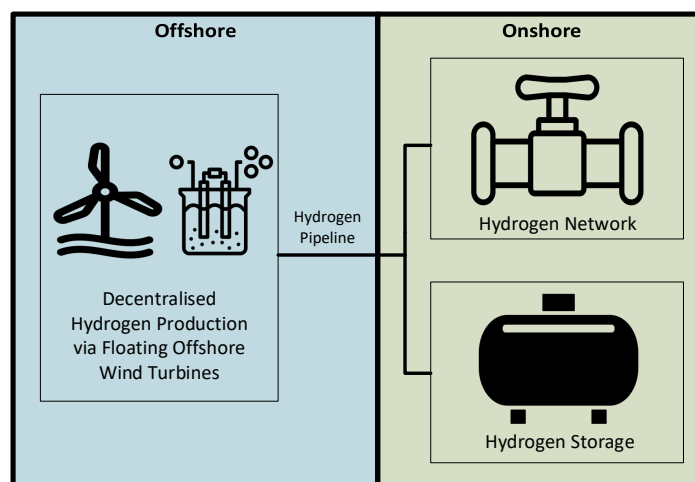


Figure 2.3: Decentralised offshore hydrogen production layout.

A disadvantage of the centralised offshore hydrogen production system is its low reliability in the face of adverse weather conditions, component failures and hazardous incidents like hydrogen leaks and fires. This stems from the fact that all the equipment and the manpower are concentrated in one place [7]. As a result, mishaps have a high probability to lead not only to infrastructure damage but also to hinder the safety of the workers on the platform. In addition, the hydrogen plant may be rendered offline for prolonged time after a failure, owing to the unfavourable weather conditions and long distances from shore, which may slow down the repair works. It is worth mentioning that, although large scale platforms have been developed for the oil and gas industries, they have high CAPEX and operational expenditures (OPEX), thus they are economically unattractive for centralised offshore hydrogen production. [7]. Hence, the high reliability and the lower cost of the decentralised layout, in respect to the centralised one, makes it more promising for producing hydrogen from FOWT.

Therefore, this project will focus on the decentralised (in situ) offshore layout for hydrogen production via FOWT. Nevertheless, it should be noted that the physical dimensions of the hydrogen production plant impose constraints on the floater type which is suitable to be used

in such a layout [23]. This will be closely examined in Section 4.2 of this project. Also, even if the hydrogen components fit on the floating platform, additional modifications should take place to pair the floater with the hydrogen plant and to shield all sensitive equipment from water damage [23].

An additional justification for the choice of the decentralised offshore hydrogen production via FOWT as the basis of this project is the comparison of LCoH prediction of the examined layouts. According to the LCoH estimates produced for the Dolphyn project, which examines the possibility of in situ hydrogen production via FOWT, the decentralised offshore hydrogen production on spar buoys or semi-submersible platforms is likely to have the lowest LCoH [7]. The exact opposite is observed for the centralised onshore hydrogen layout. This is a result of the higher costs and losses of HVAC and HVDC lines, which increase even more as the distance from shore increases. In the case of offshore hydrogen production, the LCoH of the centralised offshore layout is higher than that of the decentralised one, due to the offshore platform costs and the mandatory manning of the platform, which incurs logistical costs [7].

However, for both offshore layouts, the LCoH increase due to larger offshore distances, is minimal because of the low pipeline losses. Finally, the LCoH of the semi-submersible FOWT is lower than that of the spar buoy. This is a result of the low modifications required to accommodate the hydrogen plant to the semi-submersible floater. In conclusion, from a techno-economical perspective, the in situ hydrogen production via FOWT is more promising than other alternatives. Thus, it will be closely examined in this project. However, the LCoH figures suggest that attention should be given to the choice of the specific floater type as different floaters have a different effect on the system LCoH.

2.2 Technical Characteristics of the FOWT In Situ Hydrogen Plant

The next step after determining that the in situ hydrogen production on top of the floater of FOWT has the potential of being a cost effective solution for hydrogen production via offshore wind, is to examine which components comprise the decentralised offshore hydrogen plant. The literature review showed that, in addition to the electrolyser, a desalination plant, a full scale (AC to DC and AC to AC) power converter, a sea water pump, a hydrogen compressor, an auxiliary power source and a riser for hydrogen distribution constitute a typical in situ hydrogen production plant [7, 11].

More specifically, as far as the electrolyser is concerned, a PEM electrolyser will be considered in this project because it offers operational flexibility, making it suitable to be coupled with intermittent wind turbines [32]. Since a PEM electrolyser operates with DC current, while the output of the wind turbine is AC current, an AC to DC converter is required for their coupling. Moreover, the PEM electrolyser needs to be supplied with desalinated water [33], so a desalination unit should be considered for the treatment of the sea water [34]. The most common water desalination technology for supplying PEM electrolysers is Reverse Osmosis (RO), because it is the least energy-intensive desalination method [30, 35]. Although the product of RO requires additional purification steps, RO is more suitable for floating offshore applications because sea water can be pumped from large depths, thus not having impurities or excessive turbulence [36]. In addition, as already mentioned, seawater should be pumped from the sea to the RO plant level. As a result, seawater-compatible pumps should be installed on the floater.

After its production, hydrogen should be transported from the decentralised production site to other sites. Those may be centralised pipeline networks or refuelling hubs for tankers [7]. In both cases, it needs to be compressed to improve the transport capacity of the distribution

network and to counter the associated pressure drop [37]. Therefore, a hydrogen compressor should be present at the hydrogen production site. According to Carter et al. (2020) [38], the hydrogen produced by a PEM electrolyser has a pressure of 30-70 bar [2], while, in order to minimise losses, hydrogen should be compressed to pressures ranging from 80 to 100 bar [37]. Thus, it is assumed that hydrogen is compressed to 100 bar at the production site before being transported elsewhere. Finally, the produced hydrogen flows towards the distribution network via flexible catenary risers, made from alternating layers of steel and high density polyethylene (HDPE) [39, 40].

2.3 Comparison of Floater Designs

However, the in situ hydrogen production layout via FOWT has an impact on the floater design, which will be considered in this project [11]. This stems from the fact that the floaters' dynamic behavior and their available space for the hydrogen plant components are the main drivers for determining their suitability for decentralised offshore hydrogen production [41]. The main floater designs used in commercially available solutions and simulation models are [41]: (i) spar buoy, (ii) tension-leg platform (TLP) and (iii) semi-submersible platform. A schematic representation of the three floater types is given in Figure 2.4.



Figure 2.4: Types of floaters used for FOWT. Left: Spar buoy. Middle: Semi-submersible platform. Right: Tension-leg platform. Source:[42].

A **spar buoy** consists of a cylinder, which is the physical extension of the wind turbine conventional tower, but with a slightly larger diameter [7, 41]. It is normal to the sea plane and it uses a ballast for ensuring that its centre of buoyancy is higher than its centre of gravity, thus ensuring structural stability. However, in order for this to happen, the in-water part of the spar buoy has a high length, therefore making this floater suitable for deep waters (100-200 m) [41]. The floater is moored via mooring lines, which employ a variety of anchoring systems.

The spar buoy is characterised by design simplicity, making it suitable for mass production [41]. Also, mooring is a straightforward task, while owing to its construction and its ballast configuration, it is less sensitive to wave loading [43]. Nevertheless, the deep draft of the spar buoy results in its incompatibility with relatively shallow waters [41]. In addition, commissioning of the spar buoy is more complicated and costly, in comparison to other floaters [41, 43]. This stems from the fact that, due to the large floater draft, it has to be transported on site at a horizontal orientation, while special equipment is required for its vertical reposition [41].

In addition, one main disadvantage of the spar buoy when in situ hydrogen production from FOWT is concerned, is the inadequate area to install the hydrogen plant components [7]. The spar buoy does not offer a dedicated flat plane for placing the equipment, as in the semi-submersible and TLP floaters. Hence, the spar buoy should be considerably modified in the case of the decentralised offshore hydrogen production. This can be done by installing a cantilevered circular deck, protruding from the floater or by emplacing the hydrogen plant inside the floater [7]. Nevertheless, the added mass on the floater and the change of the floater structure may have an adverse impact on the spar buoy floater stability [43]. In addition, since the current hydrogen production components have a large area footprint, specialised solutions should emerge for spar-buoy specific applications [7]. Thus, since in situ hydrogen production is currently difficult to be implemented on spar buoy FOWT, this type of floater will not be considered in this project.

Furthermore, a **TLP** floater is a high buoyancy and low mass structure, which is secured in place via high tension, bottom anchored mooring lines [43]. Its construction and assembly is a straightforward and not material-intensive task, due to its straightforward design [41]. Moreover, the wind turbine components can be installed at the production site and then be towed to the installation site [43]. Due to its design, it can be installed in relatively shallow depths, starting from 50 m, but due to the required mooring tension, the installation depths are limited to 150 m [41]. Nonetheless, the TLP floater transport and on-site installation is more difficult, when compared with the semi-submersible and spar buoy floaters because the balance of the floater is deeply influenced by the mooring tension [43]. Therefore, both practices may require additional equipment so as to ensure that the floater is well balanced. This, in combination with the high strength requirements of the mooring equipment, leads to increased CAPEX and operational expenditure (OPEX) for the TLP, which are higher than the other floater designs [41].

It should be highlighted that, due to its design, the TLP is prone to high frequency excitations [43], which are detrimental for the wind turbine. Finally, the mooring lines should always be in tension, which signifies the need for their safe anchoring at the sea bottom [44]. As a result, the TLP platform is unsuitable for locations near seismogenic layers [44]. All in all, the TLP floater has critical issues with its stability under its tow to the installation site and under mooring-line snapping conditions, which may both cause damage to the wind turbine and the sensitive hydrogen production components. For the aforementioned reasons, the TLP is deemed as unsuitable for coupling a FOWT with in situ hydrogen production.

Last but not least, a **semi-submersible floater** comprises of three vertical cylinders, which are connected via pontoons or braces, situated below the mean sea level (MSL) [43]. For some semi-submersible floater designs, some of the pontoons may be situated above the MSL, thereby creating a triangular beam structure on the top of the floater. The cylinders, together with the pontoons contribute to buoyancy, while the cylinders themselves provide stability to the structure [41]. The position of the floater is kept fixed by mooring lines, which are anchored on the sea bottom. The upper part of the cylinders and of the pontoons offers an unrestricted area, which can be used as a deck for the in situ hydrogen production plant. Even for small semi-submersible floaters like the one used in the WindFloat Atlantic project [45], the floater top area is around $1,100 \text{ m}^3$, which is more than enough for accommodating the hydrogen plant.

Moreover, due to the increased stability and buoyancy, the equipment can be pre-installed on the platform, and then the whole assembly can be towed to the installation site [43]. Another advantage of the semi-submersible floater is that it can be installed in depths ranging from 40-1000 m, thus being suitable for shallow and deep waters as well [41]. However, its manufacturing is more complex and more material-intensive than the spar buoy and the TLP floaters [43].

Also, attention should be given on the motions of the floater due to waves because it is more susceptible to wave loading, occurring to its configuration [43]. Nevertheless, due to its ability to accommodate the hydrogen production facility, with relative straightforward and cheap modifications, this type of floater will be the baseline floater of this project.

2.4 FOWT Description

The FOWT that will be used in this project is the IEA Wind 15 MW reference turbine (RWT), developed by NREL, DTU and the University of Maine [46]. It is a direct-drive wind turbine with a rotor diameter of 240 m, a hub height of 150 m and cut-in and cut-out wind speeds of 3 m/s and 25 m/s respectively. The rated wind speed of the turbine for BF applications is 10.59 m/s. The choice of this turbine is driven by the fact that it is an advanced design for the following years. However, it is suggested that its design needs additional optimization in the case of being used in floating offshore applications [46]. More information about the turbine can be found in its technical report [46].

As mentioned in Section 2.3, the floater, which is the most suitable for accommodating the in situ hydrogen production plant, is the semi-submersible. As a result, semi-submersible floaters, compatible with the IEA Wind 15 MW turbine should be sought. One design, which can be used with this turbine is the UMaine VoltturnUS-S reference semi-submersible floater, developed by the University of Maine and designed for the environmental conditions of the US East Coast [47]. The reason for choosing this floater is twofold; not only it is designed to be coupled with the IEA Wind 15 MW reference turbine, but also it is not actively ballasted, which would result in increased model complexity. In addition, according to Allen et al. (2020), the physical dimensions of the UMaine VoltturnUS-S semi-submersible floater are $90.1 \times 102.1 \times 290$ (l x w x h) and its weight, including the turbine is nearly 21,000 t [47]. A more detailed description about the design of the UMaine Voltturn US-S semi-submersible floater is presented in its design report [47].

2.5 Dimensioning of the In Situ Hydrogen Production Plant

After determining the components of the decentralised green hydrogen production, which is situated on the floater of a FOWT, it is crucial to provide a preliminary estimation of their rated power. Thus, information can be obtained about their physical dimensions and their weight. First, the electrolyser capacity should be decided according to the balance between the unused electrolyser capacity and the amount of curtailed power. On the one hand, if the electrolyser capacity is the same with the rated power of the wind turbine, the electrolyser will be oversized, since wind turbines operate at a power output lower than their rated one for a large amount of time in a year. This will result in a substantial increase of LCoH because the oversized electrolyser will yield higher CAPEX and OPEX, while at the same time producing lower amounts of energy.

On the other hand, if the electrolyser capacity is too small, the wind turbine will produce excess electricity, which is likely to be curtailed and thus incurring monetary losses for the plant owner. A possible solution to curtailment would be the use of battery storage, but this will reduce the efficiency of the green hydrogen production process due to their round trip efficiency and their degradation over the years [48]. Therefore, there is an optimal relationship between the rated power of the electrolyser and of the wind turbine, which will be installed on the floater.

Using data of existing offshore wind farms in the Netherlands, it is estimated that the optimal

electrolyser size should be 80% of the rated power of the wind turbine [31]. In this way, not only LCoH is reduced, but also curtailment is estimated to be minimised to around 6% [31]. As a result, the preliminary capacity of the electrolyser, which will be considered in this project, is 12 MW. By having the electrolyser capacity as an input, commercially available PEM electrolyser solutions are evaluated because they present the only way to gain an insight on the different components dimensions and technical specifications.

The literature review showed that a commercially mature solution for PEM electrolysis is the Siemens Silyzer family of electrolysers [11]. More specifically, the Silyzer 200 model [49] stack has a rated power of 1.25 MW, a rated hydrogen production of 20 kg/h and a water requirement of 340 l/h at rated power. Considering that the preliminary estimation of the electrolyser capacity is 12 MW, 10 Silyzer 200 electrolysers are considered in this project, which have a combined rated power of 12.5 MW. However, the number of stacks may need additional optimization considering whether the turbine can support the other ancillary devices.

For the RO unit, commercially available solutions are sought as well in order to supply the electrolyser's water requirement of 3400 l/h. In this direction, the Culligan IW EVO 5 RO desalination unit is used, which has a rated water output of 5000 l/h, making it suitable to cover the water need of the PEM electrolysers [50]. Additionally, a typical seawater lift pump is considered to be integrated with the desalination plant, whose rated power and weight are 50 kW and 150 kg respectively [51]. Both figures will be included in the weight and the power consumption of the RO plant. Although its rated water output is higher than the requirement of the electrolysers, its weight may be all-inclusive for the piping to the electrolyser stacks.

The next step of the analysis is the determination of the size of the compressor. It should be noted that, due to the small particle size of hydrogen, piston compressors are used instead of regular centrifugal ones [52]. According to the PEM electrolyser datasheet, hydrogen exits the PEM electrolyser at a temperature of 65°C and a pressure of 35 bar, while after the compressor, the pressure is considered to be 100 bar. Using CoolProp and assuming an compressor isentropic efficiency of 90% [53], the difference in enthalpy in the two sides of the compressor is $6.92 \cdot 10^6$ J/kg. Using the total hydrogen mass flow of 200 kg/h and a typical piston compressor efficiency of 0.85 [54], the required power for the compressor is 450 kW. However, due to the unavailability of literature regarding such large compressors, it is assumed that the hydrogen from each stack will be pressurised via separate compressors, whose total power consumption is the one calculated before. In this way, the RIX 4V4BG gas compressor will be used [31].

Furthermore, since electrolysers operate at DC current, while the wind turbine and all other components of the hydrogen production plant are AC devices, a full scale power converter is needed. Also, the use of the converter is mandatory because the AC components operate at different voltage levels and frequencies. For simplification reasons, it is assumed that one centralised full-scale converter is responsible for setting the correct voltage and frequency values for the AC and DC buses. However, it should be noted that this assumption may lead to oversimplification because the converter topology may be more complicated, due to the different AC voltage levels and frequencies, in which the different components work.

In addition, a preliminary decision about the converter size should be taken. Although this would involve detailed power flow calculations, which should involve all the components of the in situ hydrogen plant, it is assumed that the converter size will be 15 MW, equal to the wind turbine rated electrical power. This is a high accuracy assumption because the summation of the rated capacities of all system components is about 13 MW, while the mismatch between the wind turbine generation and local consumption will be fed in a battery. Nevertheless, the literature review showed that, currently there are no commercially available converters in the

power range of 15 MW, while large offshore wind turbines such as the GE Haliade X-13 MW are coupled with ABB PCS6000 full scale converters [55], whose maximum capacity is 12 MW [56]. To tackle this issue, the weight, the dimensions and the auxiliary power supply of the ABB PCS6000-12 MW will be upscaled according to their power ratings, using a factor of 15/12 so as to provide an estimation of the hypothetical 15 MW converter, considered in this project.

The last step in dimensioning the system is the estimation of the battery capacity. Battery storage is essential for the system because, not only it can store the mismatch between the power generated by the wind turbine and the power consumed by the load, but it can constitute a backup source to power the hydrogen production components at periods with low wind speeds [7]. Also, batteries are useful in the power system shutdown phase because (i) they supply electricity to produce heat with a view of avoiding water freezing inside the electrolyser tubes [57], (ii) they are used to power necessary control systems of the wind turbine and the hydrogen plant [7] and (iii) they provide electricity for scheduled maintenance works on the wind turbine and the components of hydrogen plant [7]. The battery will be dimensioned according to the difference between the power generated by the wind turbine after the converter ($15 \cdot 0.98 = 14.7$ MW) and the total load of the hydrogen plant (~13 MW). Therefore, a battery capacity of around 1.7 MW is required. A commercially available solution for batteries in this power rating is the Tesla Megapack. It has a capacity of 3 MWh and a converter rating of 1.5 MW [58], making this battery suitable for the application examined in this project.

The rationale of this subsection results in having the actual dimensions and the added weight of the in situ hydrogen production facility, which will be added on the FOWT model considered in this project. The physical dimensions, the weight and the power rating of all in-situ hydrogen production components are summarised in Table 2.1. Finally, it should be noted that the mass per length of the catenary riser is approximately eight times lower than that of the mooring lines [40, 47], whereas the added mass per length of the compressed hydrogen, which is transferred in the risers is calculated to be negligible, when compared with the "dry" riser mass per length. Therefore, in this project, it is anticipated that the catenary riser mass is likely to have an insignificant effect on the floater added mass and for this reason, no modeling of the catenary riser will be done.

Table 2.1: Physical dimensions, weight and power consumption of components constituting the in situ hydrogen production plant, added on the FOWT considered in this project.

Component	Dimensions (m x m x m)	Weight (t)	Power (MW)
Electrolysis Plant	6.30 x 31.00 x 3.00	170	12.50
RO Unit (incl. Seawater Lift Pump)	4.70 x 1.20 x 1.90	0.8	0.054
Compression Unit	1.00 x 10.60 x 1.20	7.5	0.45
Full Scale Power Converter	7.45 x 1.60 x 3.08	9.1	0.015
Battery Storage	7.10 x 1.60 x 2.40	23.1	1.5
Total	N/A	210.5	14.52

3 | Research Methodology

Chapter 3 provides information about the software and the inputs used for conducting the necessary simulations for this thesis project. More specifically, Section 3.1 gives a brief description of OpenFAST, which was used in the project followed by Section 3.2, in which all necessary inputs to the simulations are discussed. Then, Section 3.3 presents the wind, wave and turbulence conditions, considered as baseline for answering the main research question and the sub-questions of this project. In addition, Section 3.4 examines the wind turbine controller characteristics, which affect the FOWT's power production. Finally, Section 3.5 discusses the methodology for altering the UMaine semi-submersible floater input files so as to incorporate the added mass and the inertia of the in situ hydrogen plant in the OpenFAST model.

3.1 Software Description

In order to assess the effect of the floater motion on the performance of the FOWT, OpenFAST is used. OpenFAST (Fatigue, Aerodynamics, Structures and Turbulence) is an open-source engineering tool, used for simulation of wind turbine operation in the time domain [59]. It is developed by NREL and it consists of a variety of models, namely: (i) aerodynamics models, (ii) structural (elastic) models, (iii) servo models, which simulate the controller and the electrical system of the turbine, and (iv) hydrodynamic models, when offshore turbines are concerned. In this way, the simulation package is able to conduct coupled aero-elasto-servo-hydro simulations, by which the power production, the motion and the loads sustained by the turbine can be studied and assessed.

In addition, the aerodynamics model implements either the blade element momentum (BEM) theory [60] or the Convecting Lagrangian Filaments (OLAF) theory [61]. In this project, the former is used. For the hydrodynamics model, the solution of the Morison [62] or the Cummins [63] equation is used, depending on the floater [64]. More information about the hydrodynamic modelling in OpenFAST can be found in the documentation of OpenFAST [65] and in the work of Jonkman, (2007) [59].

OpenFAST incorporates several submodules, which are interfaced via a driver/coupler program. The submodules used by OpenFAST in this project are the following [65]: (i) AeroDyn v15, (ii) ElastoDyn, (iii) InflowWind, (iv) ServoDyn, (v) HydroDyn, (vi) MoorDyn. All six submodules are executed simultaneously during the simulation and they exchange information via the driver program, therefore contributing to combined simulations. The modelling procedure of OpenFAST and the operation of the aforementioned modules is presented in the OpenFAST documentation [65], where the reader can deepen into the mathematical expressions and all hypotheses and inputs used in the simulations conducted for this thesis project.

3.2 Simulation Setup

3.2.1 General Information

For all OpenFAST simulations conducted in this project, the BEM solution, obtained from OpenFAST is corrected in the three-dimensional space via enabling the Prandtl tip loss, Prandtl hub loss and Pitt and Peters skewed wake corrections, while the unsteady aerodynamic model of Beddoes-Leishman is used to incorporate dynamic flow phenomena such as dynamic stall. It should be noted that no tower shadow effects are considered in this project. As far as the simulation time is concerned, IEC 61400-3 prescribes that the simulation length should be at least 10 min for each mean hub height wind speed and sea state examined [22]. Also, even though the initial conditions for the simulated DoFs in ElastoDyn are set according to their expected values for the simulated wind/wave conditions, appropriate simulation time should be discarded in order not to include startup transients [22].

In this direction, since the surge and sway natural frequencies of the UMaine Voltturn US-S semi-submersible floater are the lowest observed between all DoFs and equal to 0.007 Hz, the free decay tests of the aforementioned DoFs, presented in [47], suggest that the floater oscillations under no wind conditions damp out at a time of nearly 400 s. Hence, in order to increase the results' confidence of not including transient FOWT response, the first 400 s of all simulations in steady and turbulent wind conditions were discarded. In addition, under steady wind conditions, IEC TS 61400-3-2:2019 prescribes that a simulation time of 10 min or 600 s is deemed to produce valid results [66] because the simulations should account for the stochastic nature of sea conditions. Hence, the total simulation time for steady wind conditions is 1000 s. Finally, the average and the standard deviation values of all variables considered in this project are calculated considering the entire simulation time of 600 s.

When turbulent wind conditions are considered, IEC 61400-3 proposes that the total simulation time should be at least 1 h so as that the results are statistically reliable [22]. However, since this project is mainly concerned about the FOWT power generation and AEP figures instead of the FOWT ultimate and fatigue loading, the simulation time was opted to be the lowest possible, i.e. 1 h. In addition, although 61400-3 standard recommends to run 6 10-min simulations at different seeds, Stewart et al. (2013) [67] and Haid et al. (2013) [68] propose that, instead of running a large amount of 10-min simulations, a smaller amount of larger duration simulations can be run as well. In this direction, for the studying of turbulent wind conditions, three 20-min (1200 s) simulations were run, using three random wind seeds, while the wave seed was the same for all simulations. However, as mentioned before, the first 400 s of the simulations were discarded, raising the total turbulence simulation time to 1600 s.

Nevertheless, this approach is not in accordance with IEC 61400-3 standard, since, three wave seeds should be considered as well. In this case, the three wave seeds should be simulated for the same turbulence seed, raising the amount of turbulence simulations per wind speed to nine and to three for steady wind. Thus, the total number of simulations, that should be conducted for this project, would have increased exponentially, requiring a lot of computational effort and storage and possibly the use of a second computer, which was constrained due to the work from home nature of COVID-19 pandemic. It should be noted that the simulation of one wave seed is likely not to hinder the validity of the results, since not only the general trends studied in this project can be clearly depicted using only one wave seed. Also, the simulation of multiple wave seeds is critical in the case of investigation of FOWT ultimate and fatigue loading.

As in the case of steady wind, under turbulence, the calculation of the average values of the variables used for producing the results of this project are obtained via averaging the average

values of the 1200 s simulation time over the three seeds. For the standard deviation, the maximum standard deviation of the three seeds over the 1200 s time period is concerned, since it can lead to more conservative results. For the same reason, the minimum and maximum values of the studied variables are obtained via calculating the minimum of the minima and the maximum of the maxima observed for the three seeds under the simulation time of 1200 s.

In addition, as far as the wind field is concerned, for a preliminary analysis of the FOWT behaviour, steady wind fields are used. However, to answer sub-question 4 and to quantify the benefits of a possible aerodynamic redesign, the FOWT is subjected to turbulent wind fields using the Mann turbulence model [69]. As recommended by the IEC 61400-1 standard, for turbulent wind simulations, the shear parameter for the Mann turbulence spectrum has a value of 3.9, while the longitudinal turbulence scale parameter is equal to 29.4 m [66]. The simulated wind speeds are divided into 3 classes, namely [4-10], [10-15], and [15-25] m/s, with a view to lowering the amount of Mann turbulence boxes needed for the analysis, thus saving time, computational effort and storage space.

A dedicated box is used for the near rated wind speed region (10-15 m/s) because many of the critical operational events of the FOWT take place in this wind speed class. In order to generate the Mann turbulence boxes, the OpenFAST default simulation time step of 0.025 s and the total turbulence simulation time of 1600 s are used, while attention is given on the x-direction part of the box, which is aligned with the wind direction. More specifically, the turbulence box needs to have finer resolution in the x-direction than in y and z ones, because it is more critical in describing the turbulence experienced by the rotor.

Then, according to the Mann turbulence box methodology, the lowest wind speed of each bin determines the maximum acceptable resolution of each box, since the number of simulation time steps per box plane should be lower than 3. In other case, the box resolution becomes too coarse, thereby reducing the simulation accuracy. Hence, the maximum acceptable Mann turbulence box x-direction step ($d_{x,max}$) is given by Equation 3.2.1.

$$d_{x,max} = 3dt_{sim}U_{box,min} \quad (3.2.1)$$

where dt_{sim} is the simulation time step and $U_{box,min}$ the minimum wind speed of each Mann turbulence box. Moreover, the maximum wind speed of each class determines the length of each Mann turbulence box because the box should not repeat itself, which will affect the frequency content of the wind field. The next step for the determination of the Mann Turbulence box step in x-direction is to select a specific amount of nodes. Thus, the x-direction step (d_x) is determined by Equation 3.2.2.

$$d_x = U_{box,max}\Delta t/n_x \quad (3.2.2)$$

where $U_{box,max}$ is the maximum wind speed of each box, Δt the total simulation time, including the transient time and n_x the number of nodes in x-direction. Finally, the obtained x-direction Mann turbulence box step should be lower than the maximum acceptable resolution in this direction. In any other case, the number of nodes or the simulation time should be adjusted for satisfying the aforementioned criterion. As far as the Mann turbulence box y and z directions are used, they are not so critical for describing the wind field, so 64 nodes are used with a box step of 4.17 m, which is nearly equal to the maximum chord length of the IEA 15 MW RWT.

The iterative procedure, which was previously described, concludes that for a simulation time

of 1600 s and for a simulation time step of 0.025 s, 65536 nodes are required in the x-direction of the Mann Turbulence box for all wind speed classes. Hence, the dimensions of the Mann turbulence boxes used in this project, for wind speed classes [4-10],[10-15] and [15-25] m/s are 16000 x 262.71 x 262.71, 24000 x 262.71 x 262.71 and 40000 x 262.71 x 262.71 (m x m x m) respectively. More information about the Mann turbulence box generation can be found in Table 3.1. Finally, as proposed by 61400-1 standard, the turbulence in y and z directions (σ_y and σ_z respectively) are associated via the turbulence in x axis (σ_x) via Equations 3.2.3a and 3.2.3b respectively [70].

$$\sigma_y = 0.7\sigma_x \quad (3.2.3a)$$

$$\sigma_z = 0.5\sigma_x \quad (3.2.3b)$$

Table 3.1: Mann Turbulence box parameters for the three wind speed classes examined.

Wind Speed Class (m/s)	n_x (-)	$n_y = n_z$ (-)	d_x (m)	d_y (m)	d_z (m)
[4-10]	65536	64	0.2441	4.17	4.17
[10-15]	65536	64	0.3662	4.17	4.17
[15-25]	65536	64	0.6104	4.17	4.17

For the statistical analysis of the results under turbulence, the mean value of each parameter, examined in this project is the mean of the three seeds and the standard deviation is equal to the maximum standard deviation of each seed, so as to increase the results' confidence. As far as the minimum and maximum values of the indices of this project, aligned with the standard deviation approach, the minima and maxima of each of the three seeds are used. Finally, since the FOWT is free to move, spanwise blade parameters like angle of attack (AoA), inflow angle, and blade forces, are averaged over the three blades with the view of minimising the effect of the FOWT movement inside the wind field.

It should be noted, that wind shear is incorporated in simulations using the power law, which is given by Equation 3.2.4. This choice is made due to the fact that it is more accurate for heights higher than 60 m [71], while the IEA 15 RWT has a hub height of 150 m.

$$U(h) = U_{ref} \left(\frac{h}{H_{hub}} \right)^\gamma \quad (3.2.4)$$

As far as the incident wave kinematics are concerned, the JONSWAP wave spectrum is used, with a peak shape parameter given by the recommendation of IEC 61400-3 Ed.1 standard and by the simulated significant wave height and peak spectral period values [22]. In addition, the wave spectrum lower and upper frequency limits are set to 0 and 6.283 rad/s respectively, in order to examine all possible wave frequencies, which can excite the floater and the turbine. It should be noted that, for the scope of this project, in addition to first order waves, second order waves are considered as well. More specifically, difference-frequency and sum-frequency second order waves are incorporated in HydroDyn, with frequencies ranging in the intervals [0,0.738] rad/ and [0.314,3.2] rad/s respectively.

Furthermore, it should be mentioned that, to increase simulation modularity and simplicity, when simulations for the BF offshore wind turbine are conducted, the platform six DoFs, HydroDyn and MoorDyn modules are disabled, whereas the ElastoDyn initial conditions and

the controller used in ServoDyn are the ones for the monopile offshore wind turbine. Although this approach tends to be not realistic, because no hydrodynamics are simulated for the BF wind turbine, the discrepancies regarding power production are deemed to be low, therefore pointing that it is a correct solution. In addition, BF hydrodynamics should be examined in the case of ultimate limit and fatigue analysis, which outside of the scope of this project.

Finally, for the static floater pitch simulations, the floater DoFs and Hydrodyn are turned off with a view to understand the effect of the static floater pitch to the power production of the FOWT. In addition, the floater DoFs initial conditions will be set according to those of the monopile model, with the exception of the floater pitch angle, which will have a variable for each wind speed, while being constant with time. Thus, a decoupling from the dynamic floater motion will be done.

3.2.2 Convergence Analysis

Nevertheless, the non-consideration of the first 400 s of the simulations under both steady and turbulent wind conditions should be closely examined via a convergence analysis for both operational regimes. This stems from the fact that the selection of 400 s of the steady and turbulent wind simulations to account for simulation transients considered the floater alone, without taking into account the fully-coupled wind turbine-floater-mooring line model. Also, the non-inclusion of transient response after the first 400 s of the simulations should be verified for the variables considered in this project. For this reason, the generator power, the rotational speed, the blade and floater pitch angles, the spanwise AoA and the spanwise in plane and out of plane forces are considered in the convergence analysis.

Yet, other variables of this project such as the inflow angle are directly or indirectly associated with the aforementioned variables, so they do not need to be individually examined. As far as the spanwise variables are concerned, only their time series at the radial position of 0.715 is examined, since this radial position is considered to be representative of inboard and outboard blade elements. In addition, the convergence analysis is performed for the wind speed of 4 m/s, which is the nearest wind speed to the cut-in wind speed (3 m/s) and for one random wind speed in the peak shaver region, i.e. 10.5 m/s, since this project mainly focuses on the partial load region. Last but not least, for both steady and turbulent wind conditions, the examined variables are thought to have converged at their steady state (SS) value if their time-varying error compared to their steady state values is lower than 5%. Also, in this case, no transient response is thought to be included in their SS value.

As far as the convergence analysis at steady wind is concerned, steady state is thought to be achieved at the last 200 s of the simulation. Therefore, the SS values of all variables considered in the convergence analysis are calculated via averaging their time series between 800 and 1000 s. Then, the moving average of the individual time series of the variables is calculated for each time step using an averaging time period of 200 s, equal with the SS averaging time. The relative error of the moving average of each time step compared to the SS value is calculated for each simulation variable, with the view of comparing the time-varying errors to the value of 5%. The results of the convergence analysis for steady wind conditions and for wind speeds 4 m/s and 10.5 m/s are presented in Figures 3.1a and 3.1b respectively.

The examination of Figures 3.1a and 3.1b shows that at both 4 m/s and 10.5 m/s, the relative errors of all variables considered in this project are well below 5%. In fact, for the wind speed of 4 m/s, which is near the cut-in wind speed, the relative errors are higher than the ones at 10.5 m/s by a factor of 6.7 to 1 at maximum. Nevertheless, at both wind speeds examined, the

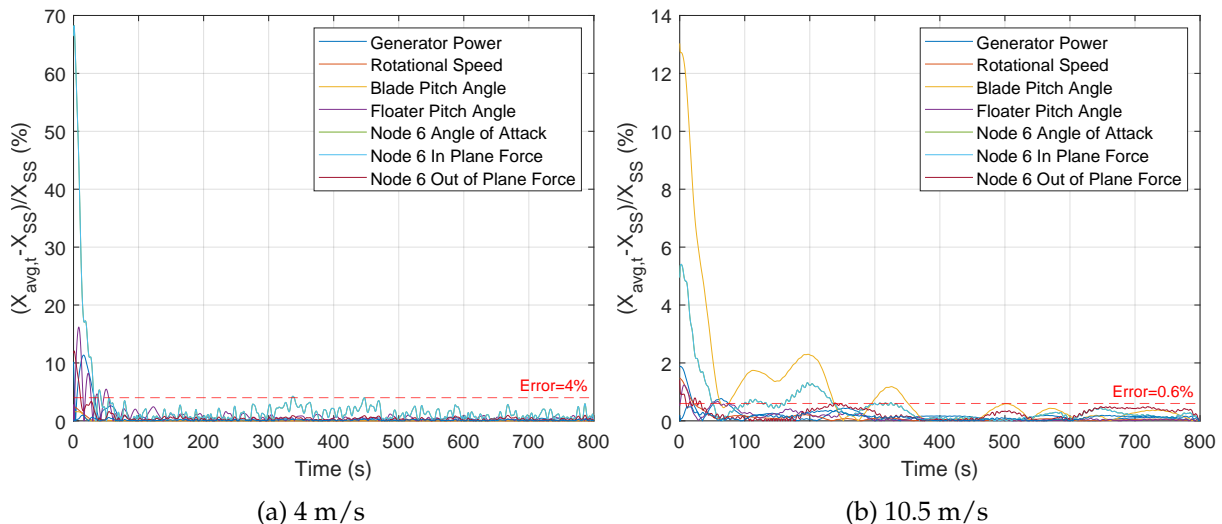


Figure 3.1: Time-varying error compared to the steady state value of for all simulation variables considered in the convergence analysis, under steady wind conditions.

majority of the useful quantities of this project converge to values that deviate at maximum 1% from their SS counterparts, while at 10.5 m/s, the relative errors are always lower than 0.6%. Furthermore, Figures 3.1a and 3.1b show that the transient response of all variables disappear after approximately 200 s.

However, this is not true for the case of the blade pitch angle error time series at 10.5 m/s, where transients fade out at approximately 370 s. In this case, the relative errors are more or less lower than nearly 2%. Therefore, since it is always lower than the maximum error of 5%, observed at 4 m/s, it is likely not to affect the simulation convergence after 200 s. To conclude, the discardment of the first 400 s of the simulations for each studied simulation variable under steady wind is deemed to be a transient overestimation, since the actual transient time is approximately 200 s. Hence, for steady wind conditions, the simulation time could be 800 s rather than 1000 s. However, at any case, the relative errors of all variables are lower than the acceptable error of 5%, thereby rendering the results of steady wind simulations as accurate.

Furthermore, under turbulence, the convergence analysis should be done for the maximum turbulence intensity (TI) considered in this project, i.e. 20%. Yet, in this case, the calculation of the SS values and of the moving average at each timestep for all variables considered in the analysis should be done using a larger time interval than in steady wind. This stems from the fact that, for an averaging time interval lower than 1035 s, the relative errors of various variables of the analysis were found to be higher than the acceptable 5%, set for this project. Hence, an averaging time of 1100 s is selected. The results of the convergence analysis under a TI of 20% are shown at Figures 3.2a and 3.2b for wind speeds 4 m/s and 10.5 m/s respectively.

It can be clearly seen for both wind speeds examined, the maximum error, compared to the SS value of all variables of the convergence analysis is lower than 2.8% after 400 s. In fact, all variables, with the exception of the angle of attack at 4 m/s and of the blade pitch angle at 10.5 m/s present even lower errors after 400 s. The large variations of the aforementioned simulation variables is likely connected to their large deviation from their mean values, observed from their corresponding time series.

Still, Figures 3.2a and 3.2b depict that for nearly all variables, which are studied in the convergence analysis, their transients fade away after approximately 200 s. Therefore even for a

TI value of 20%, the errors of the studied variables not only are lower than 5%, but also their transient behavior is deemed not to be considered in the results in case the the first 400 s of the turbulent wind simulations are discarded. It is worth mentioning that, since the results of this project are calculated via averaging the whole 1200 s of turbulent wind simulations, thereby considering a larger SS time interval than 1100s, the obtained simulation errors are likely to be lower than 2.8%. Finally, same results are obtained for smaller TI values, such as 10%, but in this case, as shown in Figures 3.3a and 3.3b for the convergence of variables at TI=10%, the maximum errors are even lower than the ones observed for TI 20%.

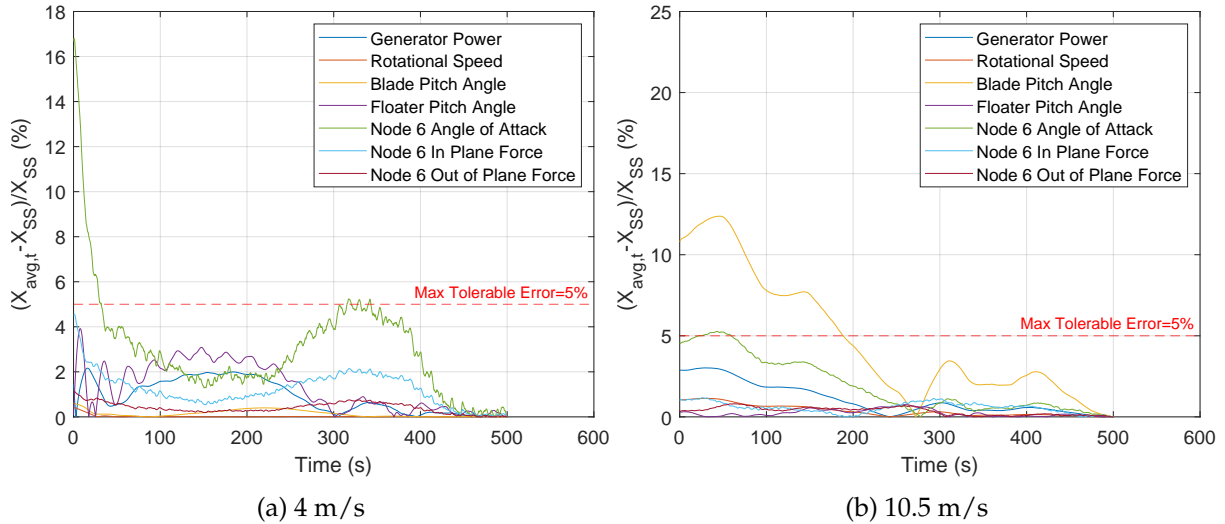


Figure 3.2: Time-varying error compared to the steady state value of all simulation variables considered in the convergence analysis, under a TI value of 20%.

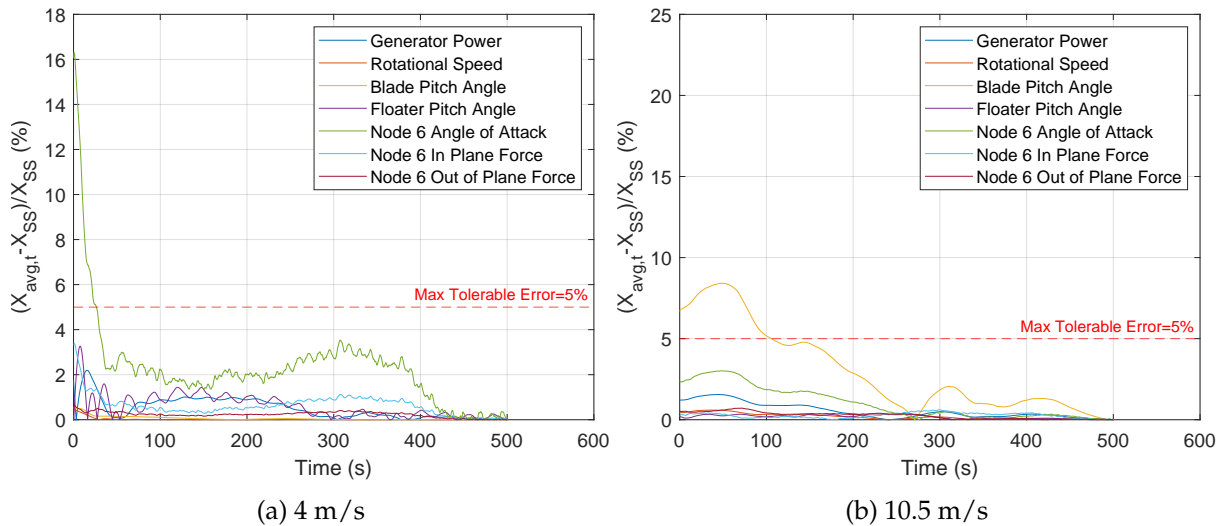


Figure 3.3: Time-varying error compared to the steady state value of all simulation variables considered in the convergence analysis, under a TI value of 10%.

3.3 Environmental Conditions

One of the most important aspects for this project is to determine the wind and wave conditions, for which OpenFAST simulations will be conducted. The parameters that describe the FOWT environmental conditions are [59]: (i) the wind speed (U), (ii) the significant wave height (H_s), (iii) the peak spectral period (T_p) and (iv) the wind/wave misalignment θ . Since UMaine

Volturn US-S semi-submersible floater is designed for environmental conditions of a general US East Coast site [47], it is thought that the environmental conditions used in this project should be site-representative. Stewart et al. (2015) created a typical offshore metocean dataset for a general US East Coast offshore site [72], in which the measured data were used to create conditional probabilities for describing the environmental conditions at this site.

In addition, Stewart et al. (2015) estimated the most expected combinations of H_s , T_p and θ depending on the wind speed U . The results are presented in Table 3.2. For conducting the FOWT simulations, each simulated wind speed will consider the H_s , T_p and θ values of Table 3.2, rendering the FOWT power generation dependent on all environmental conditions. It should be noted that, due to the usage of conditional probabilities, the accurate calculation of the annual energy production (AEP) of the FOWT would require the consideration of the power produced by the turbine and the joint probability density function value at all combinations of the four wind/wave parameters. This would require 14^4 simulations, which are obviously time consuming.

Table 3.2: Most expected combinations of wind speed U , significant wave height H_s , peak spectral period T_p and wind/wave misalignment θ of the general US East Coast site considered in this project. Source: [72].

U (m/s)	H_s (m)	T_p (s)	θ (deg)
4	1.10	8.52	-20.82
6	1.18	8.31	-28.55
8	1.32	8.01	-27.38
9	1.43	7.83	-23.39
10	1.54	7.65	-19.40
10.5	1.61	7.60	-17.63
11	1.69	7.55	-15.85
12	1.84	7.44	-12.29
14	2.19	7.46	-10.39
16	2.60	7.64	-7.15
18	3.06	8.05	-4.81
20	3.62	8.52	-1.55
22	4.03	8.99	5.43
24	4.52	9.45	7.04

For this reason, for calculating AEP in this project, only the wind speed probability is used, which provides an average representation of the conditions at the examined site, thereby simplifying the AEP estimation process. As shown by the US East Coast metocean database, the wind speed probabilities are described by a Weibull distribution with a shape parameter of **2.12** and a scale parameter of 9.767 m/s, which is calculated for height of 90 m. Using the power law (Eq. 3.2.4) with a typical offshore site power law exponent of 0.11, the scale parameter is determined to be **10.33** m/s, whereas the shape parameter is mostly site specific, thereby not a function of the hub height. The Weibull probability density function considered for this project is depicted in Figure 3.4 .

Last but not least, the wind/wave misalignment is modeled in OpenFAST by altering the wind direction, instead of the usual method of changing the wave direction [73]. This is due to the fact that a change in the wave heading would require solving the potential flow along the floater for a wave heading different than 0° , whereas the floater is by default supplied for the solution for 0° wave direction. Therefore, in order not to create a wind direction-nacelle yaw misalignment, the rotor-nacelle assembly (RNA) yaw is set equal to the wind direction for all wind and wave

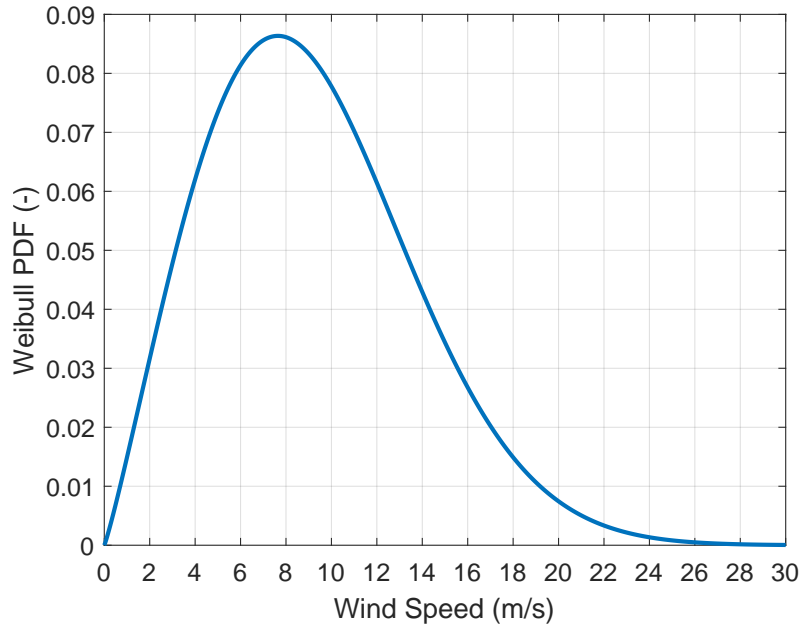


Figure 3.4: Weibull probability density function with a scale parameter of 10.33 m/s and a shape parameter of 2.12.

conditions simulated in this work.

Since TI impacts the power produced by the FOWT, the comparison of the BF and the FOWT and the possible aerodynamic redesign should be done at a specific TI value. In this project, two solutions are considered: (i) selection of the TI value prescribed by the NTM turbulence model of IEC 61400-1 ed.3 [66] for wind speeds where rated power is achieved (i.e. 12 m/s) using a class B turbine or (ii) Usage of site-specific TI values. However, as discussed in literature, the TI values predicted by IEC standards are overestimated when compared to actual measurements on various offshore sites [74]. Therefore, the second approach will be used. Measurements at US East Coast sites showed that their annual average TI value ranges from 0.08 to 0.11 [75]. This is in accordance with climate analyses of other offshore sites in different areas [74, 76], which also state that TI for offshore farms ranges between 6% and 10% for wind speeds between 12-14 m/s. Thus, the TI value that is going to be used as the baseline for this project is 10%.

3.4 Controller Description

The aerodynamic performance of a FOWT depends on the way the wind turbine controller responds to the wind field variations [77]. Therefore, it is evident that a brief description of the controller should be done, with a view of better understanding the FOWT behaviour. The IEA Wind 15 MW RWT on the UMaine semi-submersible floater uses the NREL Reference Open-Source Controller (ROSCO) [78]. For the operation of the turbine between the cut-in wind speed ($U_{\text{cut-in}}$) of 3 m/s to the cut-out wind speed ($U_{\text{cut-out}}$) of 25 m/s, the ROSCO controller uses two proportional-integral (PI) controllers. More specifically, for wind speeds ranging from $U_{\text{cut-in}}$ to the rated wind speed (U_{rated}) of 10.59 m/s, the PI generator torque regulates the rotor rotational speed with the view of maximising power extraction.

On the same time, the PI blade pitch controller is saturated at specific blade pitch angles, which ensure that the power coefficient (C_p) is maximized at the whole partial load. Under full load ($U_{\text{rated}} < U < U_{\text{cut-out}}$), the PI blade pitch controller regulates the blade pitch angle to ensure

constant power output or constant torque, depending on the controller setting. On the same time, the PI generator torque control saturates the rotor torque at its rated value.

The ROSCO controller operates under three distinct regions:(i) region 1.5, region 2 and (ii) region 3. In region 1.5, the controller tries to maximize C_p , under a minimum rotational speed constraint, which results in the turbine operating at a suboptimal tip speed ratio (TSR), while blades are constantly pitched. Moreover, in region 2, the controller tracks at the optimal TSR, which corresponds to the the optimal C_p of the rotor and to the fine blade pitch angle of 0° . Finally, region 3 is associated with power shedding via blade pitching in order to stabilise the power output of the FOWT via employing a constant torque setting. Hence, the floater stability is improved [79]. At the aforementioned regions, the controller follows the C_p surface plot, shown in Figure 3.5.

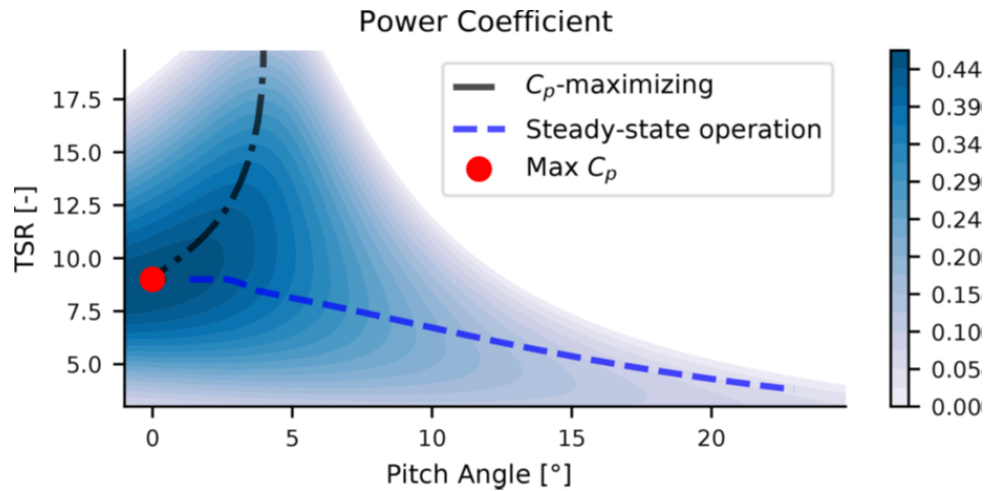


Figure 3.5: C_p surface of the IEA 15 MW RWT for steady conditions. Black dashed curve: PI blade pitch control schedule for maximizing power at region 1.5. Red point: Optimal C_p and TSR values, tracked by the controller at region 2. Blue dashed curve: C_p and TSR variation under blade pitch actuation at region 3. Source: [78]

In addition, the IEA 15 MW FOWT blade pitch controller is associated with the floater pitch motion in two ways [78]:(i) Consideration of fore-aft tower top acceleration in the PI blade pitch controller feedback signal and (ii) Minimum blade pitch saturation in order to cap the turbine thrust to a maximum value (peak shaver). For the peak shaver, the pitch angle schedule starts from 9.5 m/s onwards, by saturating the PI blade pitch controller at 1° , which becomes 5° at 12 m/s. Thus, after 9.5 m/s, the controller objective is not to track the optimal C_p but to pitch the blade with the view of keeping the turbine thrust lower to a specified setpoint.

However, as stated by Abbas et al. (2022), the peak shaver routine introduces a reduction in the power production of the FOWT, which is caused by a variety of reasons [78]. Firstly, the peak shaving routine, in addition of limiting the thrust produced by the turbine, and consequently the moment associated with the floater movement in the pitch axis, restricts the aerodynamic torque produced by the blades, which has a detrimental effect in the power generated by the FOWT. Secondly, since the peak shaver blade pitching schedule is designed for steady conditions, the peak shaver severely hampers the FOWT power under turbulence.

More specifically, the controller responds to the estimated wind speeds via following a pre-determined blade pitch angle schedule. As shown by Abbas et al. (2022), under unsteady conditions, the blade pitching is higher than needed for a specific wind speed estimate, due to slow or inaccurate wind speed prediction by the controller [78]. This stems from the fact that

the controller wind speed estimate is calculated in discrete time. Therefore, the controller caps the blade aerodynamic thrust and consequently the aerodynamic torque in lower values than the designed ones, resulting in lowering the FOWT generated power in the peak shaver region.

Furthermore, since the ROSCO controller for the IEA 15 MW FOWT is detuned with its bandwidth being below the 1st platform fore-aft natural frequency [78], the FOWT controller is slower than originally designed, which causes a slower blade pitching response in respect to the variations of the wind speed. As a result, when the inflow wind speed reduces during turbulent wind conditions, the blades are slowly pitching towards smaller angles, which results in airfoils momentarily stalling. Thereby, the aerodynamic performance of the airfoils deteriorates in terms of torque and thrust force generation. In addition, from a design standpoint, the turbine thrust value, which is taken into account in the peak shaver is multiplied by a peak shaving percentage factor, which is 0.8 for the case of the IEA 15 MW FOWT on the UMaine semi-submersible floater.

Considering the power losses occurring from the peak shaving routine and the wind speed reduction due to the static floater pitch angle, which will be thoroughly examined in Section 4.2, the FOWT achieves rated power at approximately 12 m/s and not at 10.59 m/s as the original IEA 15 MW RWT, due to the power reduction between 9.5 and 11 m/s. Nevertheless, the peak shaving effectively limits the FOWT pitch motion, which coupled with the consideration of tower top fore-aft acceleration by the controller, creates performance gains, mainly due to better FOWT stabilisation [78].

3.5 Incorporation of the In Situ Hydrogen Plant on OpenFAST Model

In order to understand the effect of the in situ hydrogen plant on the performance of the FOWT, thereby answering sub-question 3, a modification of the OpenFAST model of the Voltorn US-S semi-submersible floater is required. More specifically, it is opted not to change various operational parameters of the model, such as the deployment depth, total weight, ballast weight and configuration because no relevant information is presented in the model documentation. Therefore, the added mass of the hydrogen production components, which is 210.5 t, as per Table 2.1, will cause the floater to heave, resulting in an increased draft. As a consequence, not only the changing FOWT parameters due to the floater mass increase should be identified, but also, their new values should be calculated for the augmented floater model.

More specifically, owing to the increase of the floater draft, the tower base and top heights as well as the original floater center of gravity (CoG) will move to lower (more negative) positions in respect to the MSL. In addition, the augmented floater CoG will change due to the mass increase, as well as the volume of displaced water by the FOWT. Last but not least, the mass increase and the displacement of the original floater CoG result in an increase of the platform pitch, yaw and roll inertias with respect to the augmented floater CoG. The aforementioned changes should be calculated and then incorporated in the OpenFAST model of the FOWT.

Firstly, in order to ensure that the system floats, the total buoyancy force of the floating structure (B_{total}) should be in equilibrium with the total gravitational force of the augmented FOWT and the vertical pretension of the mooring lines, occurring due to their mass. This is described by Equation 3.5.1.

$$B_{\text{total}} = \rho_{\text{water}} \cdot g \cdot V_{\text{disp}} = (M_{\text{FOWT}} \cdot g + F_{\text{pretension}}) \quad (3.5.1)$$

where M_{FOWT} is the total FOWT mass, including the floater, wind turbine and hydrogen plant, g is the gravitational acceleration, ρ_{water} the sea water density (assumed as 1025 kg/m^3) and $F_{\text{pretension}}$ is the mooring line vertical pretension due to its gravitational force. Solving Equation 3.5.1 for V_{disp} results in calculating the displaced volume of water by the augmented platform.

In addition, to calculate the new floater draft, the dimensions and the buoyancy production characteristics of the UMaine Voltturn US-S semi-submersible floater should be identified. As it can be seen from Figure 3.6, the three pontoons of the UMaine floater are fully submerged into water, therefore they contribute to a fixed amount of buoyancy irrespective of draft. Thus, their buoyancy should be subtracted from the total buoyancy produced by the floater structure. On the other hand, the buoyant structures, which determine the floater draft, are the four cylinders comprising the floater, which are not fully submerged into water. Thus, the new floater draft (d) can be estimated from Equation 3.5.2.

$$d = (B_{\text{total}} - B_{\text{pon,total}}) / (\rho_{\text{water}} \cdot g \cdot S_{\text{col,total}}) \quad (3.5.2)$$

where $B_{\text{pon,total}}$ is the total buoyancy force from the three pontoons and $S_{\text{col,total}}$ the area of the four cylindrical columns, calculated via the floater dimensions, presented in Figure 3.6. Thus, the calculations result in a new FOWT total mass of 20303.5 t, a new draft of 20.46 m, and a new displaced water volume of 20411.46 m^3 , signifying an increase of 1.05%, 1.02% and 2.3% respectively in comparison with their values according to the original UMaine floater.

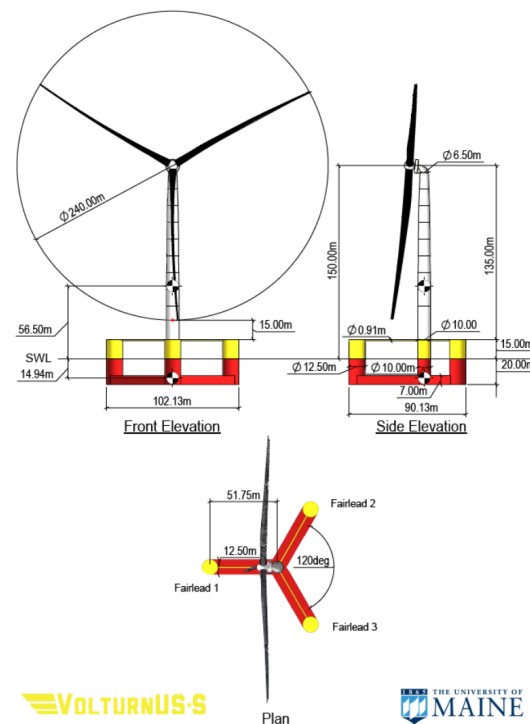


Figure 3.6: Dimensions of UMaine Voltturn US-S semi-submersible floater. The red parts of the floater are below the MSL, whereas the yellow ones are above. Source: [47].

For the calculation of the augmented floater (CoG) and roll, pitch and yaw inertias, the hydrogen components are treated as rectangular prisms, whose dimensions are presented in Table 2.1, with their CoG being at its centroid. This presents a subtle assumption that the components will be installed inside the turbine tower, as it is predicted for future in situ hydrogen topologies via FOWT [11]. However, since many components, as of 2022, are not compact enough to be

installed inside the tower, regular state-of-the-art devices will be considered in this work, even if their length from the centroid axis, exceeds the inner tower radius at its lower part. In addition, the components are placed on the floater freeboard, in order to be at a safe distance from water.

Since it is necessary for floating structures to have their neutral CoG on the z-axis, it is assumed that the CoG of the hydrogen components is situated on the z-axis, without any offset in respect to x and y axes. This assumption is made in order to decrease modelling complexity, since in other case, a reconfiguring of floater ballast may be needed because of the PEM electrolyser being largest and heavier than the other components. As a result, the z-axis coordinate of hydrogen components' CoG is equal to half of the height of the respective rectangular prism plus the new freeboard height (reduced to 14.54 m, since the floater draft increases). The positioning of the hydrogen components on the floater is depicted in Figure 3.7.

The next step for modifying the OpenFAST model is to calculate the augmented platform CoG z-axis coordinate via Equation 3.5.3:

$$z_{\text{CoG}} = \sum M_i / M_{\text{total,new}} \cdot z_{\text{CoG},i} \quad (3.5.3)$$

where M_i is the mass of each component of the augmented floater, $M_{\text{total,new}}$ the total augmented floater mass excluding the wind turbine and $z_{\text{CoG},i}$ the z-axis coordinate of the CoG of each component. It should be noted that, due to the floater heave, the original floater CoG is displaced from $z=-14.94$ m to $z=-15.40$ m. The augmented floater CoG z-axis coordinate is calculated to be $z=-15.08$ m, which is anticipated due to the mass positioning higher than MSL. Moreover, the x, y and z axis inertias ($I_{x,i}$, $I_{y,i}$ and $I_{z,i}$) of the hydrogen components in respect to a reference frame, positioned at their centroid, can be calculated via Equations 3.5.4a to 3.5.4c.

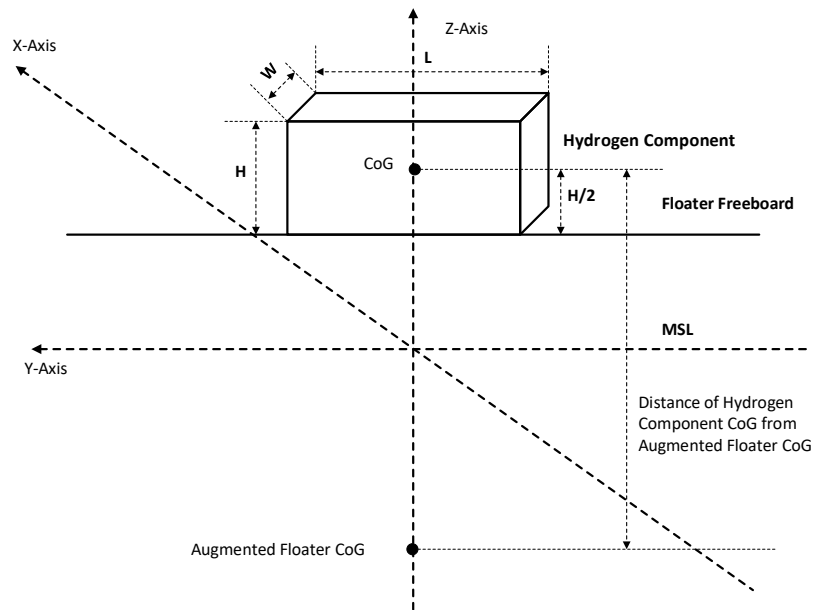


Figure 3.7: Overlapping positioning of the hydrogen production components on the floater, considering the OpenFAST reference frame.

$$I_{x,i} = \frac{1}{12} \cdot M_i (L_i^2 + H_i^2) \quad (3.5.4a)$$

$$I_{y,i} = \frac{1}{12} \cdot M_i(W_i^2 + H_i^2) \quad (3.5.4b)$$

$$I_{z,i} = \frac{1}{12} \cdot M_i(L_i^2 + W_i^2) \quad (3.5.4c)$$

where L_i , H_i and W_i is the length, height and width of each hydrogen component rectangular prism respectively. It should be noted that the coordinate system of each rectangular prism follows the same axis orientation in respect to the OpenFAST global reference frame. Nevertheless, the inertias of the original floater and the hydrogen components in respect to the three axes should be calculated in respect to the CoG of the augmented floater, which is done by applying the parallel axis theorem for each component. Then, the roll (x-axis), pitch (y-axis) and yaw (z-axis) inertias of the augmented floater in respect to its new CoG are calculated by summing the components' inertia according to the three axes. Lastly, due to floater heave, the new tower base and top heights are calculated to be 14.54 m and 143.03 m respectively.

The values of parameters relevant for the modification of the OpenFAST FOWT model, as calculated by the aforementioned process, in order to take into account the added mass of the in situ hydrogen production are presented in Table 3.3. It can be deduced that the installation of hydrogen components on the floater results in an increase of floater mass, inertia and displaced water volume by no more than 2% for each of the aforementioned quantities. As a result, it is anticipated that the in situ hydrogen plant will have a negligible effect on the FOWT motion. However, simulations should be conducted in order to highlight the hydrogen plant influence mainly on the static floater pitch angle and on the FOWT power production. The aforementioned simulation results are presented in Section 4.3 of this report.

Table 3.3: Comparison of design parameters, relevant for the modelling of FOWT in OpenFAST, for the original and the augmented floater, with differences owing to the consideration of the in situ hydrogen production plant.

	Original FOWT	Augmented FOWT	Difference (%)
Total FOWT Mass	20093.00	20303.50	1.05
Displaced Water Volume (m³)	20206.09	20411.46	1.02
Draft (m)	20.00	20.46	2.30
Floater CoG (m)	-14.94	-15.08	0.93
Freeboard Height (m)	15	14.54	-3.09
Floater Roll Inertia i.r.t. new CoG (kg m²)	1.2510E+10	1.2714E+10	1.63
Floater Pitch Inertia i.r.t. new CoG (kg m²)	1.2510E+10	1.2727E+10	1.74
Floater Yaw Inertia i.r.t new CoG (kg m²)	2.3670E+10	2.3684E+10	0.06

4 | Simulation Results

In this chapter, the effect of the floater dynamics on the aerodynamic performance of the IEA 15 MW FOWT will be investigated, while a comparison of the power production of the FOWT in respect to the BF wind turbine will be done under turbulent wind conditions. This chapter has the following structure. Section 4.1 provides an insight on the effect of wind shear on the FOWT power production, while in Section 4.2 the effect of the static floater pitch angle is investigated under variable floater pitch angle according to wind speed and under constant floater pitch angle for all examined wind speeds. Then, Section 4.3 discusses the effect of the in situ hydrogen plant on the FOWT performance. Finally, Section 4.4 presents a comparison of various performance indicators of the FOWT and the BF turbine, with a view of highlighting whether an aerodynamic redesign is needed and if yes, according to which logic.

4.1 Effect of Wind Shear

One of the parameters which influences the power produced by wind turbines is wind shear [80]. From the definition of the power law (Eq. 3.2.4), it is evident that the wind speed profile depends on the power law exponent value. More specifically, for high γ values, the wind profile becomes less steep, which results in higher wind speed variation with height. Therefore, the rotor experiences different wind speeds at various heights, which affect the blade loading and consequently the power production of the turbine. For this project, the effect of wind shear will be investigated under steady wind conditions using (i) a uniform inflow ($\gamma=0$), (ii) a sheared inflow with a $\gamma=0.11$, and (iii) a sheared inflow with $\gamma=0.3$. In addition, the FOWT will be simulated with all DoFs and the HydroDyn module turned on, so as to have a more realistic simulation of its operation. The simulation results are summarised in Figure 4.1.

As it can be seen from Figure 4.1, the power production of the FOWT is reduced due to wind shear. The power reduction increases in the case of a higher γ value. The effect of wind shear starts appearing from a wind speed of 6 m/s, but is more prevalent for wind speeds ranging from 8 m/s to 11 m/s. For the aforementioned wind speeds, although the power law exponent results in a wind speed gain for blade nodes higher than hub height, the exact opposite occurs for nodes, situated below the hub, while their wind speed is reduced more, due to the non-linear nature of the power law. As a result, the average torque per unit length produced by all blade nodes is reduced, thereby contributing to power losses.

It should be noted that, as presented in Figure 4.1, the power loss due to wind shear is small, even in the case of $\gamma=0.3$. Therefore, it can be concluded, although wind shear is acknowledged to reduce the FOWT power output, it can be neglected when studying the effect of the floater motion on the FOWT power. In order to simplify the analysis and to provide a clear view of floater motion parameters, which influence FOWT power production, **a power law exponent of 0** will be used in the simulations that will follow in next steps of this project.

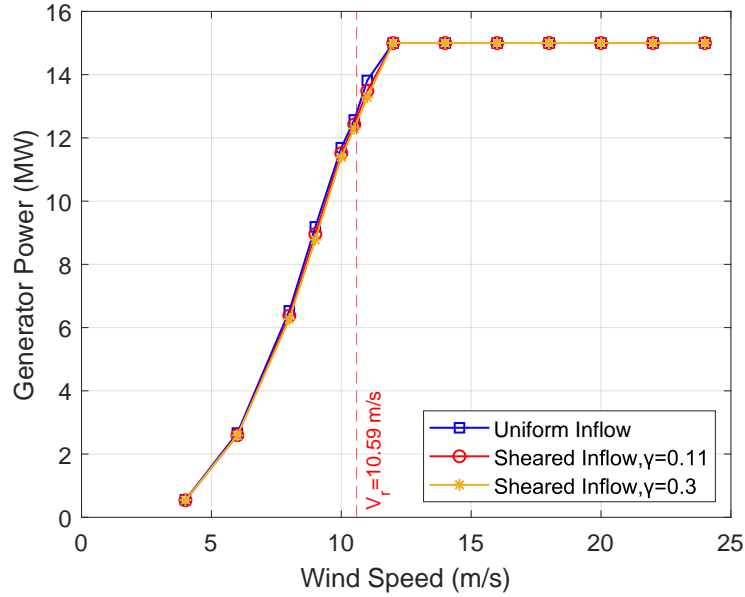


Figure 4.1: Power curves of the IEA 15 MW UMaine semi-sub FOWT for the three power law exponents examined. Blue curve: Uniform inflow, Red curve: Sheared inflow with $\gamma=0.11$. Yellow curve: Sheared inflow with $\gamma=0.3$.

4.2 Effect of Static Floater Pitch Angle on the FOWT Power

In this section, the effect of the static floater pitch angle will be investigated, so as to understand the way it affects the power production of the FOWT. To begin with, the floater pitch angle is one of the six DoFs of the FOWT and it is associated with the rotation of the whole FOWT structure in respect to y-axis. The pitch DoF as well as the other DoFs of the FOWT in the OpenFAST coordinate system are presented in Figure 4.2. More specifically, a non-zero floater pitch angle signifies that the FOWT is inclined relative to the wind field, which reduces the inflow wind speed seen by the rotor as per Equation 4.2.1.

$$U_{fl,pitch} = U \cdot \cos(\bar{\theta}_{fl,pitch}) \quad (4.2.1)$$

where $U_{fl,pitch}$ is the actual wind speed due to an average non-zero floater pitch angle $\bar{\theta}_{fl,pitch}$ and U the undisturbed wind speed at 0° platform pitch. It is evident that, when the floater and, consequently, the turbine rotor are at an angle in respect to 0° , the rotor experiences lower wind speeds, which are likely to reduce the power performance of the turbine. In addition, from Eq. 4.2.1, it is evident that as the floater pitch angle increases, the wind speed seen by the turbine decreases, signifying a larger power reduction.

For studying the effect of the static floater pitch angle on the turbine's generated power, the BF controller is used so as to decouple the simulations from the peak shaving routine. This is done in order to highlight the influence of the static floater pitch angle on the FOWT power at a more clearer way. However, even in case the peak shaver is considered, no significant discrepancies between the results are expected. It should be noted that, the simulations will consider two simulation setups for the static floater pitch angle: (i) variable floater pitch angle according to wind speed, with the floater pitch angle equal to the average values observed during FOWT simulations with the 6 DoFs and Hydrodyn turned on, (ii) fixed static pitch ranging from 0° to 10° for all wind speeds examined. The examination of the effect of the floater static pitch under

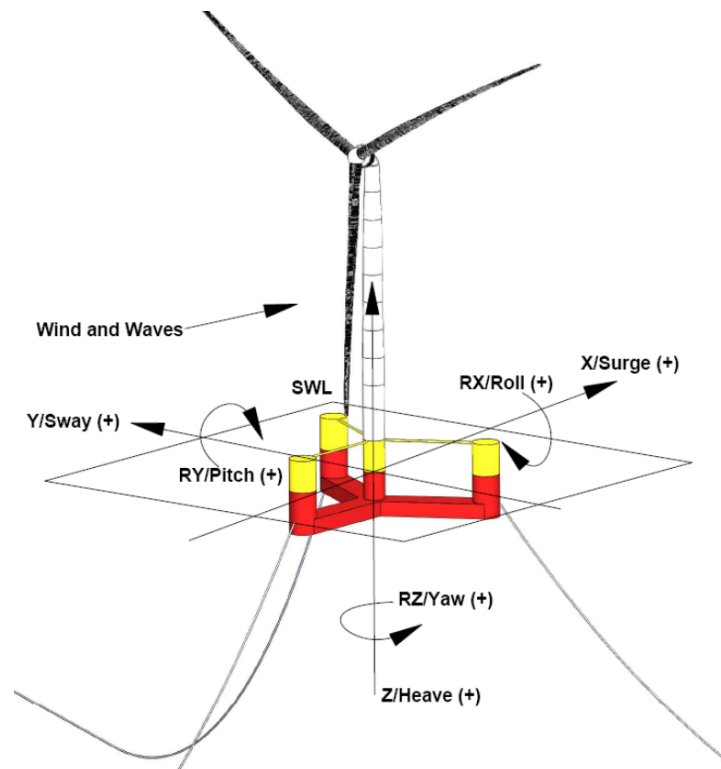


Figure 4.2: Description of the 6 degrees of freedom of the IEA 15 MW FOWT on top of the UMaine semi-submersible floater in the coordinate system of OpenFAST. Source [47].

two scenarios is done in order to take into account the normal floater pitch angle response and other extreme values, not shown during normal FOWT operation. In addition, both scenarios will be simulated in steady wind conditions, so as to have a more clearer view on the results.

4.2.1 Variable Static Floater Pitch Angle Simulations

For this simulation set, the floater pitch angles were constant for the whole simulation time and equal to the average floater pitch angles observed at the FOWT simulations at the examined wind speeds, as shown in Figure 4.3. However, it should be noted that the aforementioned floater pitch angles include the effect of the effect of the peak shaver, so as to get the actual average floater pitch angles of the FOWT. It can be clearly seen that for wind speeds up to 6 m/s, the static floater pitch angles are lower than 1° , while being negative for low wind speeds, due to gravity moments exceeding the tower top thrust moments produced at these wind speeds. Therefore the wind speed reduction, according to Equation 4.2.1, tends to be negligible. Then, for wind speeds 8 m/s to 11 m/s, the static floater pitch angles are always higher than 2° , with a maximum value of approximately 3.9° at a wind speed of 11 m/s. This observation can be attributed to high turbine loading near the rated wind speed of the FOWT.

It is worth noting that the wind speed region between 8 m/s and 11 m/s provides an insight on the peak shaver effect on the floater pitch angle. Although the static floater pitch angle rapidly increases up to 10 m/s, in the near rated region, a floater pitch angle plateau is formed, with a small deviation at 11 m/s, due to maximum FOWT loading occurring at this wind speed. Finally, from 12 m/s onwards, where FOWT rated power is achieved, the static floater pitch angle starts reducing from the maximum value of 3.9° , while being lower than 2° after 16 m/s. This observation can be attributed to the reduction of the turbine loading, owing to the increased blade pitch angle setting.

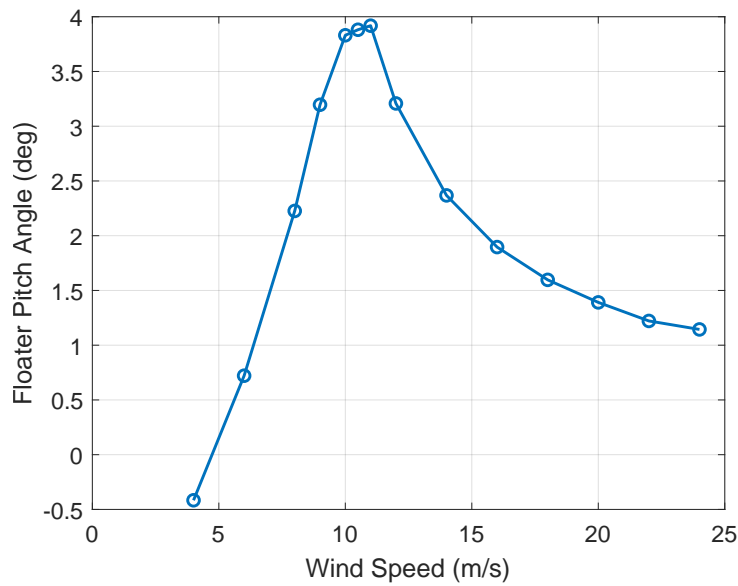


Figure 4.3: Average floater pitch angles observed during the fully-coupled FOWT simulations for a uniform wind profile and for wind speeds ranging from 4 m/s to 24 m/s.

In addition, Figure 4.4 depicts that the power production of the BF turbine under a non-zero static floater pitch angle is reduced at all wind speeds below rated (10.59 m/s). However, as shown in Figure 4.5a, the power reduction is not the same at all wind speeds. For this reason, the power deficit of the statically pitched BF turbine should be examined together with the rotor averaged wind speed deficit (presented in Figure 4.5b) and with the floater pitch angle variations. More specifically, for static floater pitch angles lower than 1° , the deficit of the rotor averaged wind speed is lower than 0.2%, thereby causing negligible power reduction. Yet, this is not the case when the static floater pitch angle exceeds 2° .

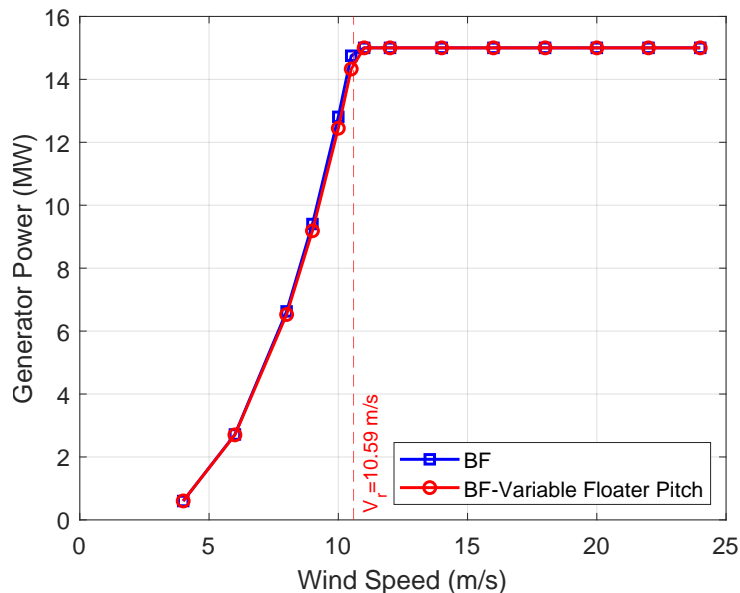


Figure 4.4: Comparison of the power curves of the IEA 15 MW RWT under BF configuration and under two scenarios: (i) fixed static floater pitch angle of 0° , (ii) variable static pitch angle according to wind speed. Blue curve: Scenario (i). Red curve: Scenario (ii).

As shown in Figure 4.5b, between 8 and 10.5 m/s, the rotor averaged wind speed reduction of the statically pitched BF turbine ranges from nearly 0.5% to 1.01%. This observation is justified

by the high static floater pitch angles occurring in this wind speed region. At the same time, the turbine power reduction ranges between 1.5% at 8 m/s, while having a maximum of 2.9% at 10.5 m/s. For wind speeds higher or equal than 11 m/s, although there is a considerable wind speed reduction, which is maximized for 12 m/s at value of 1.02%, the turbine does not experience power losses. This stems from the fact that, after 10.59 m/s, the BF turbine generator torque controller saturates at rated torque. Thus, even though from 11 m/s onwards, there is a wind speed deficit, the value of the wind speed is always higher than 10.59 m/s. Hence, rated torque and consequently rated power are achieved after 11 m/s, which are not affected by the wind speed reduction due to the static floater pitch angle.

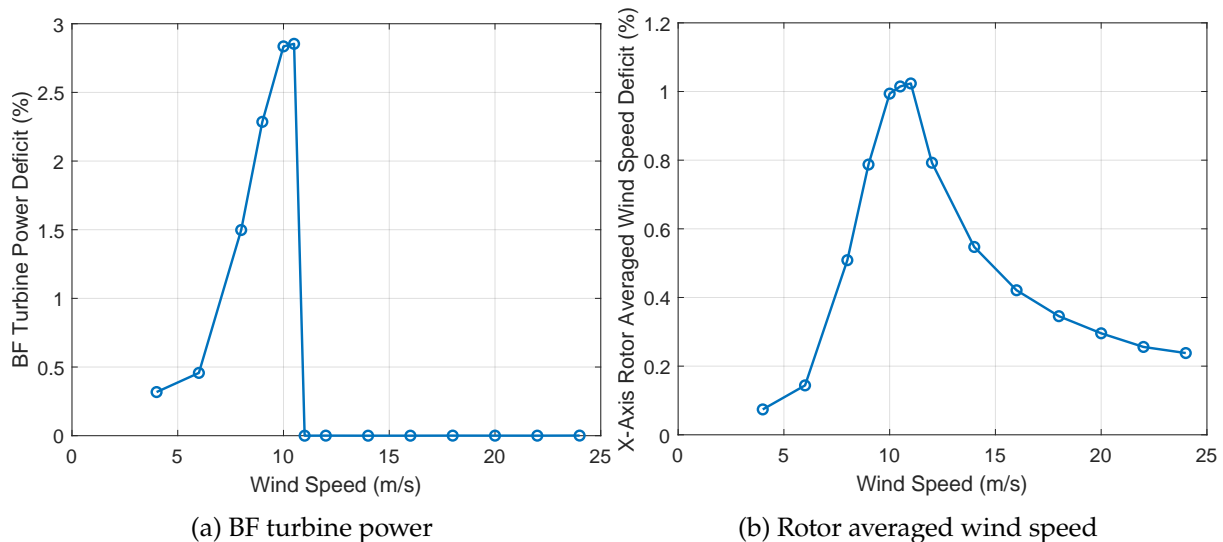


Figure 4.5: Percent difference of the generated power and the of the rotor averaged wind speed in x-axis of the BF turbine under a non-zero variable static pitch, compared to the zero degree case.

Having all this in mind, it is apparent that, although the turbine experiences power losses for all wind speeds between the cut-in wind speed of 3 m/s and 10.5 m/s, the effect of the static floater pitch angle is more severe for static floater pitch angles higher or equal to 2° . Thereby, the static floater pitch angle of 2° signifies a floater pitch threshold, after which the turbine power is reduced by a percentage higher or equal to 1.5%, due to a considerable wind speed reduction (higher than 0.5%). On the same time, for static floater pitch angles lower than 2° , although the turbine power is reduced, the reduction can be treated as negligible. The turbine power reduction is more profound in the near rated wind speeds, due to the higher force loading experienced by the turbine, which leads to higher floater pitch angles.

It should be noted that, although the simulations were conducted using the BF turbine controller, the same results are observed when the FOWT controller is considered in the simulations. However, in this case, a pure power reduction due to static floater pitch is observed up to 9 m/s, whereas, in the region 10-11 m/s, the power generation difference occurs due to the combined effect of the static floater pitch angle and of the peak shaver schedule. In addition, the simulations highlighted that in the case of the statically pitched turbine with the FOWT controller, the wind speed reduction due to the static floater pitch angle and the peak shaver result in the inability of the generator torque controller to saturate at rated torque before 12 m/s. As a result, when the FOWT controller is used, the power deficit due to static pitch occurs up to 12 m/s and not up to 10.5 m/s, as mentioned in the previous analysis because the turbine is unable to achieve rated power before 12 m/s.

4.2.2 Constant Static Floater Pitch Angle Simulations

The simulation results presented in Subsection 4.2.1, although they give a good overview of the dynamics which cause a decrease of the BF and FOWT produced power at the whole partial load region, they do not clearly depict the effect of the magnitude of the static floater pitch angle on the power production of the FOWT. This is mainly a result of the variable static floater pitch angle schedule, according to wind speed, which constitutes a barrier into reaching clear conclusions. Therefore, it is opted to use a constant static floater pitch angle, ranging from 0° to 10° with a step of 2° for the whole range of examined wind speeds. As far as the wind speed range is concerned, in order to reduce computational effort, wind speeds between **6 and 11 m/s** will be considered in this simulation setup. This is due to the fact that, as shown in Subsection 4.2.1, the power deficit below 6 m/s is negligible, whereas after 11 m/s, the studied turbine, using the BF controller achieves rated power. Finally, the simulation setup regarding the DoFs and modules of OpenFAST, is be the same as with the variable floater pitch simulations.

The power curves of the BF turbine under a fixed static pitch between 0° and 10° and for wind speeds 6 m/s to 11 m/s are depicted in Figure 4.6. It can be clearly seen that, for wind speeds between 6 m/s and 11 m/s, as the constant static floater pitch angle increases, the BF generated power reduces. This is mainly caused by the reduction of the inflow wind speed, as the floater pitch angle increases, as explained by Equation 4.2.1. In addition, the decrease in power has a disproportional relationship with the static floater pitch angle due to the non linear nature of the cosine function and the non linear relationship of the turbine power with the wind speed. More specifically, Figure 4.7a shows that for a static floater pitch angle of 2° , the maximum power deficit of the statically pitched turbine compared to a non-pitched one is approximately 1.3% at 10.5 m/s. However, when the static floater pitch has a value of 10° , the power reduction is nearly 9.8% at 10.5 m/s.

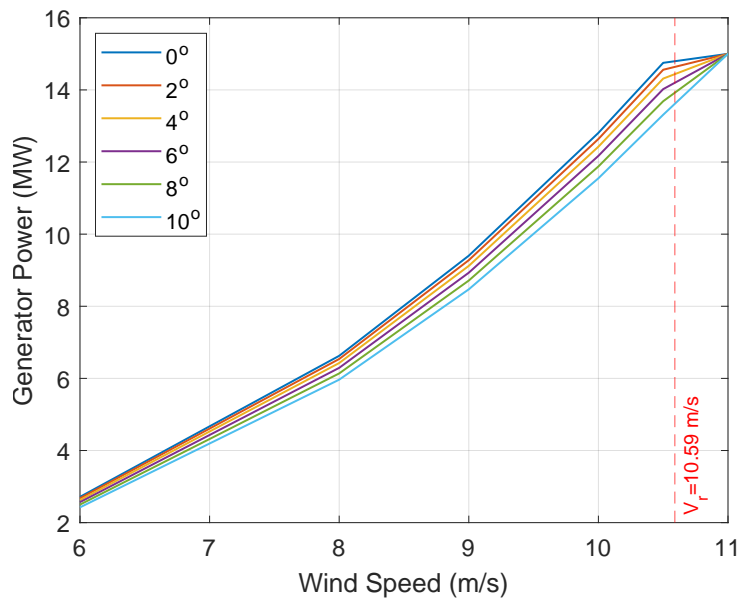


Figure 4.6: Comparison of the power curves of the IEA 15 MW RWT under BF configuration for wind speeds 6 to 12 m/s under a constant floater pitch angle, ranging from 0° to 10° .

Furthermore, it is useful to compare the percentage reduction in power of the turbine with the percentage reduction in the wind speed. These quantities are presented in Figures 4.7a and 4.7b respectively. According to Figure 4.7a, although for static floater pitch angles up to 4° , the power reduction is linear between 6 m/s and 10.5 m/s, this is not true for higher static floater pitch angles, starting from 6° . This is likely caused by the large wind speed reduction owing to

floater pitch angles being higher than 6° , which may have an impact on the non-linear controller region 1.5. Nevertheless, from 8 m/s to 10.5 m/s, where the controller tracks the optimal C_p value, the power deficit of the turbine is linear for all static floater pitch angles examined. On the same time, due to static floater pitch being constant for all wind speeds, the wind speed reduction percentage is constant for the different static floater pitch angles considered.

From Figures 4.7a and 4.7b, it can be deduced that, although the decrease of the turbine power follows the decrease of the wind speed, the percent power reduction is more or less higher than the percent wind speed reduction by a factor nearly equal to 2.8 for all wind speeds and static floater pitch angles examined. This non-linear effect can be attributed to the non-linear relation of the generated power with wind speed. Finally, the aforementioned findings are true for the FOWT as well, with the only exception being the wind speed region 10-11 m/s, where, since the peak shaver is mostly affecting the power, the aforementioned observations are true, but not so profound, as presented in Figure 4.8.

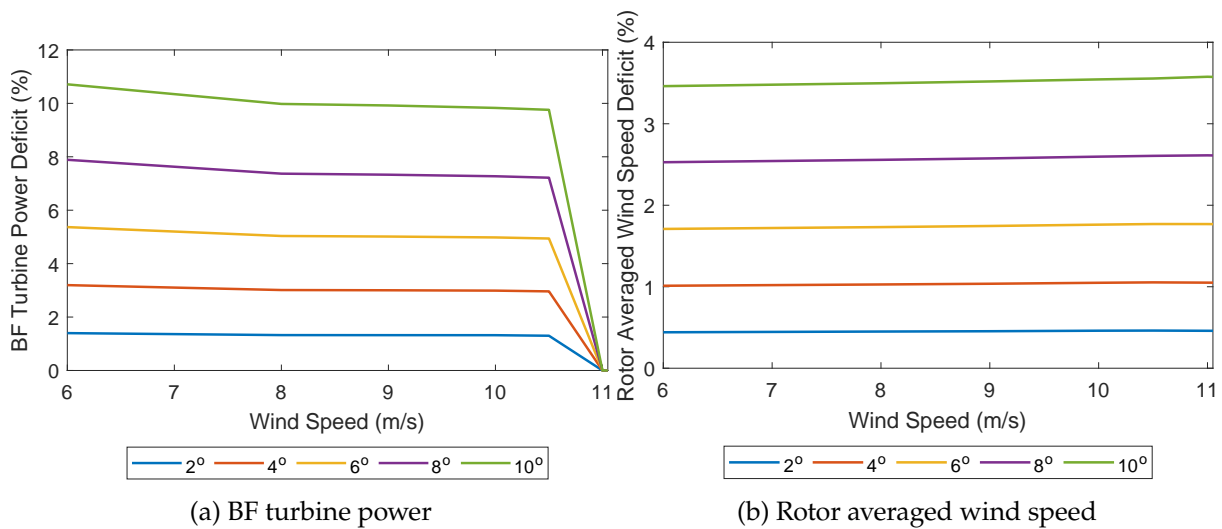


Figure 4.7: Percent difference of the generated power and the of the rotor averaged wind speed of the BF turbine under a fixed static floater pitch angle for all wind speeds, compared to the zero° case. Blue curve: 2° . Orange curve: 4° . Yellow curve: 6° , Purple curve: 8° . Green curve: 10° .

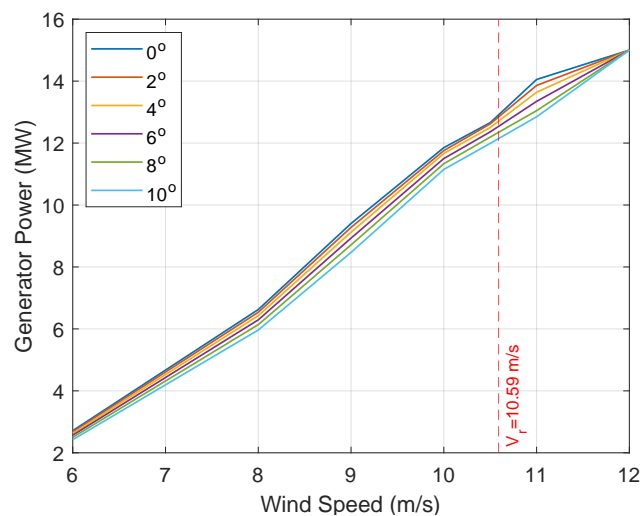


Figure 4.8: Comparison of the power curves of the IEA 15 MW RWT under FOWT configuration for wind speeds 6 to 12 m/s under a constant static floater pitch angle, ranging from 0° to 10° .

4.3 Effect of the In Situ Hydrogen Production Plant on the FOWT Performance

After the modification of the OpenFAST FOWT model according to the methodology presented in Section 3.5, the performance of the original and the augmented FOWT should be compared. In this direction, a steady wind profile is used in order to ensure simulation simplicity and more straightforward results. Also, for both configurations, the platform 6 DoFs and HydroDyn were enabled, in order to understand the floater dynamic behavior on the FOWT performance. In addition, it should be noted that, the inputs produced by WAMIT for the hydrodynamic loading of the floater are kept the same for the augmented FOWT, even though they should be re-generated for it. Yet, this process is outside of the scope of this project. Also, it is anticipated that due to the variation of the FOWT displaced water volume and new CoG by less than 2%, the original WAMIT files are sufficient for drawing valid results on the effect of the incorporation of the hydrogen plant on the FOWT. The comparison of the power curves and of the static floater pitch between the augmented and the original FOWT are depicted in Figures 4.9 and 4.10 respectively.

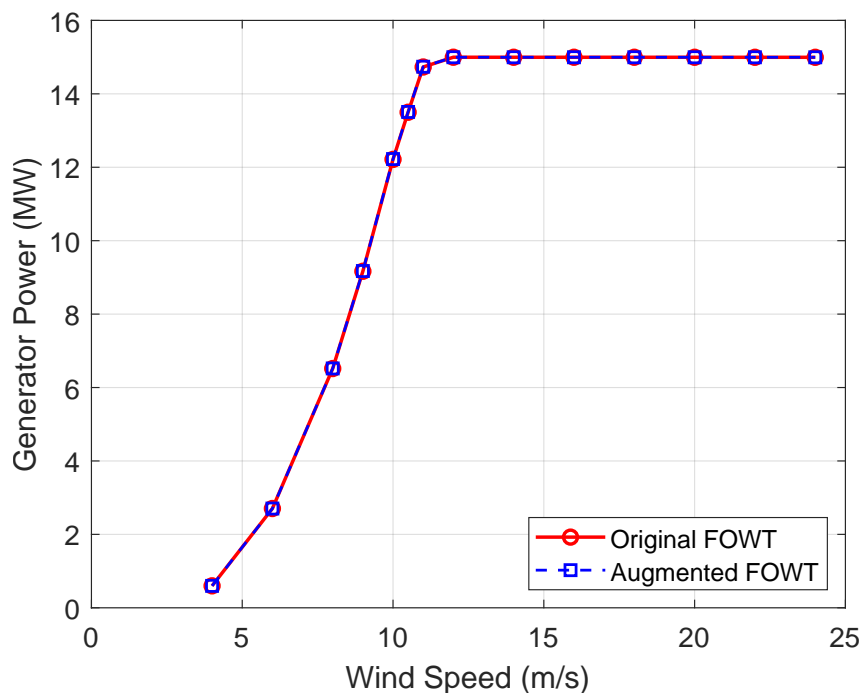


Figure 4.9: Comparison of the power curves of the original of the augmented FOWT, which incorporates the in situ hydrogen production plant. Red solid curve: Original FOWT design. Blue dashed curve: Augmented FOWT design.

As it can be seen in Figure 4.9, the alteration of mass, CoG and inertias of the FOWT due to the addition of the hydrogen production components, has virtually no effect on the power production of the turbine. This can also be validated by the examination of the FOWT static floater pitch variation. Also, Figure 4.10 shows that the static floater pitch of the augmented FOWT is slightly smaller when compared to the one of the original FOWT. This can be attributed to the fact that the floater CoG becomes more negative, whereas the floater centre of buoyancy (CoB) remains the same, because it is an indirect input in the WAMIT-generated input files. Therefore, it can be deduced that the hydrogen plant effect tends to be beneficial for the FOWT performance, due to its ability of restricting the floater pitch motion to some extent. However, due to the negligible effect on the power production, it can be concluded that the FOWT performance is likely to be unaffected by the added mass of the hydrogen plant and the

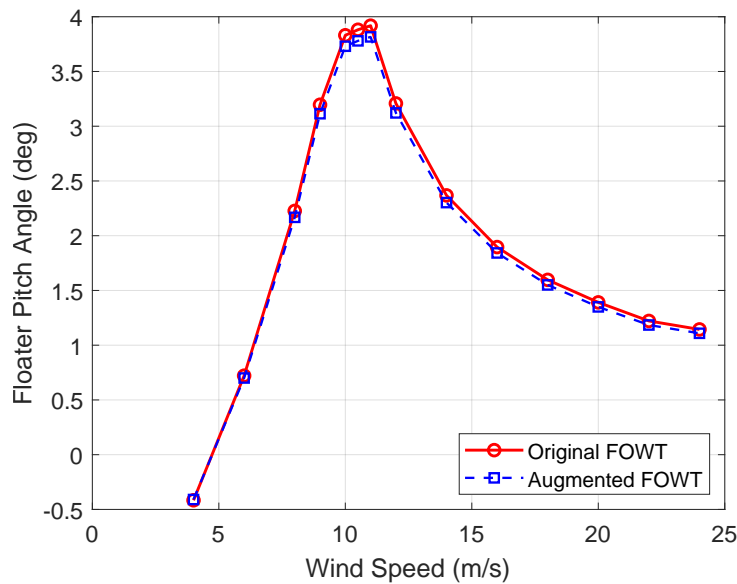


Figure 4.10: Comparison of the static floater pitch angle of the original FOWT and the augmented FOWT, which incorporates the in situ hydrogen production plant. Red solid curve: Original FOWT design. Blue dashed curve: Augmented FOWT design.

resulting changes in the floater design parameters. Thus, the comparison of the FOWT for in situ hydrogen production against the BF turbine and the evaluation of a FOWT aerodynamic redesign will be done without considering the hydrogen components' added mass, because they are deemed to have negligible effect on the results.

It should be noted that the positive effect of the in-situ hydrogen production on the performance of the FOWT is observed according to the assumption that all hydrogen components are rectangular prisms, situated inside the turbine tower, with their CoG is on the z-axis. Yet, in reality, the components' geometries are likely to be more complex and their CoG may have an offset in respect to z-axis. In this case, the floater ballast may need to be reconfigured in terms of its mass and its positioning, with the view of guaranteeing that the CoG of the augmented FOWT is on the z-axis and aligned with the floater CoB. Hence, the total FOWT mass, displaced water volume, CoG and inertias are expected to deviate from their values calculated in this project.

Moreover, an change of the displaced water volume and of the mass distribution on the floater, coupled with components positioned not close to z-axis may lead to a different response of the floater to hydrodynamic excitations, which require the calculation of new WAMIT outputs for the various augmented floater designs. Yet, the alteration of the dynamic characteristics of the FOWT when subjected to wave loading, leads to the conclusion that it may be difficult to predict a priori whether the FOWT will be positively or negatively affected by the in situ hydrogen plant. For this reason, each in-situ hydrogen production FOWT geometry should be thoroughly analysed via simulations to provide quantitative and qualitative arguments on the effect of the hydrogen components on the FOWT performance.

4.4 Turbulent Wind Simulations

Since real inflow wind fields are turbulent, the FOWT and the BF turbines should be simulated under turbulence. In this way, the effect of a time-varying wind field on the performance on the turbines will be examined and the obtained results will be closer to reality. Thus, clear recommendations will be provided on specific aerodynamic parameters of the FOWT that may

need to be redesigned in order to create performance gains. This section is structured as follows. Firstly, in Subsection 4.4.1 the FOWT performance will be evaluated under a variety of turbulence intensity (TI) values, so as to highlight the effect of TI in the FOWT generated power. Then, Subsection 4.4.2 will discuss the comparison of the FOWT and the BF turbine under turbulent wind conditions with the view of assessing the performance of the FOWT and the possibility of an aerodynamic redesign for performance improvement.

4.4.1 Effect of the Turbulence Intensity on the FOWT Performance

Although as pointed in Section 3.3, the TI of the simulated US East Coast site is 10%, it is worth examining the effect of different TI values on the performance of the FOWT. This originates from the fact that the TI values experienced by a wind turbine are time-varying and wind speed-dependent [66]. In this direction, in order to understand how TI impacts on the FOWT power and behavior, simulations were conducted under constant TI values ranging from 5% to 20% with a step of 5% for the whole range of wind speeds between 4 and 14 m/s. The distribution of simulated wind speeds was the same as in steady wind.

The power curves of the FOWT according to the simulated TI values are shown in Figure 4.11. It should be noted that since the FOWT power showed a negligible variation for an average wind speed of 4 m/s, while after 14 m/s, all simulation setups achieved rated power, only wind speeds between 6 and 14 m/s are examined. An observation of Figure 4.11 leads to the conclusion that TI impacts mainly in the FOWT partial load region by increasing the FOWT power for average wind speeds between 6 and 9 m/s, while contributing to power losses from 10 m/s to 12 m/s. More specifically, for the region 6 to 9 m/s, since the FOWT power (P_{FOWT}) is dependent on the wind speed by a power of 3 as per Equation 4.4.1. Hence, an increase of the wind speed in comparison to its mean value, results in a power gain, which outweighs the power loss occurring from a wind speed decrease, in respect to the mean.

$$P_{FOWT} = \eta_{tot} C_p \frac{1}{2} \rho A U^3 \quad (4.4.1)$$

Yet, this justification is valid in case the airfoils do not stall under turbulence. So, the mean AoA and its standard and 2x standard deviation values for wind speeds 6 and 9 m/s and for the TI bounds of 5% and 20% of this project should be examined. According to Figures 4.12a to 4.12d, the mean, standard deviation and 2x standard deviation of the AoA along the airfoils for TI 5% and TI 20% are well outside the stall region, with the exception of the blade part up to $r/R=0.2$. However, since inboard blade parts generally contribute less to torque and thrust generation and, consequently to FOWT power, it can be deduced that, even at TI=20%, where the largest spanwise AoA variations in respect to their mean value are observed, the airfoils generally operate well outside of the stall region. Hence, due to the previously analysed mechanisms, the wind speed variation due to turbulence creates power gains between 6 to 9 m/s, which increase as TI increases towards 20%.

Furthermore, Figure 4.11 depicts that, from 10 to 12 m/s, TI has a detrimental effect on the power produced by the FOWT in comparison to the steady wind case, which becomes more severe as TI increases to 20%. The reasoning behind those observations lies on the way ROSCO controller operates. More specifically, since the wind speed estimator block of ROSCO controller operates in discrete time and not in continuous time [78], it cannot track the instantaneous variations of the wind speed under turbulent conditions. This phenomenon is depicted in Figures 4.13a to 4.13b for an average wind speed of 11 m/s and for all TI values examined in this project. It

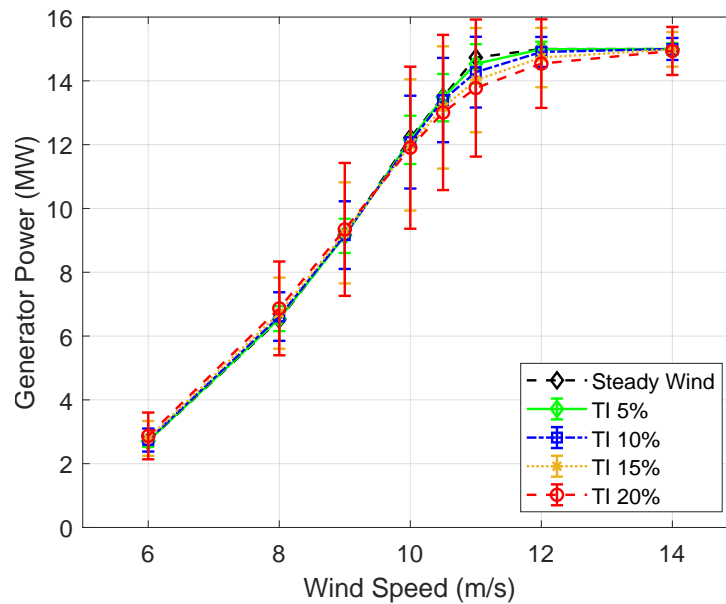


Figure 4.11: Comparison of the power curves of the IEA 15 MW FOWT on the UMaine semi-submersible floater for turbulence intensity values 5% to 20% with a step of 5% and for wind speeds 6-14 m/s. Black dashed curve: Steady wind. Green solid curve: TI=5%. Blue dashdotted curve: TI=10%. Yellow dotted curve: TI=15%. Red dashed curve: TI=20%.

should be noted that the aforementioned wind speed was randomly chosen and same results were observed for other wind speeds between 10 m/s and 12 m/s.

From Figures 4.13a and 4.13b, it is evident that at various time intervals of the simulations, the wind speed estimate is higher than the actual wind speed experienced by the rotor. Since the peak shaver routine relies on the wind speed estimate to saturate the blade pitch angle according to a specified schedule, under turbulence, the blade pitch angle set by the controller tends to be higher than its required value for a time-specific wind speed. As a result, as depicted in Figure 4.14a, under turbulence, there is higher blade pitching between 10 and 12 m/s, compared to steady conditions. In addition, Figures 4.13a and 4.13b show that increasing TI values lead to higher wind speed fluctuations in respect to the mean value. Therefore, as it can be seen in Figure 4.14a as TI increases, the value of the blade pitch angle set by the controller between 10 and 12 m/s increases as well, whereas the maximum blade pitching occurs for TI=20%.

As a result, due to both reasons that were explained in the previous paragraph, the larger blade pitch angles set by the controller, negatively impact the FOWT power generation by contributing to power shedding as early as 10 m/s. In fact, for an average wind speed of 11 m/s and for TI=20%, the high blade pitch angles set by the controller contribute to a maximum 6.5% power loss in respect to steady conditions. From 12 m/s onwards, positive wind speed fluctuations in respect to the mean value result in saturation of the generator torque controller to rated torque and thus achievement of rated power, whereas the negative ones are responsible for enabling the peak shaver. For this reason, as described in Figure 4.11, the effect of TI becomes less significant for small TI values (i.e 5% and 10%) and only higher TI values result in power generation losses. Finally, for wind speeds higher than 14 m/s, at all TI values, the FOWT operates at rated power, thereby no losses are observed.

Regarding the FOWT average floater pitch angle variation according to wind speed for the TI values examined, Figure 4.14b depicts that they are nearly the same for all TI values up to 8 m/s. From 9 m/s to 14 m/s, the FOWT average floater pitch angle decreases for higher TI values.

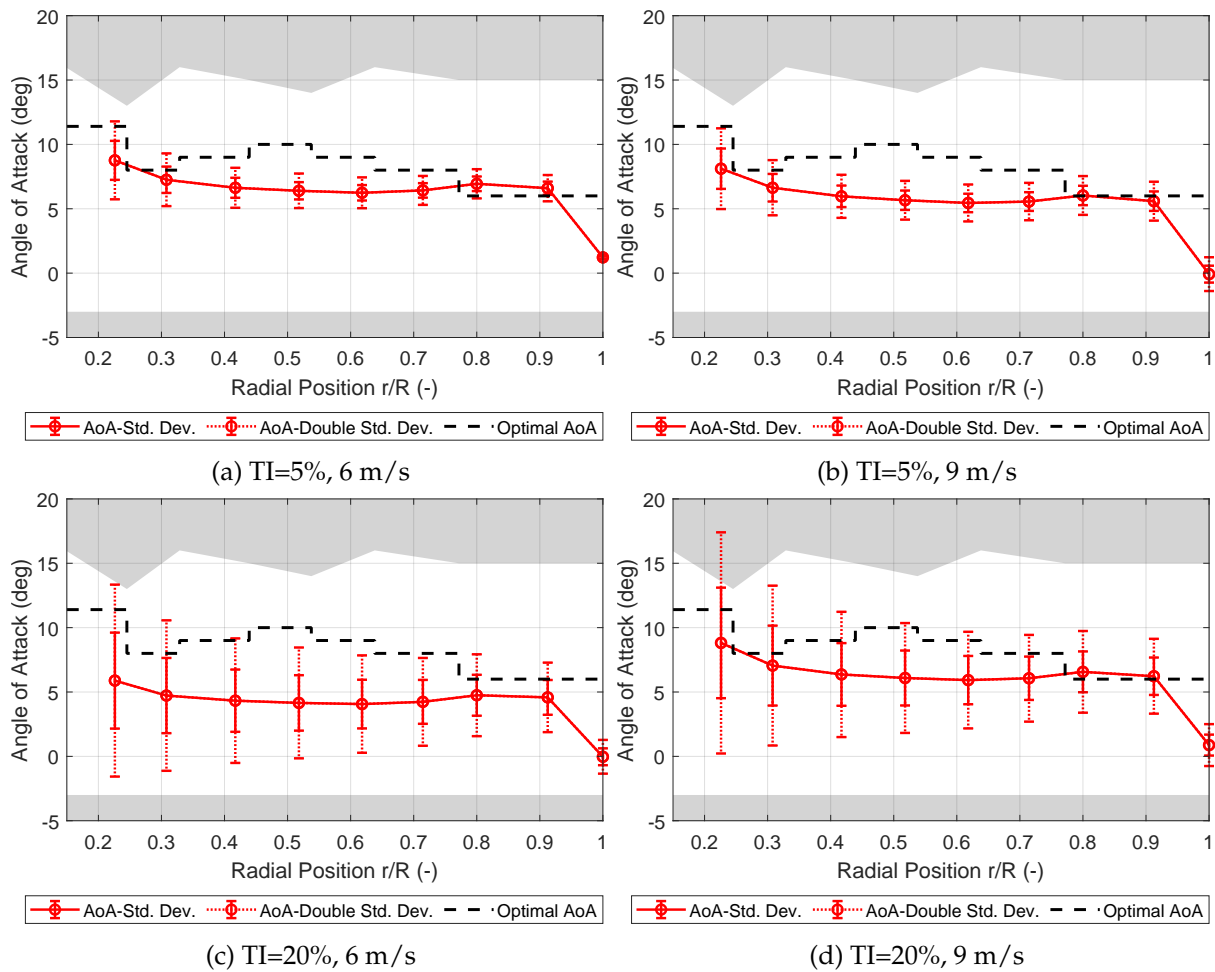


Figure 4.12: Spanwise angle of attack variation of the IEA 15 MW FOWT for TI values 5% and 20% and for wind speeds 6 m/s and 9 m/s. Solid red error bars: AoA standard deviation. Dotted red errorbars: AoA 2x standard deviation. Black dashed line: Optimal AoA. Grey area: Stall region for the different airfoils.

The decrease is more prevalent in the near rated region (9-12 m/s). It should be noted that the maximum decrease of the FOWT average floater pitch angle under turbulent conditions, compared to steady ones, is 14% and it is observed for TI=20% at an average wind speed of 11 m/s. The trends observed in Figure 4.14b are explained by the examination of the average blade pitch angles observed for the examined TI values.

Between 6 and 8 m/s, the blade pitch is the same for all TI values, thus the FOWT is expected to operate at nearly the same loading conditions for steady conditions and for all TI values between 5% and 20%. However, from 9 m/s to 12 m/s, the reduction of the average floater pitch angles for higher TI values is caused by the larger blade pitch angles observed in the simulations, owing to the larger wind speed estimates. Hence, the larger blade pitching action for higher TI values is likely to contribute in reducing the loading on the FOWT, which results in limiting the floater pitch angle for wind speeds 9 to 12 m/s.

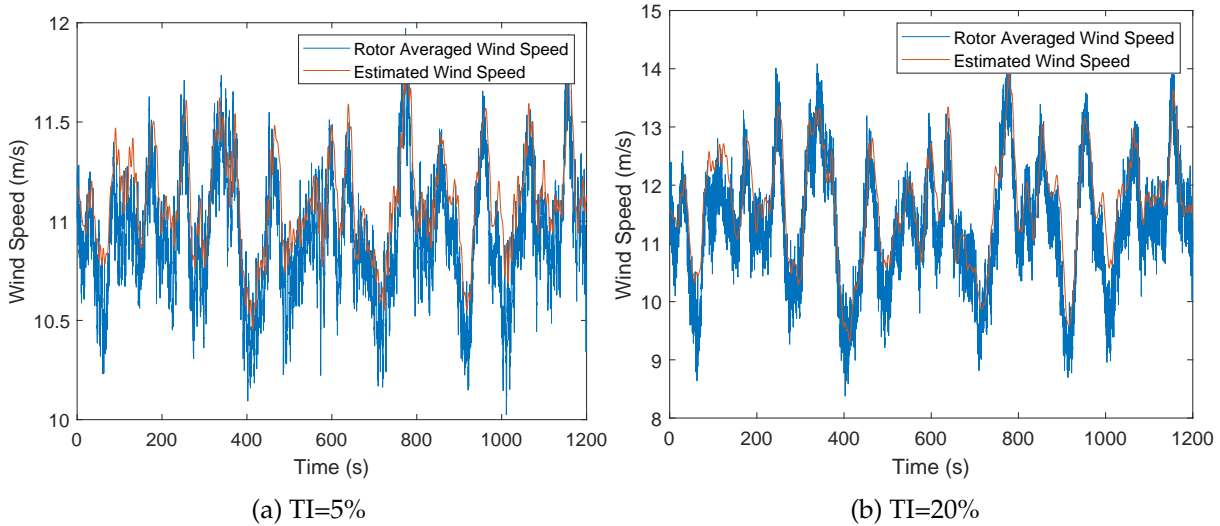


Figure 4.13: Comparison of the time series of the rotor averaged wind speed and of the wind speed estimate of the ROSCO controller for an average wind speed of 11 m/s and for TI values 5% to 20%. Blue curves: Rotor averaged wind speed. Orange curves: Wind speed estimate.

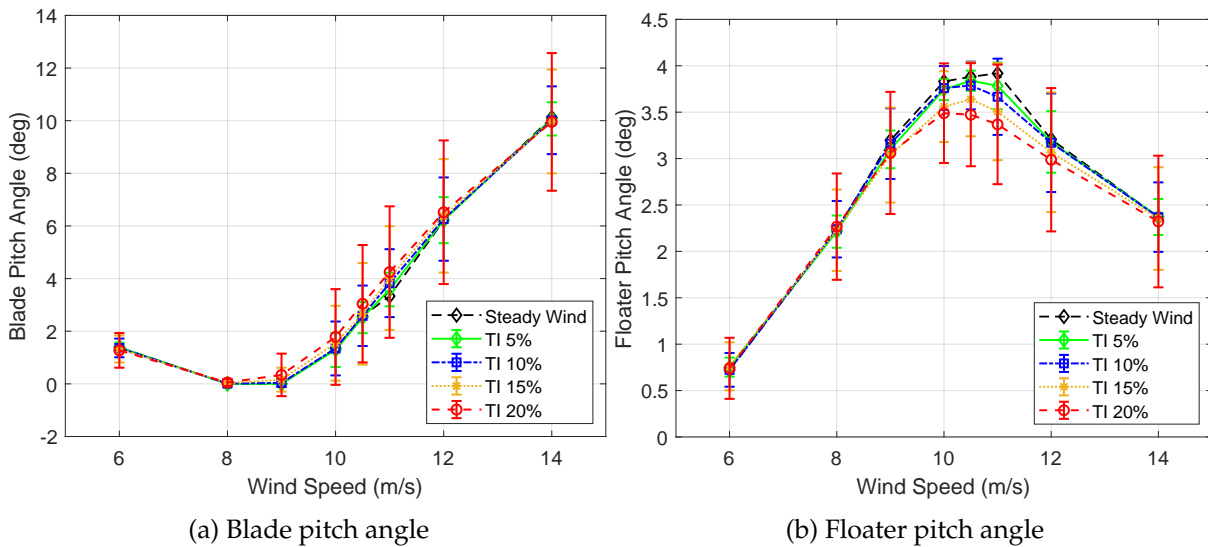


Figure 4.14: Comparison of the average blade pitch and of the average floater pitch angles of the IEA 15 MW FOWT on the UMaine semi-submersible floater for turbulence intensity values 5% to 20% with a step of 5% and for wind speeds 6-14 m/s. Black dashed curve: Steady wind. Green solid curve: TI=5%. Blue dashdotted curve: TI=10%. Yellow dotted curve: TI=15%. Red dashed curve: TI=20%.

4.4.2 Comparison of the FOWT and BF Performance-Turbulent Conditions

One of the most important aspects, which should be examined in this project is how the performance of a FOWT is differentiated compared to a BF turbine when both are subjected to turbulence. As already discussed, turbulence is able to provide more realistic indications on the motive forces, which drive the aforementioned turbines' power generation characteristics. The comparison of the IEA 15 MW RWT FOWT and BF turbine under turbulence is done at a TI value of 10%, because, as stated at Section 3.3, it is the characteristic TI value for the examined US East Coast site.

The FOWT and the BF power curves under for a TI value of 10% are presented in Figure 4.15a, whereas Figure 4.15b depicts the percent power reduction of the FOWT in respect to the BF turbine. It should be noted that, under turbulence, the wind speeds used in the analysis range from 4 m/s to 16 m/s because, for $U > 16$ m/s, both configurations achieve rated power. Nevertheless, to provide clear explanations on the way the performance of the FOWT varies in respect to that of the BF turbine, the average TSR (Figure 4.16a), the average rotational speed (Figure 4.16b), the average blade pitch angle (Figure 4.17a) of the FOWT and of the BF turbine, as well as the average FOWT floater pitch angle (Figure 4.17b) should be examined as well.

To begin with, between 4 and 6 m/s, the simulations showed that the FOWT and the BF turbine power figures are nearly the same, with their relative difference being lower than 1%. This stems from the fact that, not only both turbines operate at the same minimum rotational speed constraint (5 RPM), but also the average floater pitch angle is lower than 2° , which, as deduced in Section 4.2, does not cause significant wind speed reduction and hence power difference. In addition, Figures 4.16a and 4.17a show that, up to 6 m/s, the FOWT and BF controller actions in terms of tracked TSR setpoints and blade pitch angle saturation are the same. It is worth noticing that the observed small power difference of the FOWT and the BF turbine between 4 m/s to 6 m/s may also be an outcome of the FOWT controller tower top parallel compensation loop, which limits the FOWT pitching, as it is deduced by the small values of the floater pitch angle in Figure 4.17b.

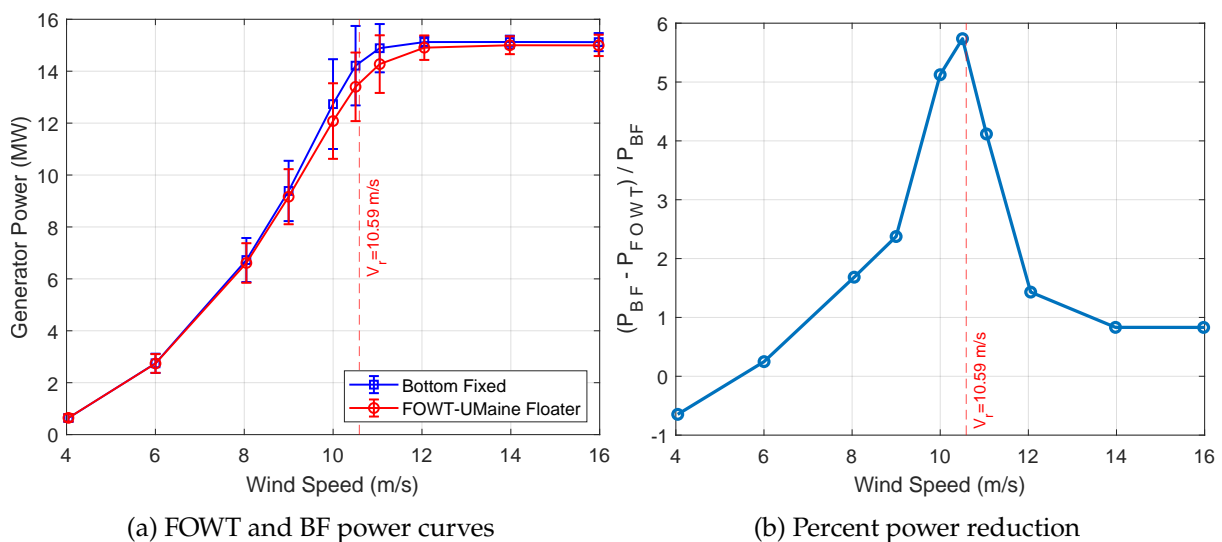


Figure 4.15: Comparison of the power curves and of the percent power reduction of the IEA 15 MW reference wind turbine under FOWT and BF configurations and under turbulent wind conditions with TI=10%. Red curve: FOWT. Blue curve: BF turbine.

Then, for wind speeds 7 to 9 m/s, the FOWT starts losing power in respect to the BF turbine, with the maximum FOWT power deficit being nearly 2.4% at 9 m/s. The main driver of the reduction of the FOWT power in respect to that of the BF turbine in this region is the reduced inflow wind speeds (shown in Figure 4.18), resulting from the average floater pitch angle being higher than 2° . It should be noted that the maximum power reduction of the FOWT is observed for an average floater pitch angle of nearly 3.2° . One additional side effect of the inflow wind speed reduction due to the average floater pitch angle is the variation of the TSR set by the FOWT controller between 7 and 9 m/s.

More specifically, although both the FOWT and the BF controllers follow the same optimal TSR and blade pitch angle setpoints (9 and 0° respectively), the reduction of the inflow wind speeds in the case of the FOWT results in its controller eventually tracking a TSR of nearly 9.2, which

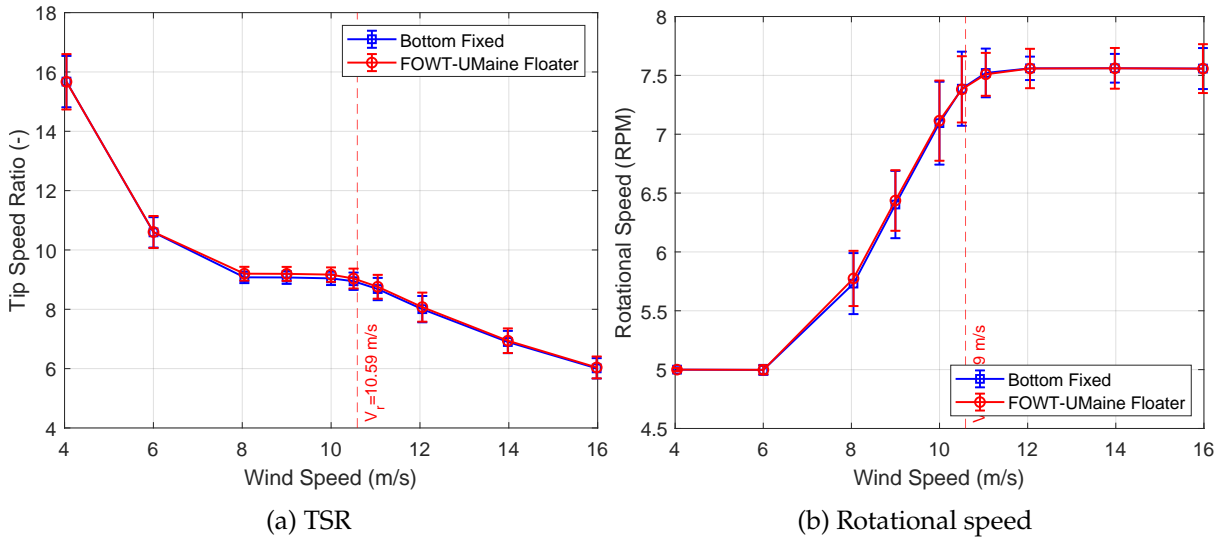


Figure 4.16: Average tip speed ratio and rotational speed as a function of the wind speed for the IEA 15 MW reference wind turbine under FOWT and BF configurations and under turbulent wind conditions with $TI=10\%$. Red curve: FOWT. Blue curve: BF turbine.

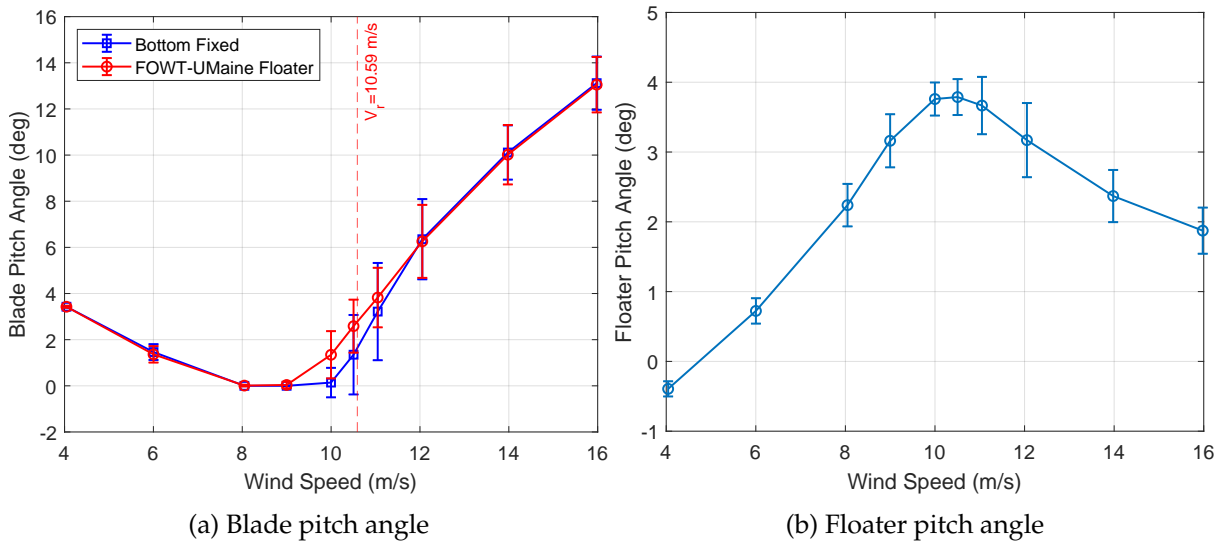


Figure 4.17: Average blade pitch and floater pitch angles as a function of the wind speed for the IEA 15 MW reference wind turbine under FOWT and BF configurations and under turbulent wind conditions with $TI=10\%$. Red curve: FOWT. Blue curve: BF turbine.

is higher than that of the BF turbine (9). This trend is clearly depicted in Figure 4.16a. Consequently, as shown in Figure 4.16b, the higher TSR imposed by the FOWT controller leads to higher rotational speed values for the FOWT, compared to the ones of the BF in between 7 and 9 m/s.

However, from 10 m/s to 12 m/s, the FOWT experiences considerable power losses in respect to the BF turbine, which are maximised at 5.7% for a wind speed of 10.5 m/s. In this wind speed region, large average FOWT floater pitch angles are observed, which surpass 3° , while between 10 to 11 m/s, the floater pitch angles are very close to their maximum average value of 3.8° , obtained at 10.5 m/s. However, from 10 to 12 m/s, in addition to the floater pitch angle, the FOWT loses power due to the peak shaver schedule. As shown in Figure 4.17a at 10 m/s and 10.5 m/s, the average blade pitch angles of the FOWT are approximately 1.3° and 2.6° respectively whereas the BF turbine operates at the fine pitch angle of 0° . Even at 11 m/s and

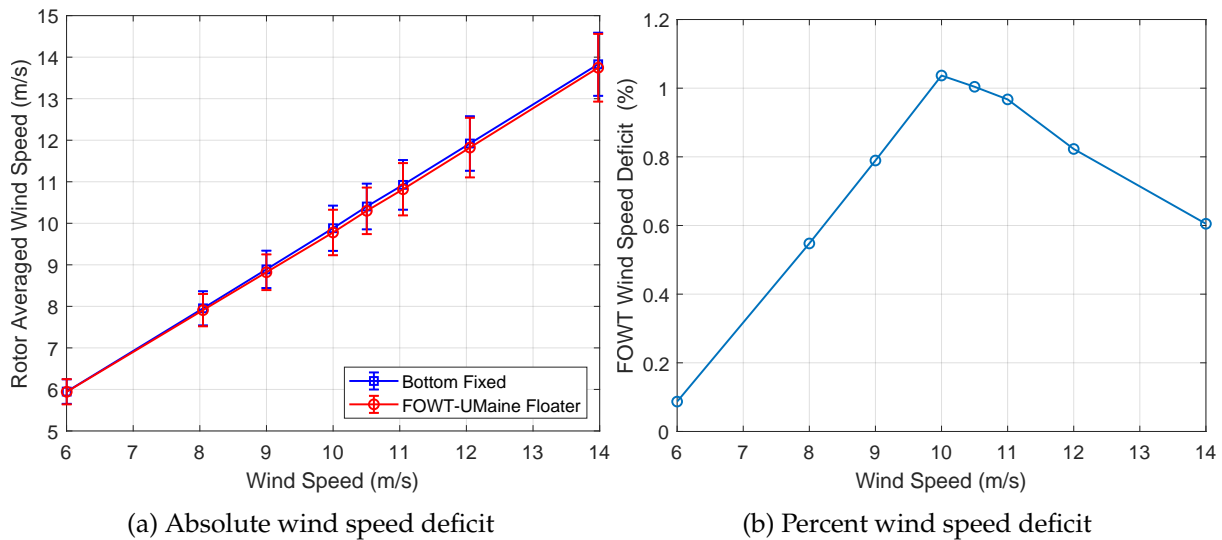


Figure 4.18: Absolute and relative wind speed deficit of the IEA 15 MW reference wind turbine under FOWT and BF configurations under turbulent wind conditions with $TI=10\%$. Red curve: FOWT. Blue curve: BF turbine.

12 m/s, where conventional blade pitch control is used in the BF turbine, the FOWT blade pitch angles set by the FOWT controller are higher than their BF counterparts because the FOWT operates under the blade pitch saturation schedule of the peak shaver.

As a result, between 10 and 12 m/s, the FOWT power loss in respect to the BF turbine is not only caused by the inflow wind speed reduction due to the static floater pitch angle, as proposed by Figure 4.18, but also from the peak shaving. Interestingly, as pointed by Figure 4.15a, although the BF turbine achieves rated power at 12 m/s, the FOWT power is lower than rated at 12 m/s. This observation is anticipated because, at 12 m/s, due to the combined effect of the static floater pitch angle and of the peak shaver, the FOWT torque is expected to be lower than its rated value, which hinders the achievement of rated power. In addition, Figure 4.16b suggests that between 10 and 12 m/s, the FOWT rotational speed is nearly the same as its BF counterpart. This likely occurs from the FOWT power shedding due to the peak shaver, which lowers the rotational speed setpoints tracked by the FOWT generator torque controller.

Finally, from 14 m/s onwards, as per Figure 4.15a, both the FOWT and the BF turbine operate at rated power. This is also pointed by Figures 4.16b and 4.17a, which show that the average rotational speed of both turbines is nearly 7.56 RPM, while they follow approximately the same blade pitch schedule. Although the floater pitch angle is higher than 2° , which causes an inflow wind speed reduction, the FOWT achieves rated power because torque is saturated at its rated value. Nevertheless, it is interesting to note that, as depicted on Figure 4.15b, the rated power of the FOWT is nearly 1% lower than that of the BF turbine. This is likely associated with the different way the FOWT and the BF controllers operate at rated power, which result on average FOWT power lower than 15 MW.

To elaborate on this, for wind speeds above rated, the FOWT operates under a constant torque setting, whereas the BF turbine at a constant power setting. Thus, the rotational speed fluctuations due to the unsteady wind field may be only reflected in the power only under the constant torque operation, i.e for the case of the FOWT. Indeed, the examination of Figures 4.15a and 4.16b, shows that although a deviation of the rotational speed in respect to the mean exists in both the FOWT and the BF, only the FOWT power fluctuates around its mean value. Thereby, on average, the FOWT power may be lower than the BF one (15 MW).

Yet, in order to understand the reasons for the FOWT performance deficit compared to the BF turbine, indices like the inflow angle, the angle of attack (AoA) and the aerodynamic torque and thrust per unit length variations along the blade span, should be examined. Their comparison will be done for the wind speeds of 9 and 10.5 m/s, since they are representative of the pre-peak shaver and peak shaver regions respectively. Also, they signify the wind speeds with the largest FOWT power reduction compared to the BF turbine, thereby rendering the comparison easier to do. Nevertheless, the definitions of the aforementioned parameters should be presented. The inflow angle and the AoA are defined according to Equations 4.4.2a and 4.4.2b.

$$\tan \varphi = \frac{U(1 - a)}{\Omega r (1 + a')} \quad (4.4.2a)$$

$$\alpha = \varphi - \theta_{twist} - \theta_{pitch} \quad (4.4.2b)$$

where φ is the inflow angle, U the inflow wind speed, a the axial induction factor, Ω the rotor rotational speed, r the radial position of the blade element, a' the tangential induction factor, α the AoA, θ_{twist} the local blade twist angle and θ_{pitch} the collective blade pitch angle respectively. It should be noted that, as it was observed during the simulations, the axial and the tangential induction factors do not vary significantly over the blade span for a specific wind speed. In addition, although the power produced by the turbine is mainly determined by the per unit aerodynamic torque, the definition of the per unit aerodynamic thrust should be presented due to being crucial in determining the out-of plane forces and moments, and, consequently, the floater pitch angle. The distribution of the torque (dQ) and thrust (dF_N) forces over the blades of a wind turbine are given by Equations 4.4.3a and 4.4.3b [60].

$$dQ = \frac{Bc}{2} \rho \frac{U^2(1 - a)^2}{\sin^2 \varphi} (C_L \sin \varphi - C_D \cos \varphi) r dr \quad (4.4.3a)$$

$$dF_N = \frac{Bc}{2} \rho \frac{U^2(1 - a)^2}{\sin^2 \varphi} (C_L \cos \varphi + C_D \sin \varphi) dr \quad (4.4.3b)$$

$$U_{rel} = \frac{U(1 - a)}{\sin \varphi} \quad (4.4.3c)$$

where B is the number of blades (3) and c is the local airfoil chord length, while the other variables have been explained in the previous sections. The term $U^2(1 - a)^2/\sin^2 \varphi$ corresponds to the square of the relative wind speed seen by the blade nodes, which is defined by Equation 4.4.3c. The torque and thrust variations are also associated with the AoA due to its role in determining the spanwise C_L/C_D values.

Firstly, the spanwise inflow angle distributions over the span should be examined for 9 m/s and 10.5 m/s. As depicted in Figure 4.19a, for wind speeds up to 9 m/s, due to the reduction of the inflow wind speed owing to the static floater pitch being higher than 2° and due to the increase of the rotational speed of the rotor, the inflow angle, by its definition, slightly decreases compared to the BF one. In this wind speed range, the simulations showed that the axial and tangential induction factors remained nearly the same for the FOWT and the BF turbines. Thus, this inflow angle increase can be considered as negligible. On the contrary, at 10.5 m/s, Figure 4.19b shows that the spanwise inflow angle of the FOWT increases considerably in respect to

the BF one. This mainly results from the higher blade pitching imposed by the controller. Consequently, up to 9 m/s, the relative wind speed seen by the blade is reduced mainly due to the static floater pitch angle, whereas, in the peak shaver region, it is combined with an increase of the inflow angle, which further reduces the spanwise relative wind speed.

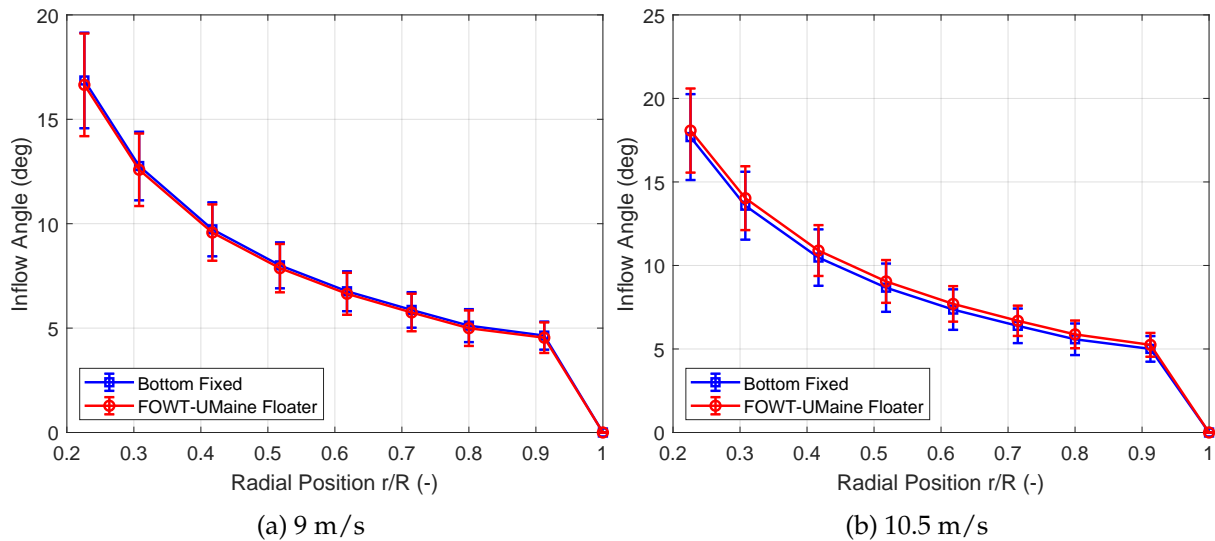


Figure 4.19: Spanwise inflow angle variation of the the IEA 15 MW RWT under FOWT and BF configurations, under turbulent wind conditions with $TI=10\%$ and for an average wind speeds of 9 and 10.5 m/s. Red curve: FOWT. Blue curve: BF turbine.

As far as the spanwise AoA variation is concerned, Figures 4.20a and 4.20b show that at both 9 m/s and 10.5 m/s, the AoA standard deviation is considerably away of the stall region. Even considering the 2x standard deviation it is always outside of the stall region. This points out that the IEA 15 MW FOWT and BF designs are well protected from performance loss due to stall. Furthermore, according to Figure 4.20a, the slight decrease in the inflow angle at 9 m/s is reflected in the AoA variation, by slightly decreasing the FOWT AoA compared to its BF counterpart. This is expected as the blade pitch angles of the two turbines are 0° at 9 m/s, while their blades have the same twist angle distributions. Therefore at 9 m/s, the decreased AoA drives the airfoils to slightly lower C_L/C_D value. Still, at 10.5 m/s, the increased blade pitching due to the peak shaver, results in decreasing the spanwise AoA by approximately 1° along the blade span. This is the maximum AoA reduction observed for wind speeds between 10-12 m/s.

The reduction in AoA has a detrimental effect on the airfoils' aerodynamic performance as it moves their operating point away from their optimal region. Thereby, their operational C_L/C_D value is reduced, which, as proposed by the definition of the spanwise torque (Eq.4.4.3a), has the effect of reducing the blade aerodynamic torque and consequently the turbine power. Therefore, a possible aerodynamic redesign could involve the increase of the FOWT spanwise AoA with the view of operating the airfoils nearer to their optimal region. In this way, their aerodynamic efficiency can be increased, thus boosting the torque force produced by the blades.

Finally, having examined the variations of the inflow angle and the AoA, the FOWT and BF blade torque along the span should be analysed. As presented in Figure 4.21a, the spanwise torque of the FOWT at 9 m/s is always lower than that of the BF turbine by approximately 3%. Same results are obtained for other wind speeds below 9 m/s. However, the torque reduction is less severe for wind speeds below 9 m/s. The reduction in torque in the pre-peak shaver region stems mainly from the reduction of the inflow wind speed, due to increased static floater pitch angle, which is depicted in Figure 4.18. Although there is an effect on the inflow angle and the AoA, it tends to be overwhelmed by the wind speed deficit.

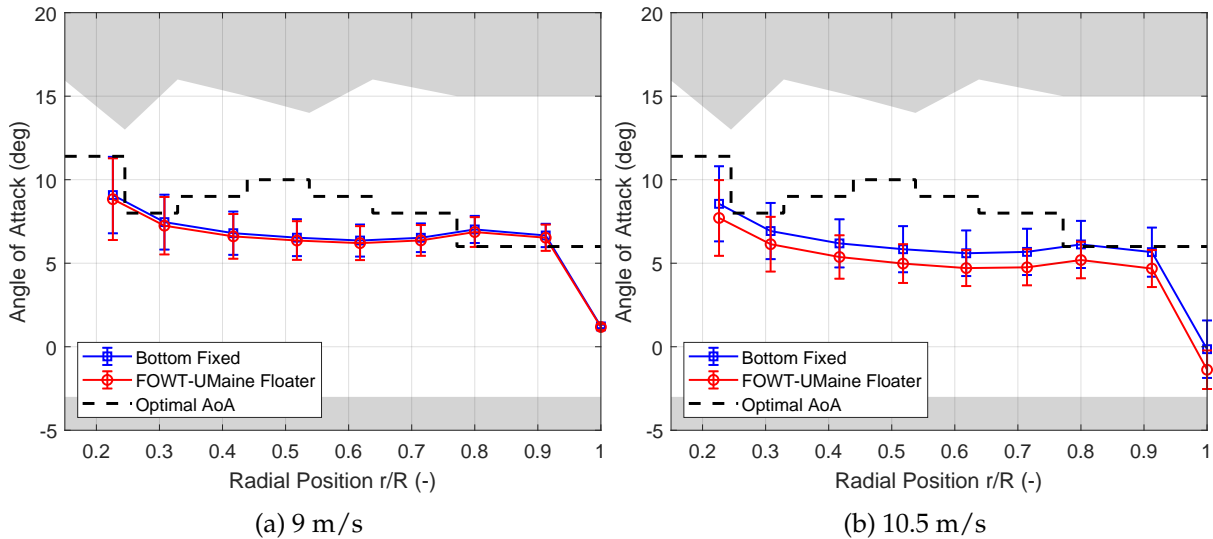


Figure 4.20: Spanwise angle of attack variation of the the IEA 15 MW RWT under FOWT and BF configurations, under turbulent wind conditions with $TI=10\%$ and for an average wind speeds of 9 and 10.5 m/s. Red curve: FOWT. Blue curve: BF turbine. Dashed black line: Optimal angle of attack. Grey area: Stall region.

At 10.5 m/s, Figure 4.21b, suggests that the FOWT spanwise torque is significantly reduced compared to the BF. This results from the combined effect of lower inflow wind speed (Figure 4.18), higher spanwise inflow angle (Figure 4.19b), and lower spanwise airfoil aerodynamic efficiency, originating from the reduction of the airfoils' AoA compared to their optimal values (Figure 4.20b). All parameters result in reducing the relative wind speed seen by the blades of the FOWT and also in reducing the airfoils' potential in generating torque, as per Equation 4.4.3a. It is interesting to note that at 10.5 m/s, the spanwise FOWT torque exhibits a maximum reduction of nearly 6% compared to the BF. Consequently, one interesting aerodynamic redesign idea is finding ways to regain the spanwise 6% torque deficit along the blade.

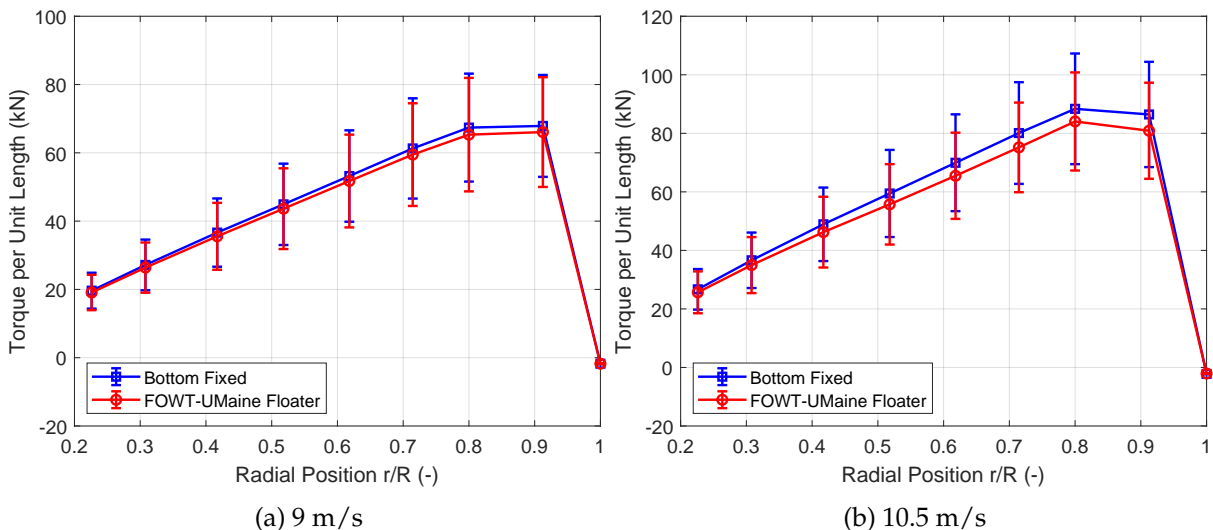


Figure 4.21: Spanwise torque per unit length variation of the the IEA 15 MW RWT under FOWT and BF configurations, under turbulent wind conditions with $TI=10\%$ and for an average wind speeds of 9 and 10.5 m/s. Red curve: FOWT. Blue curve: BF turbine.

5 | Aerodynamic Redesign

The results presented in Chapter 4 suggest that the IEA 15 MW FOWT inherently loses power due to static tilt, occurring from the average floater pitch angle during the simulations and the peak shaving routine. Therefore, the FOWT should be redesigned so as to improve its performance and to bring it as close as possible to its BF counterpart. Although there are plenty of ways for a FOWT to gain performance, an aerodynamic redesign of the IEA 15 MW FOWT should be pursued in this project as it is relatively simple and aligned with the results produced so far. This chapter has the following structure. Firstly, Section 5.1 delves into the methodology and considerations regarding the aerodynamic redesign solutions what will be implemented in this project. Then, Sections 5.2 and 5.3 present and compare possible redesign scenarios which involve the alteration of the spanwise blade twist angle and the spanwise chord length as a means of increasing the aerodynamic torque produced by the blades. Last but not least, Section 5.4 evaluates a two-element aerodynamic redesign via simultaneously altering both the spanwise blade twist angle and the spanwise chord length.

5.1 Aerodynamic Redesign Methodology

As shown by Chapter 4, the wind speed reduction due to the increased floater pitch angle and the decreased turbine loading owing to the peak shaver routine have the effect of reducing the power produced by the FOWT. However, the FOWT performance deterioration in respect to the BF turbine is associated with the variation of the in-plane force (torque) distribution on the blades of the FOWT and the BF. Therefore, the redesign process that will be conducted in this project, will try to provide solutions on how to increase the torque produced by the FOWT blades, so as to cover their deficit compared to their BF counterparts. Nevertheless, since the torque produced by blade nodes is closely associated with the out-of-plane force (thrust), which is the motive force behind the floater movement in the pitch DoF, attention should be given on the thrust distribution over the blades as well. Given the definitions of the torque and thrust force distributions of the blade nodes, as per Equations 4.4.3a and 4.4.3b, in order to increase the torque produced by the wind turbine blades, the following solutions can be implemented:

- Change of the chord length of the local airfoils.
- Change of the C_L/C_D values of the blades' airfoils, which will assure that the airfoils contribute to large lift force generation, while at the same time contributing to small drag. Thus, the airfoils' AoA should increase in case it is lower than their optimal AoA or operate as close to their optimal AoA value as possible.
- Change of the relative wind speed seen by the blade nodes, which can mainly be achieved via altering the values of the inflow angle φ , of the rotational speed Ω and of the induction factor a .

The simulation results presented in Subsection 4.4.2 suggest the maximum average inflow angle for all blade nodes was smaller than 18° . Due to the nature of the sine and cosine functions, at

such angles the $\cos \varphi$ value is close to 1, whereas the values of $\sin \varphi$ are lower than 0.3 in any case, while being more sensitive to the inflow angle variations. This is not the case for the cosine values, which are always higher than 0.9. As a result, the term $1/\sin^2 \varphi$ in Eq. 4.4.3a and 4.4.3b has a considerable effect in determining the blade torque and thrust per unit length respectively. In addition, the alteration of C_L and C_D values due to the airfoils' AoA variation is small, whereas the chord length, which impacts on the forces on a linear way, cannot be significantly increased due to its non-linear upscaling on the blade mass and stiffnesses respectively [81].

Therefore, the increase of the torque per unit length produced by the blade nodes may be mostly influenced by the variations of the inflow angle and it is closely associated with the velocity triangles along the blade. A typical velocity triangle for a random radial position over the blade span is represented in Figure 5.1. However, the velocity triangle depends not only on the inflow angle and the AoA, but also on the axial and tangential induction factors and on the inflow wind speed. Hence, the determination of the spanwise velocity triangles and consequently the torque per unit length forces on the blades is complicated and requires close study via simulations. Nevertheless, from the definition of the per unit torque and thrust forces along the blade, presented by Equations 4.4.3a and 4.4.3b, it is evident that an effort to increase the blade spanwise torque force per unit length via the alteration of the previously mentioned parameters is likely to result in an increase of the blade spanwise thrust force per unit length.

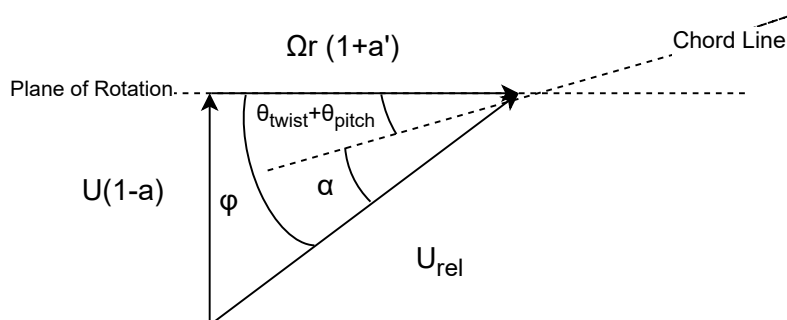


Figure 5.1: Typical velocity triangle for a random radial position along the blade span.

An increase in the spanwise thrust force per unit length is likely to be detrimental for the FOWT performance because it can lead to higher static floater pitch angles and hence to a higher inflow wind speed reduction. Hence, although FOWT power gains may be created at the aerodynamic redesign wind speeds of 10 to 12 m/s, losses are anticipated at all other partial load wind speeds. The FOWT power reduction in off-design conditions is likely driven from the greater reduction of the inflow wind speeds due to larger floater pitch angles, but also from the fact that the velocity triangle changes in off-design wind speeds. The combination of both factors may contribute in decreasing the relative wind speed seen by the blade elements, thereby reducing the per unit aerodynamic torque and thrust forces along the blade. As a result, the chord length of the airfoils, the spanwise AoA and the spanwise inflow angle should be altered in the redesign process, with the view to finding their optimal values, which result in more torque per unit length gain than thrust per unit length increase at various parts of the blade.

Aligned with the FOWT torque gain solutions, three aerodynamic redesign scenarios are examined in this project. The first will involve a variation of the local blade twist angle over the blade, whereas the second will try to increase the turbine's loading via increasing the chord length of the airfoils. As far as the third solution is concerned, it will combine the two redesign solutions via choosing the optimal blade twist angle and chord length redesign ideas, as it will be highlighted by the assessments. The scenarios for the three solutions will be assessed on the

basis of the AEP increase compared to the original FOWT configuration, while attention will be paid on the variation of static floater pitch angle and torque and thrust forces for the wind speeds of 9 and 10.5 m/s. The aforementioned wind speeds are considered as representative before and after the peak shaver is enabled respectively. In addition, the redesign process will consider an AEP error margin of 0.5%, so as to assess the validity of the redesign.

Yet, there are other aerodynamic redesign ideas that can be implemented like the blade pitch schedule alteration in the peak shaver region, the changing of the positions of the airfoils along the blade span and the substitution of the existing airfoils with more suitable ones. A refinement of the peak shaver's blade pitching schedule is likely to have an adverse effect the dynamics of the FOWT, because it will affect the maximum thrust value opted from the designers for a safe and stable operation of the FOWT [78]. In addition, the repositioning of airfoils not only is a complex solution but it requires a large amount of trial-and-error simulations in OpenFAST so as to find the best airfoil positioning on the blade span. Thereby it is deemed to be time-consuming, while its results can be easily achieved via the variation of the local twist angle variation along the blade.

Moreover, a substitution of the default DTU FFA series airfoils of the IEA 15 MW RWT would create compatibility issues with OpenFAST, as airfoil polar files should be created according to OpenFAST specifications. This process is likely to require extensive modifications, hence it is outside of the scope of this project, but is proposed for further investigation. Finally, considering that, as depicted in Subsection 4.4.2, the blade pitching due to peak shaving reduces the AoA of the airfoils for all wind speeds between 10 and 12 m/s and consequently their operational C_L/C_D value, new airfoils may be designed around the peak shaver. Those airfoils should have higher C_L/C_D values in respect to the DTU FFA series airfoils, which are maintained over a wide range of AoA. Nevertheless, this approach is not selected for this project, due to being overcomplicated and due to requiring a detailed aerodynamic study.

5.2 Section Twist Angle Variation

An aerodynamic redesign via the changing the section twist angle of the blades is likely to impact on the spanwise inflow angle and AoA distributions. This stems from the connection of the aforementioned three angles as per Equation 4.4.2b. Hence, the change in the section twist angle affects the AoA of the blade elements and their operational C_L/C_D . At the same time, the spanwise inflow angle distribution is likely to change, thereby altering the spanwise velocity triangles and the spanwise relative wind speeds. From Equations 4.4.3a and 4.4.3b, the adjustment of airfoils' C_L/C_D values and of the relative wind speed seen by the blade elements is deemed to have an effect on the spanwise per unit length torque and thrust distributions.

The first step in deciding how to alter the section twist angle of the blades is the consideration of lessons learned from the comparison of the FOWT against the BF turbine. More specifically, the blade pitching due to the peak shaver has the effect of reducing the AoA of the FOWT, compared to the BF turbine in the whole peak shaver region, therefore reducing the C_L/C_D values of the airfoils. This observation is deemed to cause a decrease in the blade per unit torque and thrust. To counter this issue, the section twist angle should decrease in all positions of the blade span, because, in this way, the AoA and consequently the C_L/C_D values can increase. Due to the AoA definition, in both cases of a positive or negative twist angle, an increase in AoA is achieved via reducing the twist angle. The AoA increase can achieve per unit blade torque and thrust force gains, which drive to FOWT power gains in the peak shaver.

Nevertheless, in the pre-peak shaver region, although an increase in AoA will be beneficial for

the inboard blade nodes ($r/R \leq 0.77$), due to their AoA being lower than their optimal one, a force deficit in the outer blade parts ($r/R > 0.77$) will be experienced, due to reduction in C_L/C_D values. As a result, there is an a priori knowledge that the FOWT will experience decrease of loading in the outboard blade part. Consequently power losses in the pre-peak shaver region are likely to occur, which should be outweighed by the gains in the peak shaver region. In addition, attention should be given on how much the section twist angle will be reduced. More specifically, the simulation results of Subsection 4.4.2 showed that the maximum AoA deficit of the FOWT in respect to the BF turbine was around 1° at the wind speed of 10.5 m/s. Therefore, the spanwise twist angle will be reduced by at maximum 1° to counter this difference.

Still, the twist angle reduction should not be the same at the whole blade span. According to Figures 4.20a and 4.20b, blade nodes at $r/R > 0.77$, which contribute the most to torque and thrust per unit length generation, operate at suboptimal AoA between 10 to 12 m/s and at suroptimal AoA for wind speeds up to 9 m/s. Hence, in case an increase of the AoA was to be done via an 1° twist angle reduction for blade nodes at $r/R > 0.77$, the AoA in the peak shaving wind speeds would be considerably increased, while the exact opposite would occur for wind speeds up to 9 m/s. Hence, although the performance of the airfoils would improve in the peak shaver region, excess losses would occur in the off-design wind speeds.

Moreover, Figures 4.19a and 4.19b depicted that after $r/R > 0.6$, the FOWT inflow angle is generally lower than 8° . For such angles, the square of relative wind speed term in the definitions of the per unit length aerodynamic torque and thrust over the blades (Eq. 4.4.3a and 4.4.3b respectively) obtains high values and it is sensitive to inflow angle variations. Thus, the per unit length aerodynamic torque and thrust of blade nodes at $r/R > 0.6$ is likely to vary considerably when the inflow angles change due to the change in AoA. This is not desired because blade nodes at $r/R > 0.6$ largely contribute to spanwise aerodynamic torque generation (shown in Figures 4.21a and 4.21b), but on the same time, they may result in excessively increasing the thrust produced by the FOWT.

Finally, the spanwise twist angle reduction should account for the nature of airfoils, especially in the inboard blade part (up to $r/R = 0.3$). This is due to the fact that the inboard airfoils comprise of cylinders and high thickness airfoils, which not only they have low C_L/C_D values but also, the relative wind velocity for those positions is low. Therefore, not only possible force gains will be low, but thrust is likely to increase at the expense of torque, due to high airfoil drag.

Having all these in mind, four section twist angle profiles were tested, named profile 1 to 4. They are presented in Figure 5.2 and analysed in Table 5.1. It is worth mentioning that, since it was opted to design as realistic blade twist variations as possible, the designed profiles were smoothed using a 3rd degree polynomial interpolation. This was done in order to avoid having abrupt chord angle variations over the blade span, which would render the blade unphysical and difficult to manufacture. A side-effect of this process is that, when the midboard blade part is considered ($0.3 \leq r/R \leq 0.6$), the twist redesign process started and finished at a bit higher blade span positions. In addition, the twist angle variation was not always to the setpoint value, but a bit higher or lower than it.

The AEP estimations, using the simulation results, suggest that all blade twist angle redesign profiles slightly increase the FOWT AEP compared to the original FOWT. Table 5.2 highlights that the FOWT AEP gain by twist angle profile 2 is the largest among all tests with an AEP increase of 0.244%. The twist angle profile 3 has also the ability to boost the FOWT's AEP, by giving a slightly lower AEP increase (0.236%) in respect to the original FOWT. Furthermore, twist angle profile number 1, although being suboptimal when weighted up to profiles 2 and 3, surpasses the 0.2% AEP gain, as other profiles. Finally, the midboard twist angle decrease by

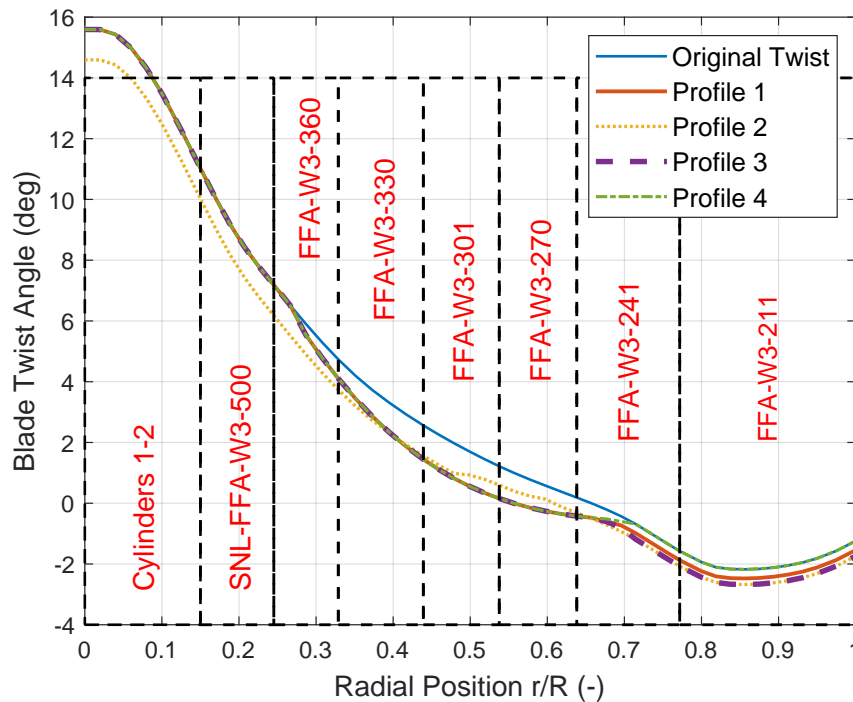


Figure 5.2: Comparison of the spanwise blade twist profiles for the aerodynamic redesign of the IEA 15 MW FOWT. Solid blue curve: Original blade twist angle variation. Solid orange curve: Inboard twist angle equal to original profile, midboard blade twist decrease of 1° , followed by an outboard 0.3° decrease. Dotted yellow curve: Inboard and midboard twist angle decrease of 1° followed by a 0.3° decrease towards the tip. Dashed purple curve: Inboard twist angle equal to original twist angle variation, midboard twist angle decrease of 1° , followed by a 0.5° twist angle decrease towards the tip. Dashed green curve: Midboard twist angle reduction by 1° , inboard and outboard twist angle equal to original values.

1° , creates AEP gains, which are smaller than other profiles. This may be attributed to the fact that it does not consider a blade twist reduction towards the blade tip, as with other blade twist redesign profiles.

This observation, combined with the optimality of profile 2, points to the direction of reducing the twist angle at the whole blade span. Also, the comparison of AEP gains of profile 2 and 3, which have a higher blade twist reduction towards the tip, suggests that the twist angles towards the tip should be considerably decreased. Nevertheless, the simulations indicated that an outboard twist angle reduction higher than 1° deteriorated the performance of the FOWT due to excessive blade loading in the peak shaver and high wind speed deficit in the pre-peak shaver region due to higher static floater pitch angles. Therefore, the optimality region for the outboard twist angle decrease is likely to be $[0.5^\circ, 1^\circ]$.

To explain the results, the power produced by the FOWT according to the different twist angle profiles should be examined. However, since the power variations are small between the profiles, the power generation between the blade twist profiles will be compared according to their power at 9 m/s and 10.5 m/s respectively (shown in Figures 5.3a and 5.3b), since they are representative wind speeds for the pre-peak and peak shaver regions respectively. A more complete depiction of the FOWT power curves according to the redesign scenarios are presented for the sake of completeness in Figure B.1 of Appendix B.1 of this work.

As pointed by Figures 5.3a and 5.3b, twist profile 3 and 4 result in boosting the FOWT power

Table 5.1: Description and reasoning of the four twist angle profiles used for the aerodynamic redesign of the IEA 15 MW RWT FOWT considered in this project.

Twist Profile Index	Blade Inboard Part ($0 \leq r/R \leq 0.3$)	Blade Midboard Part ($0.3 < r/R \leq 0.65$)	Blade Outboard Part ($0.65 < r/R \leq 1$)	Reasoning
Twist Profile 1	Original Twist Profile	Reduction of approx. 1°	Reduction of approx. 0.3°	Increase in AoA, spanwise torque and thrust from $r/R=0.3$ onwards. However, smaller effect of AoA to spanwise forces for $r/R \geq 0.65$.
Twist Profile 2	Reduction of 1°	Reduction of 1°	Reduction of 0.5°	Test of hypothesis of more spanwise torque than thrust up to $r/R=0.65$. Aggressive twist angle reduction from $r/R=0.65$ onwards for higher AoA, torque and thrust forces.
Twist Profile 3	Original Twist Profile	Reduction of approx. 1°	Reduction of 0.5°	Same as twist profile 1. More aggressive twist angle reduction from $r/R \geq 0.65$ than profile 1.
Twist Profile 4	Original Twist Profile	Reduction of approx. 1°	Original Twist Profile	AoA and torque and thrust increase in the midboard blade part. Same AoA and loading as original FOWT in other blade areas.

Table 5.2: Comparison of the AEP, the AEP increase compared to the original FOWT and the AEP deficit compared to the BF wind turbine for the original FOWT and the redesigned FOWT, according to the four blade twist profile variations.

	Original FOWT	FOWT Twist Profile 1	FOWT Twist Profile 2	FOWT Twist Profile 3	FOWT Twist Profile 4
AEP (GWh)	60.341	60.472	60.488	60.483	60.433
AEP Increase Compared to Original FOWT (%)	–	0.217	0.244	0.236	0.154
FOWT AEP Decrease Compared to BF (%)	2.932	2.721	2.695	2.702	2.782

generation at an average wind speed of 10.5 m/s more than the other two redesign profiles. Yet, the exact opposite trend is observed for the wind speed of 9 m/s, where profiles 2 and 3 result in the FOWT losing more power than profiles 1,4 as well as producing less power than the original FOWT design. One of the explanations for the power deficit of profiles 2 and 3 lies in the static floater pitch angles, represented in Figure 5.4 for all profiles examined. The simulation results point out that profiles 2 and 3 result in an approximately 0.18° increase in the static floater pitch angle at all wind speeds, compared to the original FOWT configuration, while being the highest for all examined profiles.

As a result, a reduction of the twist angle in the whole blade span and especially in the outboard

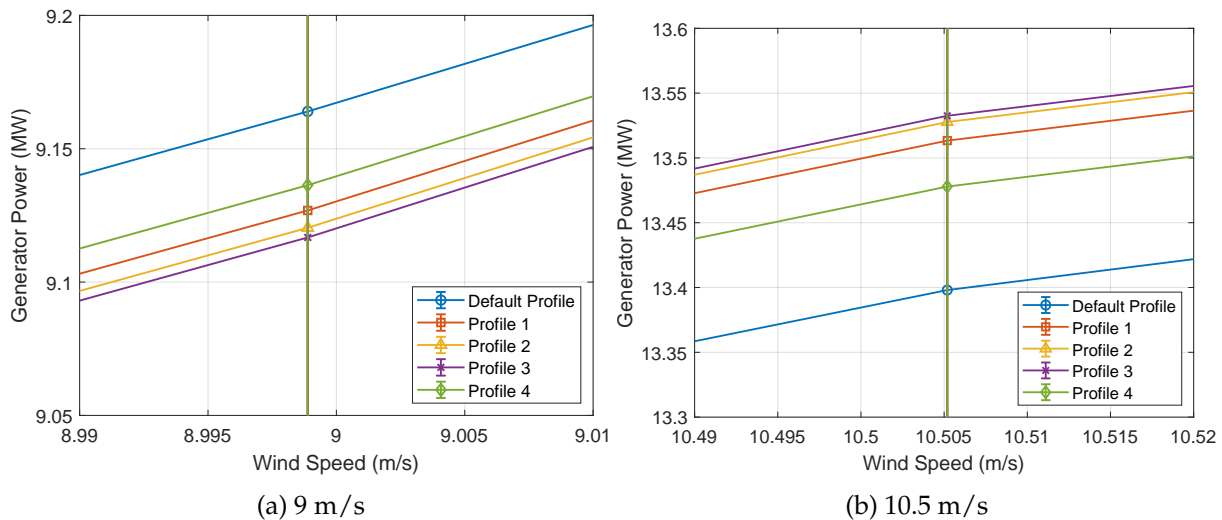


Figure 5.3: Power generation of the IEA 15 MW FOWT according to the original and the redesigned blade twist angle profiles for the average wind speeds of 9 and 10.5 m/s respectively. Blue curve: Original blade twist angle profile. Orange curve: Blade twist profile 1. Orange curve: Blade twist profile 2. Purple curve: Blade twist profile 3. Green curve: Blade twist profile 4.

blade part results in increasing the FOWT blade loading. Although it is beneficial for wind speeds in the peak shaver region, it results in decreasing the inflow wind speeds in the pre-peak shaver region, thereby incurring power losses. The aforementioned observations are true for other wind speeds of the two examined wind speed regions. Nevertheless, due to the wind speed probability function, which is used for the representation of the wind conditions of the site studied in this project (shown in Figure 3.4), the peak shaver gains have nearly the same weight as the pre-peak shaver losses. Hence, AEP gains are observed from the blade twist angle redesign process.

In order to understand how each blade twist profile affects the power generation and the static pitch angles of the FOWT, the variation of the relative wind speed along the FOWT blades should be examined. This stems from the fact that, as proposed by Equations 4.4.3a and 4.4.3b, the relative wind speed affects the torque and thrust per unit length of the FOWT blades. Generally, the relative wind speed of the blade nodes increases towards the outer blade part, as depicted by the schematic of the velocity triangles along the blade (Figure 5.1). However, the simulations showed that the relative difference of the average values of the spanwise relative wind speed of the redesigned FOWT compared to that of the original FOWT is at maximum 0.1% at all radial positions. Hence, the examination of the spanwise relative wind speed according to the different twist angle redesign solutions should zoom on a narrow part of the blade in order to better observe the changes.

More specifically, the spanwise radial position of 0.715 was chosen as representative for the inner and outer blade parts. The relative wind speed of the redesigned FOWT blades at $r/R=0.715$ is shown in Figures 5.5a and 5.5b. For an average wind speed of 9 m/s, the relative wind speed at $r/R=0.715$ reduces for all twist angle redesign solutions, whereas the exact opposite trend is observed at 10.5 m/s. It should be mentioned that same results were observed for the other radial positions considered in this project. Hence, it is clear that, for the redesign wind speed of 10.5 m/s and likely for all wind speeds in the peak shaver, all blade twist angle profiles are beneficial for the FOWT, since they boost the relative wind speed seen by the blades.

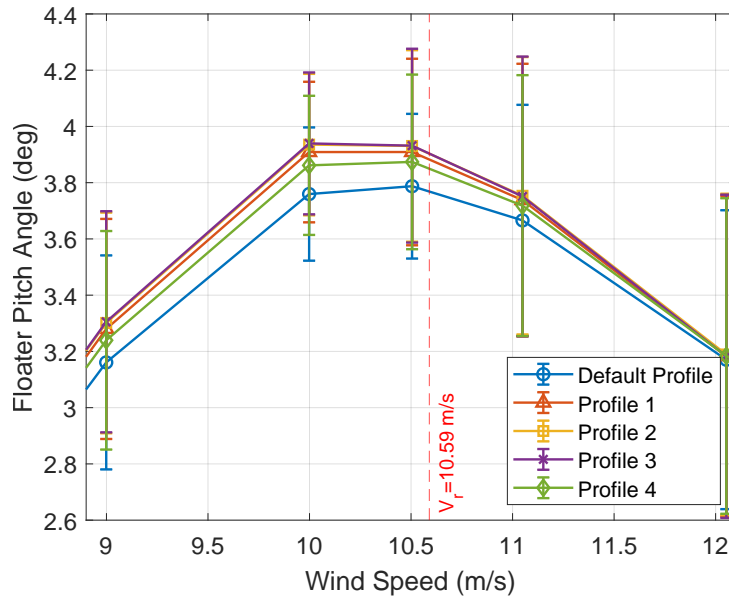


Figure 5.4: Variation of the static floater pitch angle of the IEA 15 MW FOWT according to the original and the redesigned blade twist angle profiles for average wind speeds between 9 and 12 m/s. Blue curve: Original blade twist angle profile. Orange curve: Blade twist profile 1. Orange curve: Blade twist profile 2. Purple curve: Blade twist profile 3. Green curve: Blade twist profile 4.

On the other hand, for off-design wind speeds (i.e lower than 9 m/s), the change of the spanwise twist angle is proven to be detrimental for the spanwise relative wind speed. It should be mentioned that, although the average values of the relative wind speed of the original and the redesigned FOWT are very close to each other, their standard deviation is at the excess of 2 m/s. This probably drives to the conclusion that the actual relative wind speed variations of the redesigned FOWT may even higher than depicted in Figures 5.5a and 5.5b.

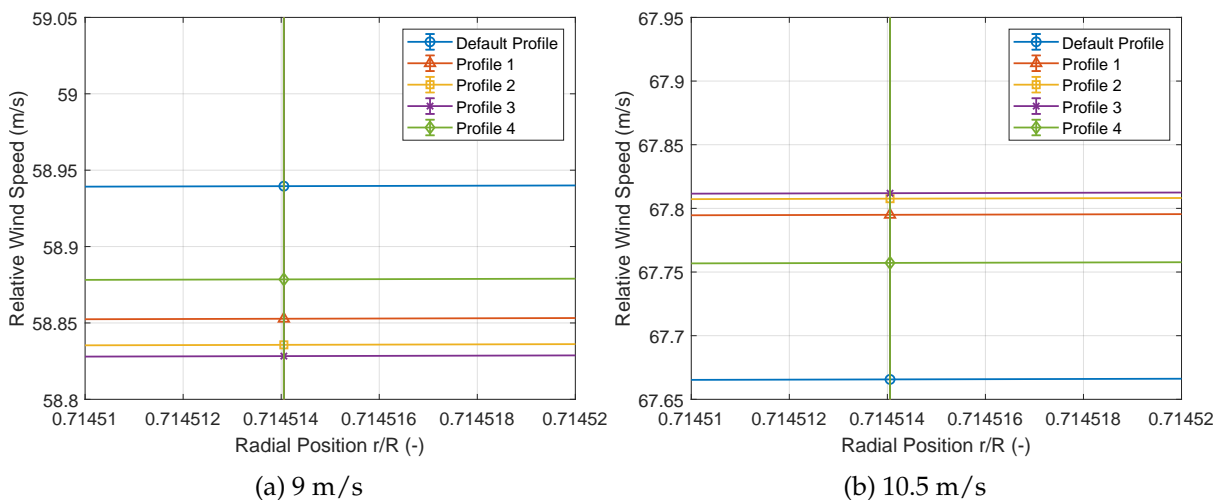


Figure 5.5: Variation of the relative wind speed at the radial position of 0.715 of the IEA 15 MW FOWT according to the original and the redesigned blade twist angle profiles for average wind speeds of 9 and 10.5 m/s. Blue curve: Original blade twist angle profile. Orange curve: Blade twist profile 1. Orange curve: Blade twist profile 2. Purple curve: Blade twist profile 3. Green curve: Blade twist profile 4.

However, to explain the motive forces behind the observed variations of the relative wind speed

on the blades of the FOWT according to the chord length redesign profiles, the spanwise inflow angles, the spanwise induction factors and the inflow wind speed on the FOWT rotor should be examined as well. This is due to the fact that all quantities are associated via Equation 4.4.3c. The inflow angle along the span for wind speeds of 9 m/s and 10.5 m/s is depicted in Figures 5.6a and 5.6b respectively. It can be deduced that for the whole partial load region, the inflow angle of all blade twist redesigns reduces at the whole blade span. This is due to the observed reduction of the rotational speed of the rotor and of the increase of the induction factor. However, the inflow angle reduction is maximum in the midboard blade elements, with only an approximately 0.5° reduction in this region. On the other hand, the inboard and outboard blade elements experience a slight inflow angle reduction. It should be noted that the inflow angle reduction is smaller for wind speeds where the peak shaver is enabled (i.e. 10-11 m/s).

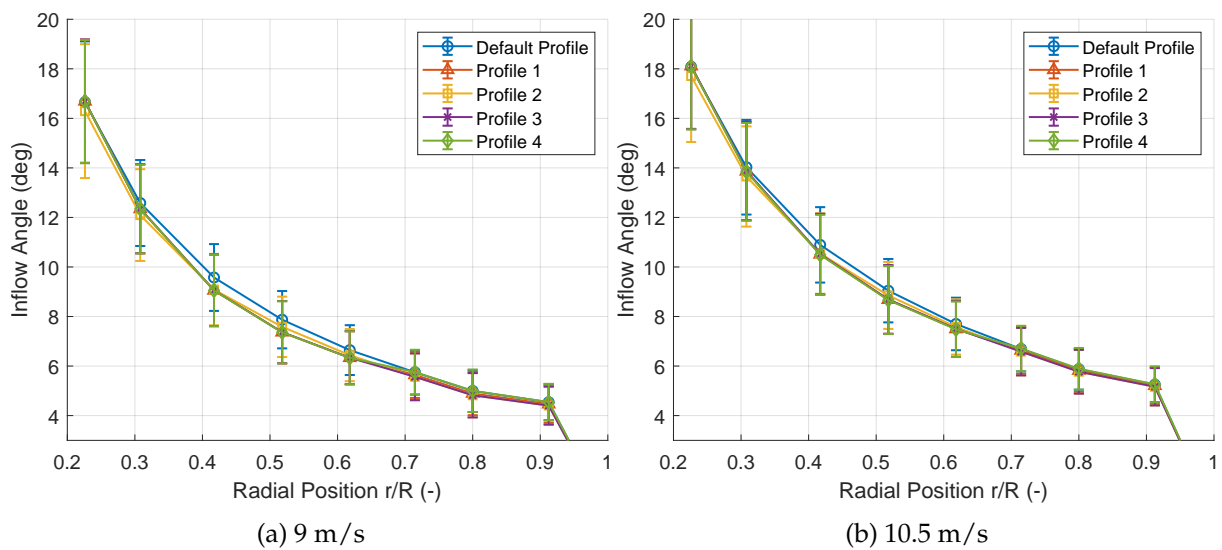


Figure 5.6: Spanwise inflow angle variation of the IEA 15 MW FOWT according to the original and the redesigned blade twist angle profiles for average wind speeds of 9 and 10.5 m/s. Blue curve: Original blade twist angle profile. Orange curve: Blade twist profile 1. Orange curve: Blade twist profile 2. Purple curve: Blade twist profile 3. Green curve: Blade twist profile 4.

Furthermore, twist angle profile 3 results in the highest inflow angle reduction observed over the simulations, a fact which creates higher relative wind speed gains. On the other hand, profile 2 has nearly the same inflow angle variation as profile 3, while being less steep towards the tip, resulting in a smaller relative wind speed increase. In addition, at both wind speeds examined, the inflow angle does not vary significantly for $r/R > 0.70$, because it is mostly dominated by the increase in the rotational velocity. To sum up, from this analysis, it is clearly described that the twist angle reduction according to all profiles tested in this project results in decreasing the spanwise inflow angle.

Nevertheless, the inflow angle reduction compared to the the original FOWT tends to be even larger for wind speeds lower than 9 m/s, i.e in the pre peak shaver region. Hence, the inflow angle reduction observed in both design and off-design wind speeds, is likely to be beneficial for the relative wind speed, as from its definition 4.4.3c, it has the potential of increasing the relative wind speed, and consequently the per unit length spanwise torque and thrust forces. It should be noted that the loading gain will be possibly higher for $r/R > 0.65$, due to the lower inflow angle values.

In addition, the variation of the axial induction factor should be studied for determining the

potential of the twist angle profiles for improving the FOWT performance. The spanwise distribution of the axial induction factor along the blades of the original and the redesigned FOWT according to the proposed twist angle profiles is depicted in Figures 5.7a and 5.7b for wind speeds 9 and 10.5 m/s respectively. From the aforementioned figures, it can be deduced that twist angle profiles 1 to 4 result in an increase of the axial induction factor along the FOWT blade span compared to the original twist profile for both 9 m/s and 10.5 m/s. Still, the increase of the axial induction factor is more profound for the pre-peak shaver wind speeds ($U < 9$ m/s) and for radial positions lower than 0.7. This can be attributed to the high reduction of the twist angle that was selected up to this radial position.

The increase of the axial induction factor that was observed during the simulations is deemed to be a possible reason for lowering the FOWT performance when the alteration of the blade twist angle is considered for the redesign of the FOWT. This conclusion is driven from the definition of the relative wind speed over the FOWT blades (Eq. 4.4.3c), which clearly shows that an increase in the axial induction factor may result in decreasing the relative wind speed, and hence the torque and thrust per unit length of the blades, as per Eqs. 4.4.3a and 4.4.3b respectively. Finally, as far as the inflow wind speed is concerned, Figures 5.8a and 5.8b highlight that at both 9 m/s and 10.5 m/s, the inflow wind speed over the rotor decreases. This is connected with the higher static floater pitch angles observed in Figure 5.4, which also result in being detrimental for the relative wind speed seen by the blades as well.

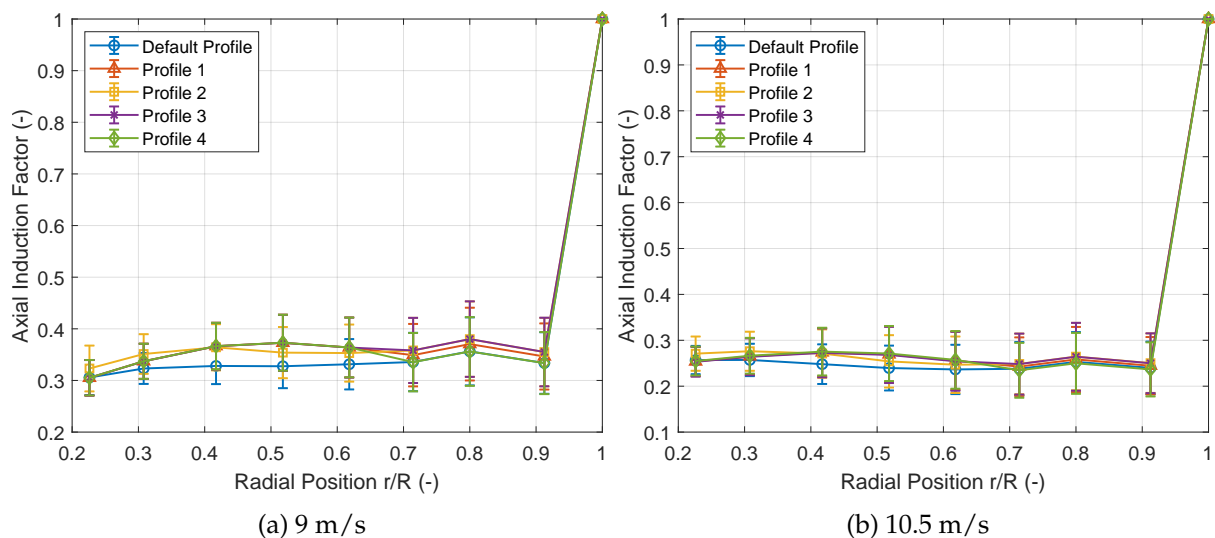


Figure 5.7: Spanwise variation of the axial induction factor of the IEA 15 MW FOWT according to the original and the redesigned blade twist angle profiles for average wind speeds of 9 and 10.5 m/s. Blue curve: Original blade twist angle profile. Orange curve: Blade twist profile 1. Orange curve: Blade twist profile 2. Purple curve: Blade twist profile 3. Green curve: Blade twist profile 4.

From the aforementioned analysis, it is evident that the variation of the relative wind speed between 4-9 m/s and 10-12 m/s is heavily dependent on the variations of the velocity triangles over the blade span at these wind speed ranges. Between 4 to 9 m/s, for all twist angle profiles examined, the combined effect of increase of the induction factor from approximately 0.33 to values ranging from 0.35 to 0.38 and of the reduction of the inflow wind speeds, is likely to outweigh the decrease of the inflow angle observed in this wind speed region for the majority of blade spanwise positions. Thus, a relative wind speed reduction is observed in Figure 5.5a for 9 m/s, which can be indicative of other wind speeds between 4 to 9 m/s.

On the contrary, in the redesign wind speeds (i.e 10-12 m/s), the combination of the induction

factor values, which are 0.27 at maximum, and of the observed inflow wind speeds and inflow angles, may ultimately create relative wind speed gains for the redesign cases. The combination of those values is a possible explanation why, as shown in Figure 5.5b, all redesign twist angle profiles achieve higher relative wind speeds over the blade span for wind speeds between 10 m/s and 12 m/s. Therefore, it is anticipated that all the redesign of the FOWT blades according to twist angle profiles 1-4 is expected to create spanwise torque and thrust per unit length gains in the peak shaver region (10-12 m/s) and to reduce the aforementioned quantities in the off-design wind speeds (up to 9 m/s).

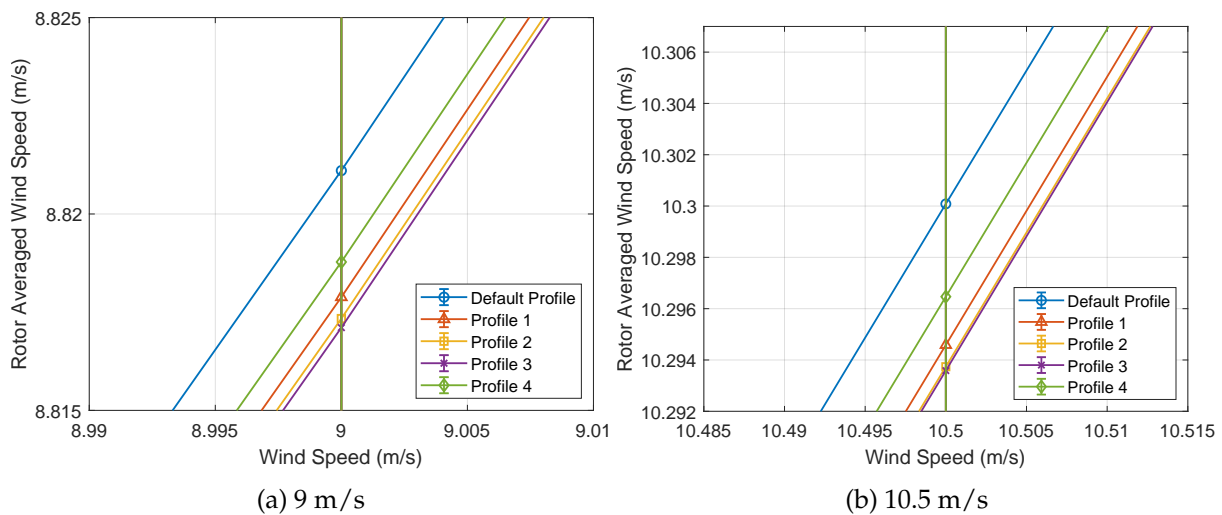


Figure 5.8: Rotor averaged wind speeds of the IEA 15 MW FOWT according to the original and the redesigned blade twist angle profiles for average wind speeds of 9 and 10.5 m/s. Blue curve: Original blade twist angle profile. Orange curve: Blade twist profile 1. Orange curve: Blade twist profile 2. Purple curve: Blade twist profile 3. Green curve: Blade twist profile 4.

One other indicator that should be evaluated for the blade twist redesign process is the spanwise AoA variation, which is presented in Figures 5.9a and 5.9b for average wind speeds 9 and 10.5 m/s respectively. Although by definition, AoA depends on the inflow angle and blade pitch angle variations, the results suggest that the reduction of the blade twist angle achieves its target of increasing the AoA along the blade, compared to the original FOWT twist distribution. Yet, it should be mentioned that, as it is depicted in Figure 5.9a, at 9 m/s and for the whole pre-peak shaver region, the AoA increase, especially by profiles 2 and 3, deteriorates the performance of the exterior blade airfoils ($r/R > 0.77$) because it leads them to suroptimal regions, where lift over drag reduces, even though FFA-W3-211 airfoil has a relatively shallow optimal region.

This drives to the conclusion that, although there are C_L/C_D gains in the interior blade part, the C_L/C_D reduction towards the tip is detrimental for the generation of torque and thrust forces. Interestingly, the correlation of the AEP increase indicator with the AoA variation, proposes that a relatively high increase of the AoA in the inboard and outboard blade elements, followed by a mild increase in the inboard section, as in profile 2, is likely to achieve higher performance gains. Therefore, the redesign effort should pursue towards such twist angle profiles.

Since the spanwise relative wind speed and AoA variations have been presented, their impact on the torque and thrust forces should be examined for the whole partial load wind speeds. According to Figures 5.10a and 5.10b, at an average wind speed of 9 m/s, for all blade twist profiles the spanwise thrust increases much more than the spanwise torque. The latter not only shows a small increase up to $r/R=0.6$, but it starts to decrease towards the tip, especially for profiles 2 and 3. On the same time, profiles 2 and 3 have a higher thrust force towards the tip,

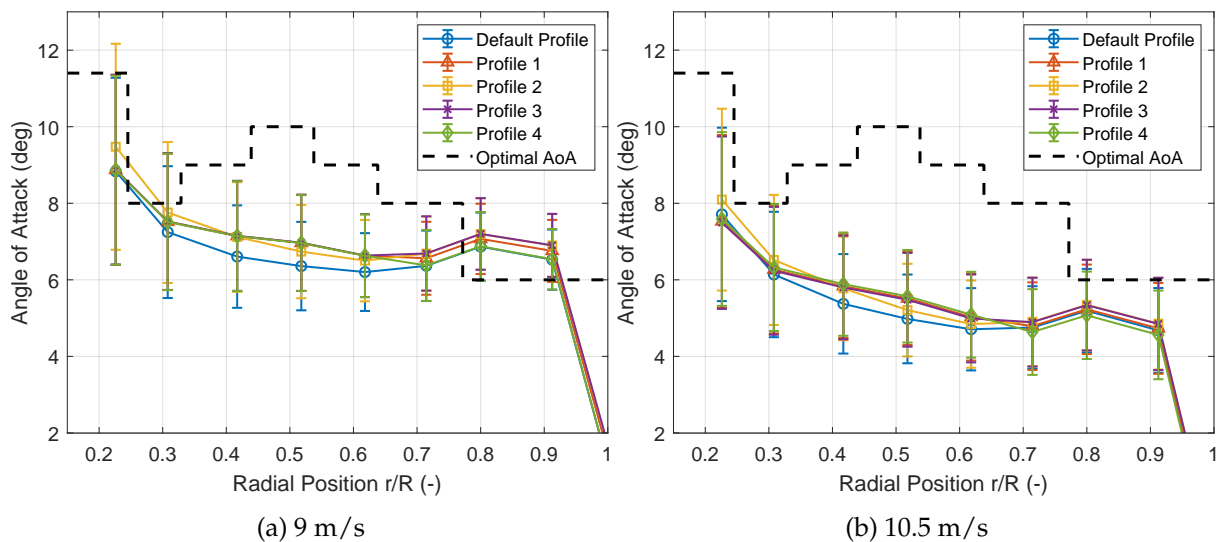


Figure 5.9: Spanwise angle of attack variation of the IEA 15 MW FOWT blades according to the original and the redesigned blade twist angle profiles for the average wind speeds of 9 and 10.5 m/s respectively. Blue curve: Original blade twist angle profile. Orange curve: Blade twist profile 1. Orange curve: Blade twist profile 2. Purple curve: Blade twist profile 3. Green curve: Blade twist profile 4.

which explains the reason for the high FOWT blades' out-of plane loading and the resulting power decrease due to the increased static floater pitch angle. For an average wind speed of 10.5 m/s and for the whole peak shaver region, Figures 5.11a and 5.11b show that, although the spanwise thrust produced by the blades, according to all tested twist angle profiles, increases much, compared to the original profile, significant torque force gains start to emerge in the whole blade span.

Moreover, as highlighted by the thrust and torque variations for the two wind speeds examined, in order to create force gains and on the same time increase torque more than thrust, a less step twist angle reduction is the inboard blade part, followed by a slightly twisted blade towards the tip, as described by twist angle profile 2, is preferred against other profiles. In this way, a more gradual spanwise torque and thrust gain occurs, which also considers the outboard blade part, contributing the most to both forces. Nevertheless, this redesign idea results in the highest torque reduction compared to the thrust increase in the pre-peak shaver region, which leads to power losses at wind speeds up to 9 m/s.

However, the power gain in the peak shaver region and its contribution to energy production due to the wind speed distribution, outweighs the power loss in the pre-peak shaver region. Finally, it should be noted that the AEP gains are within the selected error margin of this project (0.5%), which signifies that the results are inconclusive. Hence, a more detailed study of the redesign should be done, which will consider a higher resolution of wind speeds, as well as a high fidelity simulation package.

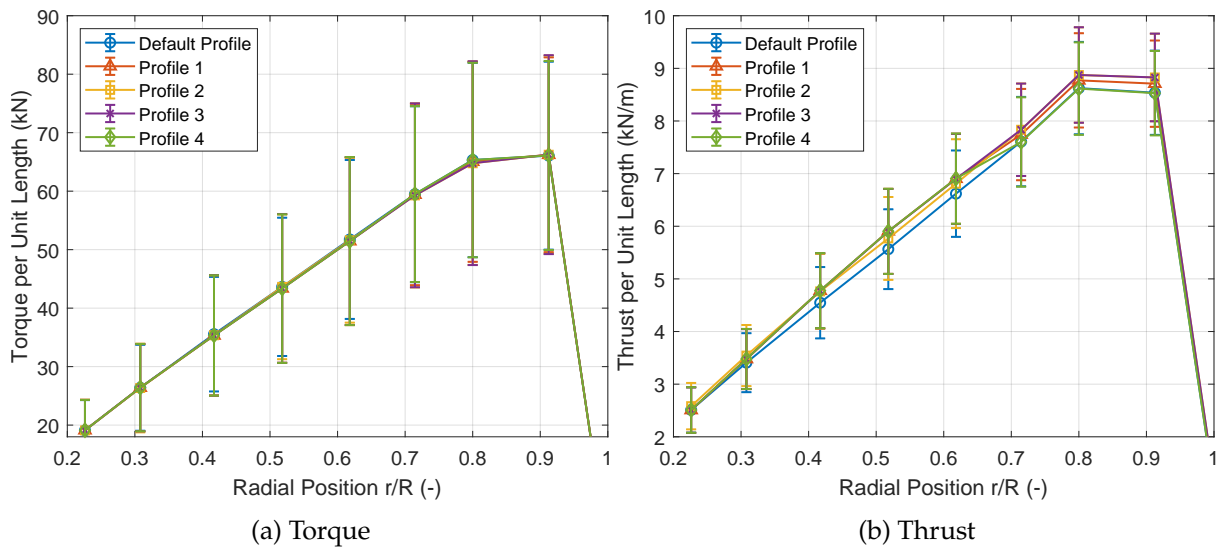


Figure 5.10: Spanwise torque and thrust variation of the IEA 15 MW FOWT blades according to the original and the redesigned blade twist angle profiles for the average wind speed of 9 m/s. Blue curve: Original blade twist angle profile. Orange curve: Blade twist profile 1. Orange curve: Blade twist profile 2. Purple curve: Blade twist profile 3. Green curve: Blade twist profile 4.

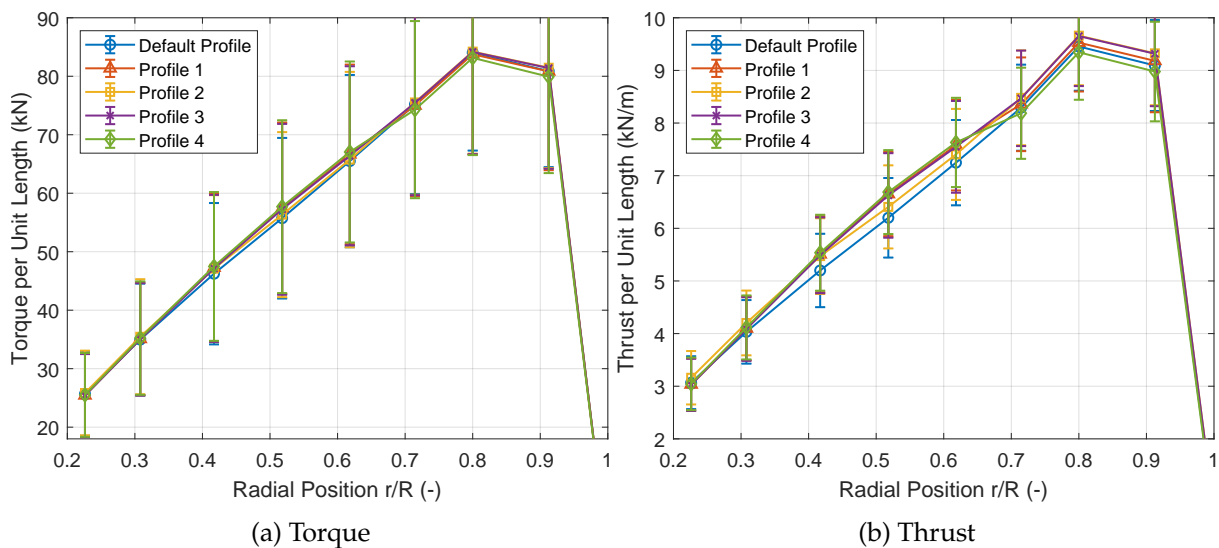


Figure 5.11: Spanwise torque and thrust variation of the IEA 15 MW FOWT blades according to the original and the redesigned blade twist angle profiles for the average wind speed of 10.5 m/s. Blue curve: Original blade twist angle profile. Orange curve: Blade twist profile 1. Orange curve: Blade twist profile 2. Purple curve: Blade twist profile 3. Green curve: Blade twist profile 4.

5.3 Chord Length Variation

The first aspect for the aerodynamic redesign of the FOWT via increasing the airfoils' chord length is to determine the upscaling strategy. Firstly, considering the manufacturability of the blade, it is opted to not to change the shape of the chord distribution over the blade span and to keep it similar to that of the original IEA 15 MW RWT. Also, the redesigned chord profiles do not include abrupt spanwise chord length variations and a decreasing trend of the chord length towards the blade tip is used. In this way, the blade can be redesigned in a more realistic

way. To account for the mass per length and edgewise and flapwise stiffness increase due to the increase of the chord length, the blade scaling laws are used. More specifically, the mass per unit length and edgewise and flapwise stiffnesses scale by the ratio of chord in the power of 2 and 4 respectively [81]. The blade natural frequencies are independent from the upscaling process due to being normalised with the rotor speed [81].

Secondly, the blade parts near the root ($r/R \leq 0.245$), which are comprised by the cylindrical airfoils 1 and 2 and by the high relative thickness SNL-FFA-W3-500 airfoil, should not be upscaled, because they do not significantly contribute in torque and thrust force generation. In addition, as shown by the scaling laws, an upscaling of the inboard blade part would cause a rapid mass and stiffness increase, thus causing implications on the blade and the rotor hub gravitational loads. On top of that, the redesigned blade would become more material-intensive, and consequently more expensive. In addition, the value of the maximum chord length and its position on the blade ($c_{max} = 5.767m$ at $r/R=0.21$) is opted not to change during the chord upscaling process. This stems from the fact that a chord variation up to nearly $r/R=0.21$ is likely not to have a profound effect on the blade loading due to the low rotational velocities in this region, which result in lower relative wind speeds. Finally, the chord length profiles were smoothed via a 3rd degree polynomial function.

The chord length redesign profiles that were created for the IEA 15 MW FOWT redesign are presented in Figure 5.12 and analysed in Table 5.3. It should be noted that the turbulent wind simulations under a TI value of 10% suggested that for the wind speed of 10.5 m/s, the maximum difference of the FOWT per unit torque compared to the one of BF turbine was nearly 6% lower in the interior and the exterior blade parts. As a result, due to the linear relationship of the torque with the chord length, the lower bound of the chord length increase is 6%. In addition, the 12% cutoff percentage in the chord length increase is chosen because the simulations pointed that FOWT performance deterioration and high blade mass increase occurred after this value.

Table 5.4 highlights that the increase of the chord length of the FOWT according to the examined profiles results in a slight increase of the FOWT AEP. More specifically, chord profile 2 shows the largest AEP increase (0.154%), whereas chord profile 4 shows the smallest AEP increase, with only 0.044% AEP gain. In addition, due to the AEP gains, the FOWT according to profile 2, results in the smallest AEP deficit compared to the BF turbine (2.782%). In addition, the increase of chord along the span is more beneficial for the FOWT AEP due to more loading on the whole blade. Therefore, it is evident that a mild chord length increase of around 6% is able to create AEP gains for the FOWT, whereas, as the chord length increase becomes higher than this value, the AEP gain is continuously diminished. However, to provide an argumentation of the reasons behind the aforementioned results, indices like the generated power of the FOWT, the static floater pitch angle, the inflow angle, the AoA and the torque and thrust forces on the blade should be closely examined.

As far as the FOWT power generation is concerned, Figure 5.13a depicts that the increase of the chord length creates different trends in the power curves of the FOWT. More specifically, although in the peak shaver region (10 to 12 m/s), an increase of the chord length creates power gains, the exact opposite trend occurs in the pre-peak shaver region which is up to 9 m/s. In fact, the increased loading from the chord angle increase has a negative effect on the static floater pitch angle, as highlighted in Figure 5.13b. From the aforementioned figure, it is evident that the static floater pitch angle increases significantly for all wind speeds between 9 and 12 m/s, whereas same results are drawn for wind speeds between 6 and 8 m/s.

Therefore, the chord length redesign, which considers the power gains in the peak shaver,

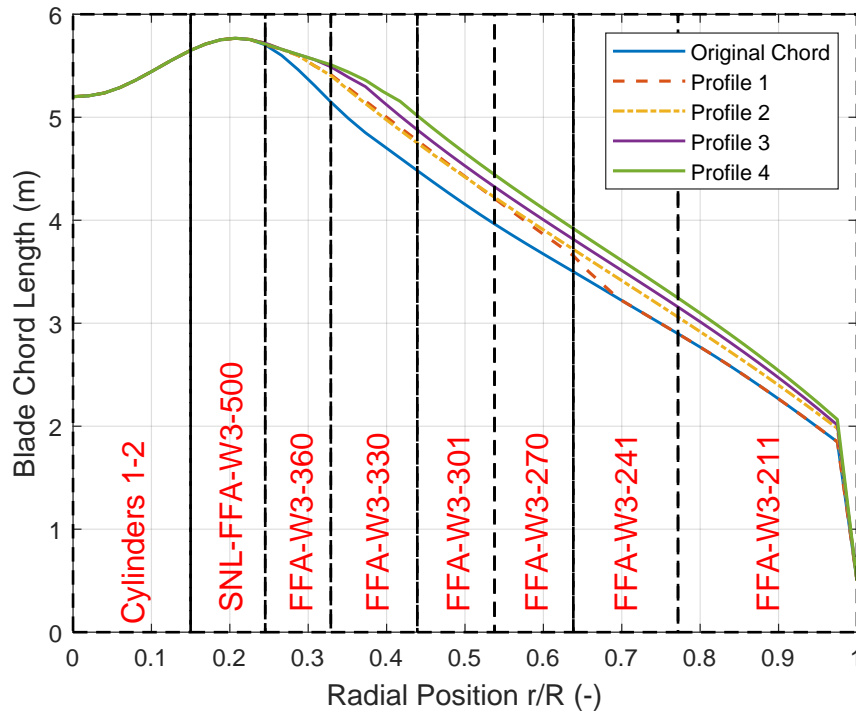


Figure 5.12: Comparison of the spanwise chord length profiles for the aerodynamic redesign of the IEA 15 MW FOWT. Solid blue line: Original chord length variation. Dashed orange line: 6% chord length increase in the inboard blade part. Dashdotted yellow : 6% chord length increase in the whole blade. Solid purple and solid green curves: 9% and 12% spanwise chord length increase respectively.

Table 5.3: Description and reasoning of the four chord length profiles used for the aerodynamic redesign of the IEA 15 MW RWT FOWT considered in this project.

Chord Length Profile Index	Chord Length Variation from $r/R > 0.25$	Reasoning
Chord Profile 1	+6 % up to $r/R=0.68$	Selection of the lower bound of chord length increase. Limiting of the per unit length thrust increase by considering blade elements up to $r/R=0.68$ so as not to result in high thrust per unit length increase, when trying to increase the torque per unit length.
Chord Profile 2	+6%	Same reasoning as chord profile 1. However, testing of whether a chord length increase over the whole blade span is able to result in more performance gains than a chord length increase up to $r/R=0.68$.
Chord Profile 3	+9%	Higher chord length increase than the baseline of 6%.
Chord Profile 4	+12%	Highest chord length increase than the baseline of 6%. Performance deterioration observed after a 12% chord length increase.

Table 5.4: Comparison of the AEP, the AEP increase compared to the original FOWT and the AEP deficit compared to the BF wind turbine for the original FOWT and the redesigned FOWT, according to the four chord length profile variations.

	Original FOWT	FOWT Chord Profile 1	FOWT Chord Profile 2	FOWT Chord Profile 3	FOWT Chord Profile 4
AEP (GWh)	60.341	60.418	60.433	60.416	60.367
AEP Increase Compared to Original FOWT (%)	–	0.128	0.154	0.124	0.044
FOWT AEP Decrease Compared to BF (%)	2.932	2.807	2.782	2.811	2.889

results in a higher static floater pitch angle in the pre-peak shaver region, which reduces the inflow wind speed seen by the blades, thereby reducing their aerodynamic performance and explaining the FOWT power deficit in wind speeds below 10 m/s. Although as pointed by the results, the energy production from wind speeds between 10 and 12 m/s has a higher contribution to AEP, the contribution of wind speeds between 7 and 9 m/s is quite significant as well as shown in Figure 3.4. Hence, the power and energy gains in the peak shaver region, created by the increased chord length, are marginally higher than the losses experienced in the rest of the partial load region.

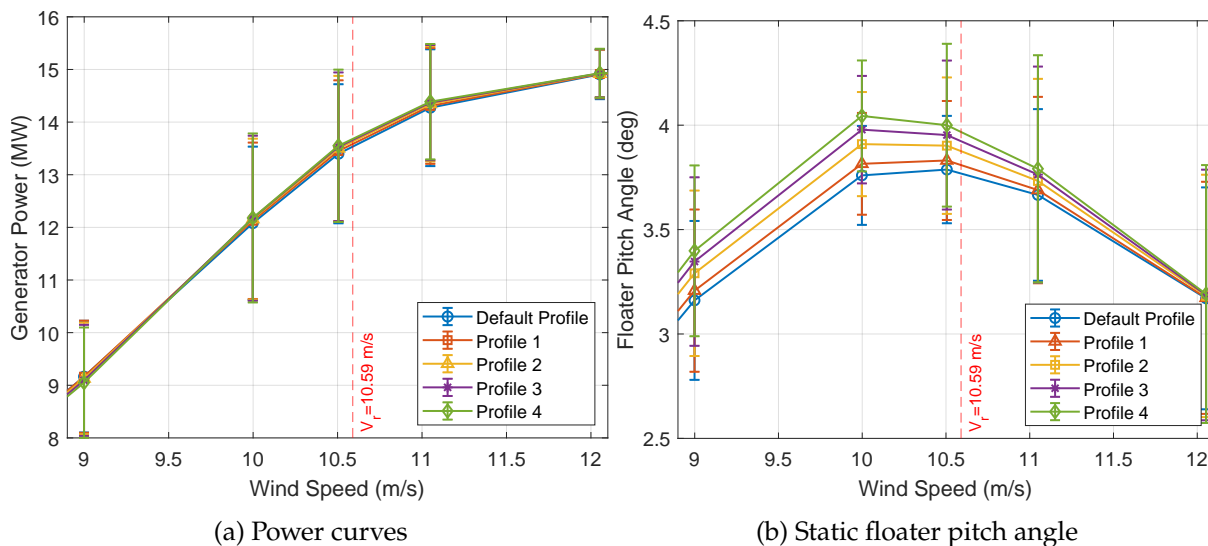


Figure 5.13: Power curves and static floater pitch angles of the original and the redesigned FOWT, according to the chord length increase profiles studied in this project and for wind speeds between 9 and 12 m/s. Blue curves: Original chord length profile. Orange curves: Chord length profile 1. Yellow curves: Chord length profile 2. Purple and Green curves: Chord length profiles 3 and 4 respectively.

To conclude, the potential of the chord length profile 2 to boost the FOWT AEP stems from the fact that, although it does not create high power gains in the peak shaver region, its losses at the off-design wind speeds tend to be lower than other profiles. At the same time, the observed static floater pitch angles of chord length profile 2 are considerably lower than profiles 3 and

4. Hence, it leads to smaller inflow wind speed reduction at the whole partial load region, compared to other chord length profiles. Thus, although the redesigned FOWT according to chord length profile 2 experiences a loading and power deficit, compared to the original FOWT, those deficits are smaller than the ones caused by chord length profiles 3 and 4 respectively.

In order to explain the power variations of the redesigned FOWT according to the chord length profiles tested in this project, the parameters which influence the per unit torque and thrust forces on the blades should be examined. More specifically, it is known that the increase of the chord length is likely to result in an increase in the blade in-plane and out of plane loading. However, since by definition (Eq. 4.4.3a and 4.4.3b), the per unit blade torque and thrust forces are dependent on the relative wind speed and on the AoA, both indices should be examined in addition to the chord length. Again, the wind speeds of 9 and 10.5 m/s will be considered as representative wind speeds for the design and off-design operational points. For the analysis of the variation of the spanwise relative wind speeds, the blade node at $r/R=0.715$ will be examined, for the same reasons as in Section 5.2.

To begin with, Figures 5.14a and 5.14b depict that although at 10.5 m/s the relative wind speed seen by the blades increases, the exact opposite occurs at 9 m/s. Those observations can be expanded for other wind speeds in the partial load region. More specifically, as the chord length of the blades increases, the relative wind speed is boosted in the peak shaver region, compared to the original FOWT. However, a maximum chord length increase of 12% results in lowering the spanwise relative wind speeds at 9 m/s, a fact which can be generalised for all wind speeds below 9 m/s. The aforementioned trends regarding the relative wind speeds along the blade can be attributed to the spanwise inflow angles, to the spanwise induction factors and to the inflow wind speed, as proposed by Equation 4.4.3c.

Starting with the inflow wind speeds, due to the increased static floater pitch angle compared to the original FOWT design, all redesign cases experience a reduction in their inflow wind speeds. Same trends are observed as in the blade twist angle case (depicted in Figures 5.15a and 5.15b). In fact, since Figure 5.13b showed that a higher chord length is associated with higher static floater pitch angles, chord profile 4 is anticipated to have the largest reduction in inflow wind speeds when compared to other profiles.

The next step in describing the observed relative wind speed variations according to the studied chord length profiles is to delve on the variations of the inflow angle along the blade. According to Figures 5.15a and 5.15b, for all wind speeds in the partial load region, the inflow angle of all nodes along the span slightly decreases as the spanwise airfoil chord length increases. The decrease of the inflow angle can be explained by its definition (Eq. 4.4.2a). As noted by the simulations, the increase of the chord length led to higher rotational speeds (presented in Figure 5.17a) due to higher rotor loading, higher induction factor values (as depicted in Figures 5.15a and 5.15b) and to lower inflow wind speeds. Nevertheless, it should be noted that the inflow angle reduction is more prevalent for wind speeds up to 9 m/s, due to the larger sensitivity of the aforementioned parameters in this wind speed region.

All in all, the increase in the spanwise chord length results in decreasing the spanwise inflow angle and the inflow wind speeds, while an increase of the induction factor was observed for all wind speeds examined in this project. Nevertheless, since the values of the aforementioned parameters have a different interplay at the studied wind speeds, it is probable that, as shown by Equation 4.4.3c, their combinations result in higher spanwise relative wind speeds in the redesign wind speeds. On the contrary, their obtained values at off-design wind speeds possibly explain why the relative wind speed decreases between 6 to 9 m/s. Hence, from the definition of the per unit length torque and thrust, it is anticipated that up to 9 m/s, the lower relative

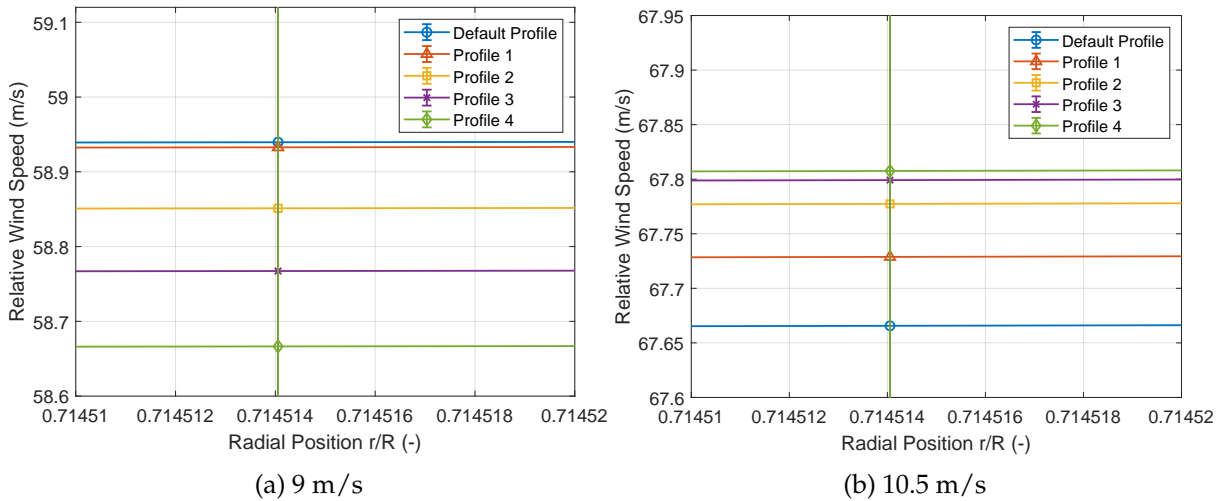


Figure 5.14: Variation of the relative wind speed of the original and the redesigned FOWT at the radial position of 0.715, according to the chord length increase profiles studied in this project for an average wind speeds of 9 m/s and 10.5 m/s. Blue curves: Original chord length profile. Orange curves: Chord length profile 1. Yellow curves: Chord length profile 2. Purple and Green curves: Chord length profiles 3 and 4 respectively.

wind speeds are likely to reduce the blade loading. The exact opposite probably occurs in the redesign wind speeds (10-12 m/s).

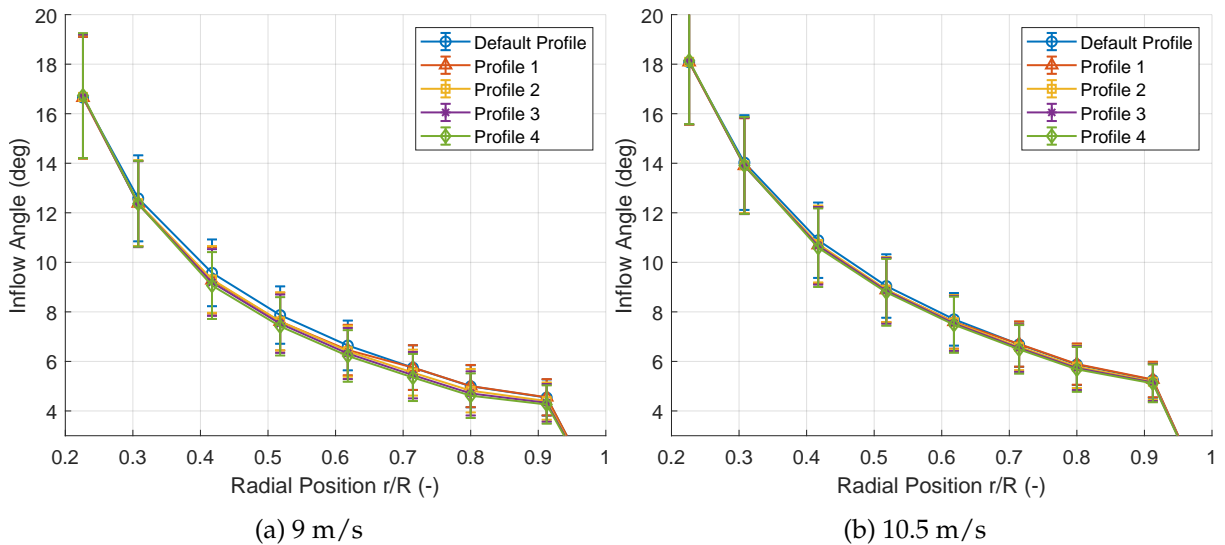


Figure 5.15: Variation of the spanwise inflow angles of the original and the redesigned FOWT, according to the chord length increase profiles studied in this project for an average wind speeds of 9 m/s and 10.5 m/s. Blue curves: Original chord length profile. Orange curves: Chord length profile 1. Yellow curves: Chord length profile 2. Purple and Green curves: Chord length profiles 3 and 4 respectively.

In addition, the variation of the spanwise AoA should be examined for the different chord length profiles in the peak shaver and in the pre-peak shaver wind speeds. As highlighted by Figures 5.18a and 5.18b, which show the AoA variation along the blade for average wind speeds of 9 m/s and 10.5 m/s respectively, airfoils with higher chord length are accompanied with a lower AoA. This observation is caused by the reduction in the inflow angle, which by definition (Eq. 4.4.2b) is associated with it. In addition, the anticipated higher blade loading due to the

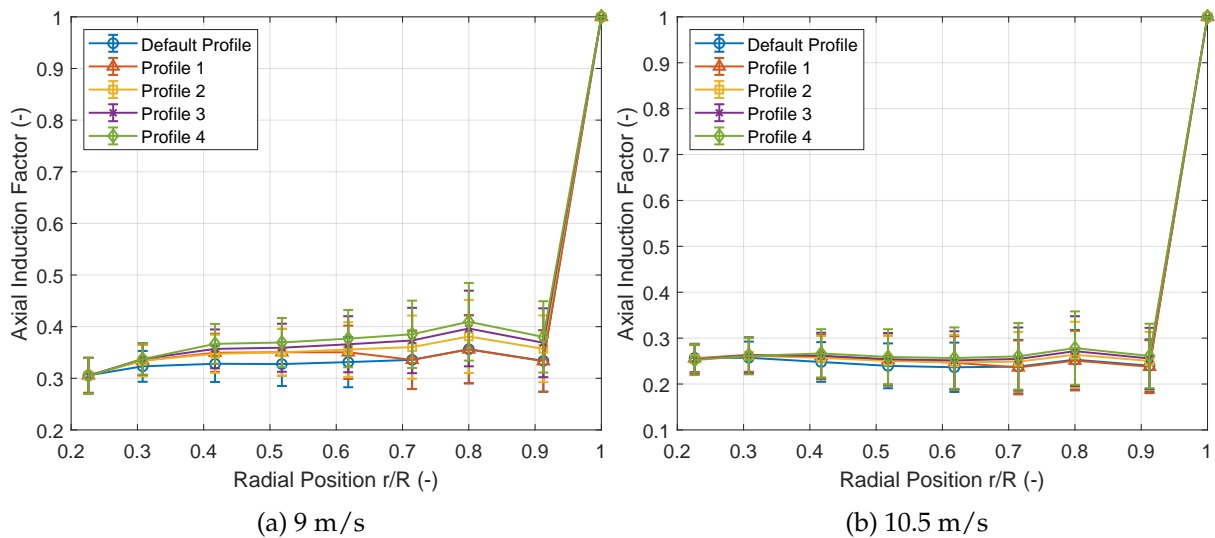


Figure 5.16: Variation of the spanwise axial induction factors of the original and the redesigned FOWT, according to the chord length increase profiles studied in this project for an average wind speeds of 9 m/s and 10.5 m/s. Blue curves: Original chord length profile. Orange curves: Chord length profile 1. Yellow curves: Chord length profile 2. Purple and Green curves: Chord length profiles 3 and 4 respectively.

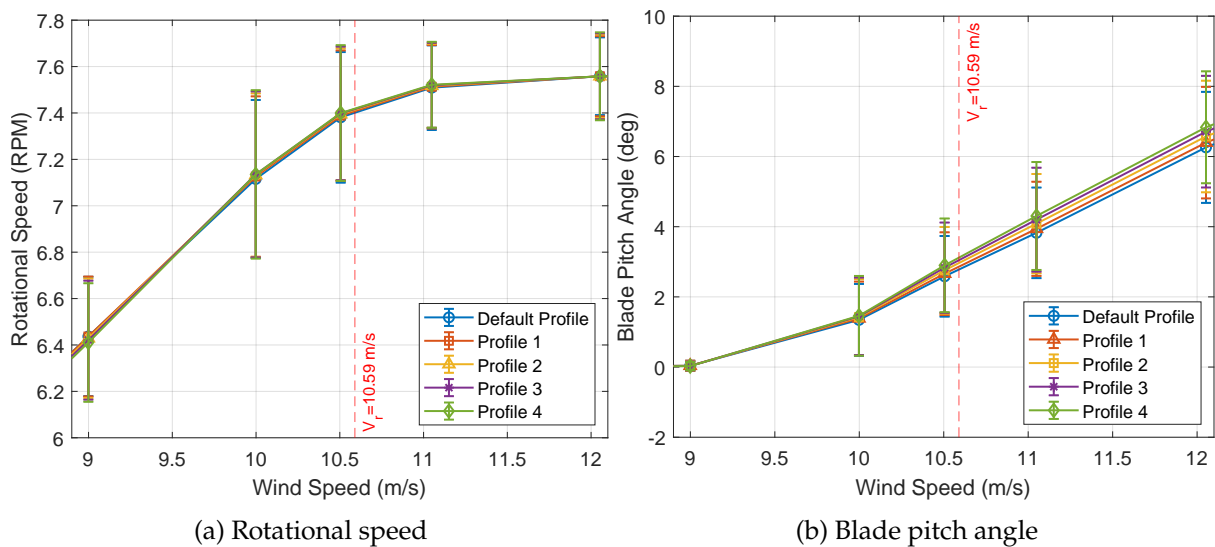


Figure 5.17: Variation of the rotational speed and blade pitch angle of the original and the redesigned FOWT, according to the chord length increase profiles studied in this project for average wind speeds between 9 and 12 m/s. Blue curves: Original chord length profile. Orange curves: Chord length profile 1. Yellow curves: Chord length profile 2. Purple and Green curves: Chord length profiles 3 and 4 respectively.

increase of the chord length and the resultant higher floater static pitch angles, lead to higher blade pitch angles set by the peak shaver (shown in Figure 5.17b), with a view of limiting the FOWT pitching movement. Consequently, the average blade pitch angle is higher as the chord length increases, thereby being one additional reason for the decrease of the AoA.

The reduction in AoA negatively affects the airfoils' aerodynamic performance due to the reduction of the C_L/C_D values along the blade span, with the exception of the outboard blade part ($r/R > 0.77$) up to 9 m/s. In this wind speed range, although the AoA reduces, it becomes

closer to its optimal value, which constitutes a lift to drag gain for these airfoils. Nevertheless, the decrease of the blade nodes' operating C_L/C_D values at all wind speeds reduces the aerodynamic efficiency of the airfoils, which, generate less lift than possible for nearly the same amount of drag. Thus, the right parenthesis terms in Eq. 4.4.3a and 4.4.3b decrease, a fact which impacts torque the most, due to its definition.

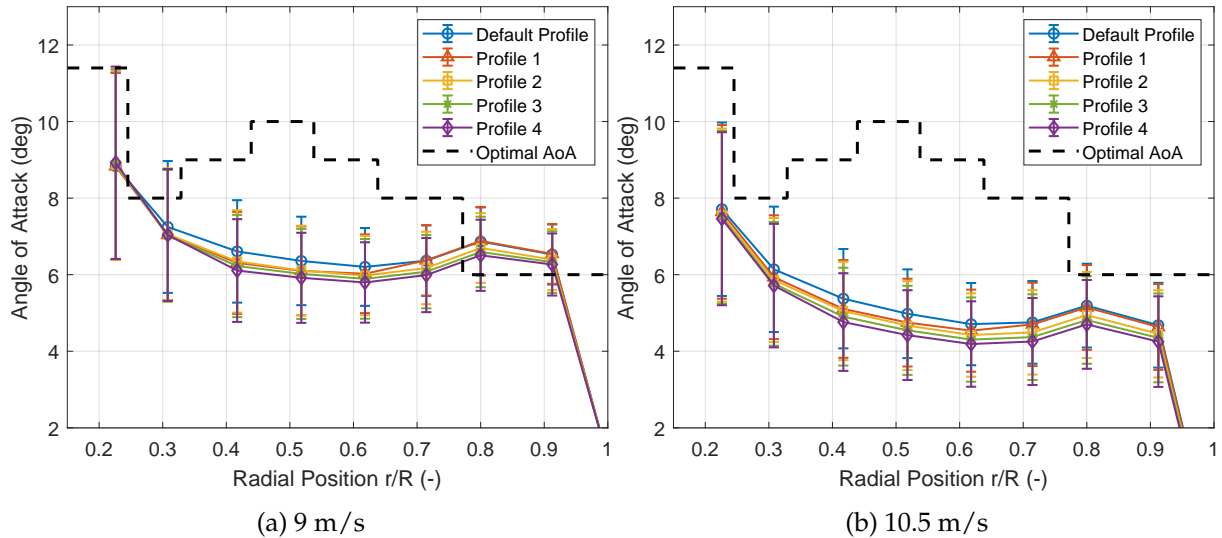


Figure 5.18: Spanwise angle of attack variation of the original and the redesigned FOWT, according to the chord length increase profiles studied in this project and for an average wind speeds of 9 and 10.5 m/s. Blue curves: Original chord length profile. Orange curves: Chord length profile 1. Yellow curves: Chord length profile 2. Purple and Green curves: Chord length profiles 3 and 4 respectively. Black dashed line: Spanwise optimal AoA.

Finally, the spanwise torque and thrust variations should be examined. However, this will be done for an average wind speed of 10.5 m/s, which is the basis of the aerodynamic redesign, but also for a wind speed in the pre-peak shaver region, i.e 9 m/s. Figures 5.19a and 5.19b show that for an average wind speed of 9 m/s, where there is less peak shaving, the increased chord length results in higher thrust but lower torque over the blade span. This paradoxical behavior is explained by the interplay of the parameters, which influence the spanwise thrust and torque per unit length. More specifically, in the case of thrust, although the spanwise relative wind speeds and the spanwise lift coefficients decrease, due to reasons explained in the previous analysis, the increase of the chord length outweighs the decrease of the aforementioned terms. Nevertheless, the exact opposite occurs for the spanwise torque, thereby reducing the power which can be extracted by the FOWT blades. At the same time, the FOWT out-of-plane loading is increased, leading to more power losses and to more frequent use of peak shaving.

On the contrary, as described by Figures 5.20a and 5.20b, at a wind speed of 10.5 m/s, the spanwise per unit torque increases due to the combined increase of the chord length, of the spanwise relative wind speeds and of the value of C_L/C_D . Same results are obtained for other wind speeds in the peak shaver region (10-12 m/s). Thus, the power of the FOWT is observed to increase. Yet, for all chord length redesign profiles, the per unit length spanwise thrust increase is even larger than the torque increase in comparison to the original FOWT. Hence, the static floater pitch of all redesign FOWT increases, which is inevitably causing more peak shaving effort by the controller.

Having all these in mind, it can be concluded that the FOWT aerodynamic redesign via increasing the spanwise airfoil chord length by 6% creates small torque gains in the peak shaver region, which increase the FOWT generator power. However, the increased airfoil chord length

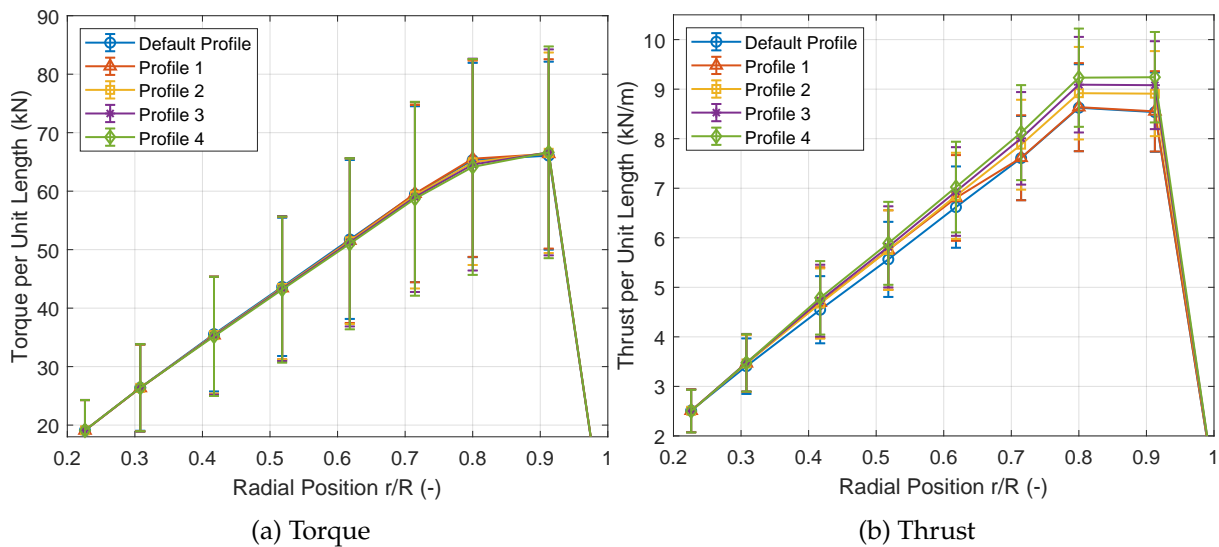


Figure 5.19: Spanwise variation of the per unit length torque and thrust of the original and the redesigned FOWT, according to the chord length increase profiles studied in this project and for an average wind speed of 9 m/s. Blue curves: Original chord length profile. Orange curves: Chord length profile 1. Yellow curves: Chord length profile 2. Purple and Green curves: Chord length profiles 3 and 4 respectively.

decreases the blade spanwise torque per unit length in case the peak shaver is not enabled, while generating large out-of-plane forces, which induce more blade pitching by the peak shaver. The airfoil performance is likely not to be optimized due to their operation at suboptimal AoA at all partial load wind speeds. These observations justify the reason why, although there are AEP gains from the redesign, those are smaller than those from the twist angle variation. Still, the AEP increase of the redesign FOWT compared to the original FOWT, which is at maximum 0.154% for the chord length profile 2, is inside the error margin of this project (0.5%). Therefore, as in the case of the blade twist profiles, the results of this study are deemed to be inconclusive.

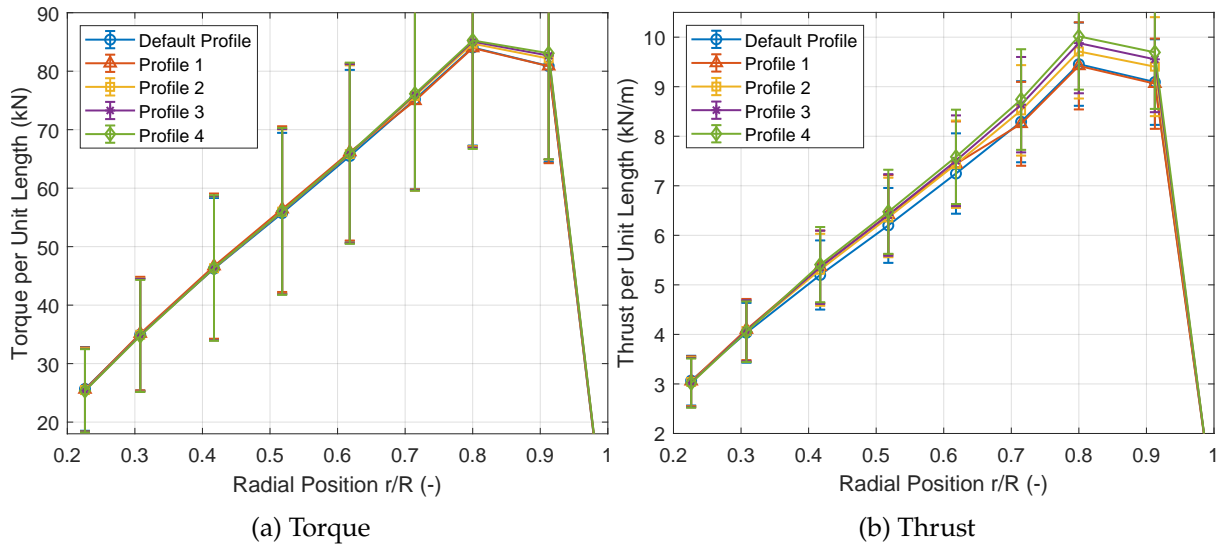


Figure 5.20: Spanwise variation of the per unit length torque and thrust of the original and the redesigned FOWT, according to the chord length increase profiles studied in this project and for an average wind speed of 10.5 m/s. Blue curves: Original chord length profile. Orange curves: Chord length profile 1. Yellow curves: Chord length profile 2. Purple and Green curves: Chord length profiles 3 and 4 respectively.

5.4 Section Twist Angle and Chord Length Variation

The final idea for the FOWT redesign is to perform a simultaneous blade twist and chord length redesign according to the respective redesign ideas, which resulted in the largest FOWT AEP increase, i.e. blade twist profile 2 and chord length profile 2. The combined blade twist and chord length FOWT redesign, as noted at Table 5.5, although it leads to a FOWT AEP gain, it is nearly 40% lower than the AEP increase achieved with twist angle profile 2, while being slightly lower than than of chord length profile 2. The aforementioned results can be explained by examining the power curves of the three redesign strategies between 9 and 12 m/s. Figure 5.21 depicts that the combination of the optimal blade twist and chord length profiles leads to larger power gains compared to the original FOWT design in the peak shaver region (10-12 m/s), but at the same time the FOWT power reduction tends to be larger in the pre-peak shaver region, as shown by the power comparison of all examined scenarios at 9 m/s. Same results are true for all wind speeds before the peak shaver is enabled.

Similar results are exhibited on the variation of the static floater pitch angle with the wind speed, as per Figure 5.22. Indeed, the combined redesign solution, since it has the dynamics of both blade twist and chord length solutions leads to the combination of the effects of the ideas, i.e. a larger static floater pitch angle at the whole examined wind speed range. It should be noted that, the static floater pitch angle is higher than 4° at 10 m/s and 10.5 m/s, which, as shown by the simulations, is attributed to very high spanwise aerodynamic thrust in these wind speeds, while the spanwise torque, albeit increased, it is not so much higher than the individual aerodynamic redesign scenarios. As a result, the wind speed deficit caused by the higher static floater pitch angles for the combined redesign scenario leads to even lower inflow wind speed values.

This is more profoundly expressed for wind speeds up to 9 m/s, where the peak shaver is mostly disabled. In addition, it is interesting to note that, for the blade twist angle and chord length aerodynamic redesign, the maximum static floater pitch angle is not constant between 10 and

Table 5.5: Comparison of the AEP, the AEP increase compared to the original FOWT and the AEP deficit compared to the BF wind turbine for the original FOWT and the redesigned FOWT, according to the blade twist profile 2, chord length profile 2 and the combination of the two profiles.

	Original FOWT	FOWT Twist Profile 2	FOWT Chord Profile 2	FOWT Chord and Twist Redesign
AEP (GWh)	60.341	60.488	60.433	60.431
AEP Increase Compared to Original FOWT (%)	–	0.244	0.154	0.150
FOWT AEP Decrease Compared to BF (%)	2.317	2.079	2.782	2.787

10.5 m/s, but is maximized at nearly 4.1° for a wind speed of 10 m/s. This, being in contrast with the observations for the original FOWT and the majority of the aerodynamic redesign scenarios, highlights that the minimum pitch angle imposed by the peak shaver for wind speeds near 10 m/s is inadequate to limit the static floater pitch angle. Therefore, this aerodynamic redesign analysis points out that, for aerodynamic redesigns causing a considerable increase in the thrust produced by the blades, the peak shaver should be redesigned, especially for the wind speed of 10 m/s. Finally, the variation of other aerodynamic performance parameters such as the inflow angles, the axial induction factors, the relative wind speeds, the AoA and the spanwise torque and thrust per unit length, is the expected from the combination of the two redesign efforts. Therefore, to avoid repetitions, they are presented in Appendix D of this work.

Last but not least, the results of this subsection suggest that, in case of a combined redesign of the blade twist angle and of the blade chord length, individual suboptimal solutions in terms of AEP should be examined. This stems from the fact that the individual AEP optimality leads to high FOWT loading, which is further exacerbated by the inclusion of both solutions into one aerodynamic redesign idea. Thus, a large amount of blade twist and chord length profiles should be tested via simulations, so as to highlight whether they can lead to optimality, when compared to individual blade twist and chord angle aerodynamic redesigns. However, as in the case of the blade twist angle and chord length redesign efforts, the AEP boost via a simultaneous blade twist and chord length redesign is within the AEP error margin selected for this project. Thus, as noted for the separate blade twist angle and chord length redesigns, it cannot be concluded for sure whether a combined redesign of the aforementioned two parameters can improve the FOWT AEP.

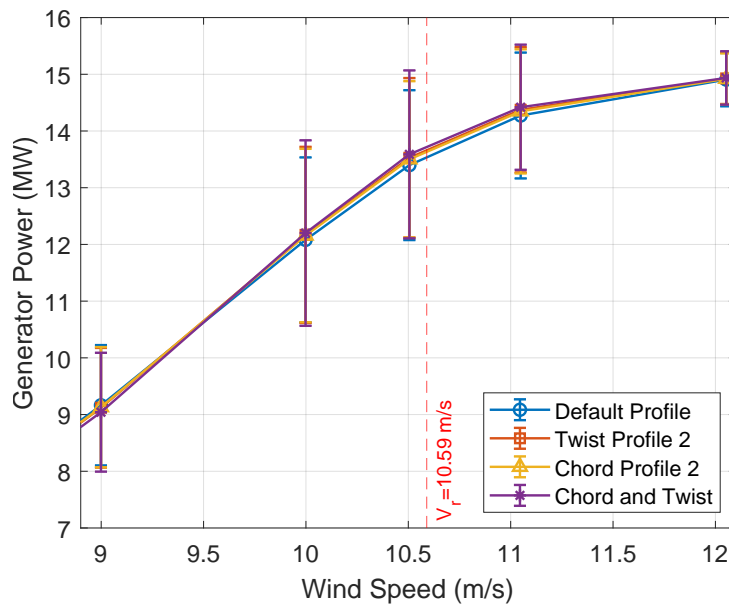


Figure 5.21: Power curves of the original and the redesigned FOWT, according to blade twist profile 2, chord length profile 2 and the combination of the two profiles, for wind speeds between 9 and 12 m/s . Blue curve: Power curve according to the original chord length profile, Orange curve: Power curve according to blade twist profile 2. Yellow curve: Power curve according to chord length profile 2. Purple line: Power curve according to the combination of the two profiles respectively.

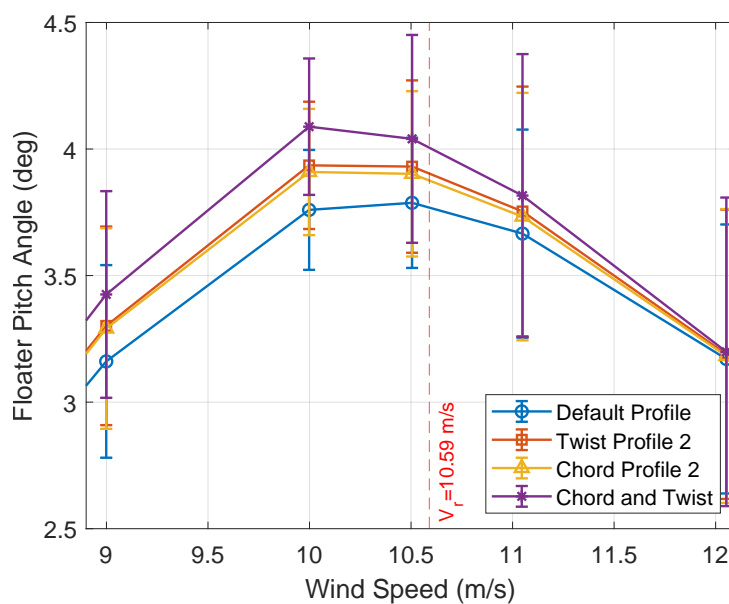


Figure 5.22: Static floater pitch angle variation of the original and the redesigned FOWT, according to blade twist profile 2, chord length profile 2 and the combination of the two profiles, for wind speeds between 9 and 12 m/s . Blue curve: Static floater pitch according to the original chord length profile, Orange curve: Static floater pitch according to blade twist profile 2. Yellow curve: Static floater pitch according to chord length profile 2. Purple line: Static floater pitch according to the combination of the two profiles respectively.

6 | Conclusions and Recommendations

The objective of this thesis project was to investigate whether FOWT for in situ hydrogen production should be aerodynamically redesigned in order to improve their performance compared to their BF counterparts. Also, a secondary target of the aerodynamic redesign was to compensate for possible power production losses due to the incorporation of the added mass of in situ hydrogen production plant on the floater. The first step in developing the methodology for answering the main research question of this project was to determine a baseline FOWT configuration and to provide an in situ plant qualitative and quantitative description via back-of-the-envelope calculations. Then, after determining a typical US East Coast site as the baseline geographical site for examining the turbines' behavior, OpenFAST was used to simulate the FOWT and BF turbines considered in this project. For this reason, various inputs were determined, while attention was given on the FOWT controller operation. In addition, the relative errors of the simulations were found to be lower than 5% at both steady and turbulent wind conditions. Finally, a simple methodology was developed so as to incorporate the added mass of the in situ hydrogen production in the FOWT model.

According to the obtained results, the non-zero static floater pitch angle led to power losses in the whole FOWT partial load region, because it tilted the FOWT against the wind field. Due to this action, the inflow wind speed seen by the rotor reduced. However, the results pointed out that a threshold static floater pitch angle value of 2° , existed, after which power losses started to considerably increase. In addition, the largest wind speed deficits occurred in the near rated region (10-12 m/s), where the static floater pitch angle had a maximum value of nearly 4° . Furthermore, as far as the in situ hydrogen plant is concerned, the simple approach of considering the hydrogen components as rectangular boxes, with their CoG being in the tower centerline, demonstrated that the in situ plant had a negligible effect on the FOWT performance. In fact, the mass and inertia increase were deemed to positively affect the FOWT performance by reducing the static floater pitch angles, especially in the rated region, due to a lower floater CoG. Therefore, much of the simulations and the aerodynamic redesign were done without considering the in situ hydrogen plant.

Nevertheless, the limitation of the turbine thrust via the peak shaving routine, was deemed to be the most significant contributor to FOWT power losses compared to the BF turbine in turbulent wind conditions. More specifically, although up to rated power, the FOWT experienced power losses due to the static floater pitch angle, from 10 m/s to 12 m/s, the FOWT losses were mainly dominated by the peak shaving. Thus, the combination of the peak shaver and the static floater pitch angle significantly hampered the power generation of the FOWT against the BF turbine in the near rated region and increased the FOWT rated power to 14 m/s in turbulent wind, instead of 10.59 m/s, in the case of the BF turbine.

In addition, the turbulent wind simulations showed that, the increased blade pitching action at near rated wind speed, contributed to maximizing the power loss for the wind speed of 10.5 m/s. For this wind speed, the spanwise AoA of the FOWT was nearly 1° lower than that of the BF, while a 6% blade spanwise aerodynamic torque reduction was also observed. Thus, to answer the main research question, an aerodynamic redesign of the FOWT should be done

and should target the wind speed of 10.5 m/s as well as the peak shaver wind speeds (10-12 m/s). Aligned with this decision, the redesigned solutions that were easy to implement for this project were the reduction of the spanwise blade twist angle, the increase of the blade chord length and the simultaneous application of both changes.

As far as the section twist angle is concerned, from all examined blade twist profiles, a reduction of the twist angle by nearly 1° in the inboard and midboard blade parts, followed by an 0.5° decrease towards the tip was proven to guarantee the largest AEP gain compared to the original FOWT. This is indicated by a gain in airfoils' aerodynamic efficiency due to their operation near their optimal AoA, while at the same time the relative wind speed seen by the blades increased. Both changes resulted in a spanwise blade torque and thrust gain, whose ratio was higher than other solutions, effectively leading to power gains. Moreover, the simulations provided evidence that the conservative spanwise chord length increase of 6%, was the best solutions amongst those tested in this project.

Yet, the increase of the chord length of the blade airfoils' resulted in sheer force gains, which not only contributed to excessive blade loading, but also caused inefficient operation of the airfoils. Moreover, a two-factor aerodynamic redesign should not involve the individual optimal blade twist and chord length solutions, since they contributed to excessive blade loading. Last but not least, the simulation results hinted that any effort to improve the FOWT performance between 10 and 12 m/s, where peak shaving occurred, proved detrimental for its performance between 6 and 9 m/s, due to the increased static floater pitch. Hence, the AEP gain was strongly influenced by whether the peak shaver region gains outweighed the pre-peak shaver region losses.

It should be noted that, the AEP increase percentage of the redesign solutions compared to the original FOWT was at maximum 0.244% for the case of the optimal twist angle profile. At the same time, the most optimal chord length redesign profile and the simultaneous alteration of both blade twist and chord length resulted in an AEP gain, which was approximately 40% lower than the one obtained according for the optimal twist angle profile. Yet, all AEP gains of the proposed redesign solutions were found to be inside the 0.5% AEP error margin considered in this project. This signifies that it cannot be concluded whether they indeed improved the performance of the FOWT against its original design. This observation is possibly a result of the low fidelity simulation nature of OpenFAST. Also, during the project, simplifications and assumptions were made, which may hinder the accuracy of the obtained results. Therefore, the creation of AEP gains via an aerodynamic redesign of the IEA 15 MW RWT on the UMaine semi-submersible floater should be examined in more depth, using high fidelity simulation tools such as computational fluid dynamics software packages.

Another issue observed from the simulations is that, due to high computational effort, only four profiles were tested for each redesign idea. Therefore, it is likely possible that, although the profiles provided useful conclusions about the aerodynamic redesign choices, other profiles may result in even larger AEP and performance gains. This is also true for the two-parameter redesign, where individual suboptimal solutions possibly lead to the generally optimal solution. Hence, the computer cluster of TU Delft should be used in order to simultaneously simulate a large number of twist angle, chord length and combined profiles, as well as to optimise the airfoil position over the blades, in order to pinpoint the most optimal redesign solutions.

In addition, as shown by the AoA variation along the blade span, sometimes, the operational AoA was no near the optimal AoA of the specific airfoil, especially in the peak shaver region. Thus, it is recommended that existing airfoils should be improved or new airfoils should be designed, with the view to being more compatible with peak shavers. More specifically, airfoils with higher C_L/C_D over a wide range of AoA should be designed for use with peak shavers. In

this way, not only the aerodynamic efficiency of the airfoils will be boosted, but also it will be kept more or less constant when blade pitching due to peak shaving is used.

Last but not least, in order to improve the FOWT performance, in addition to the aerodynamic redesign, a structural redesign can be performed as well. This may target the rotor itself i.e. by refining the blade stiffness, or the platform and its mooring lines. For example, the tension of one or more mooring lines can be increased so as to limit to some extent the static floater pitch angle. However, if a structural redesign is undertaken, then an investigation of ultimate and fatigue loading analyses should be performed using design load cases (DLC) according to IEC/TS 61400-3-2. However, DLC testing should also be conducted for the aerodynamic redesign as well. This stems from the fact that the increased turbine loading occurring at all aerodynamic redesign scenarios may be detrimental for various components like the hub, the blades and the mooring lines. Finally, as a recommendation for further work, the aerodynamic redesign investigation, conducted in this project, can be expanded to other floaters such as the spar buoy and the TLP, which are commonly used as FOWT platforms, in addition to semi-sub floaters.

References

- [1] IPCC. "Proposed outline of the special report in 2018 on the impacts of global warming of 1.5 °C above pre-industrial levels and related global greenhouse gas emission pathways , in the context of strengthening the global response to the threat of climate cha". In: *Ippc - Sr15* 2.October (2018), pp. 17–20. URL: www.environmentalgraphiti.org.
- [2] IRENA. *Green Hydrogen Cost Reduction*. 2020, p. 105. ISBN: 9789292602956. URL: [/publications/2020/Dec/Green-hydrogen-cost-reduction%0Ahttps://www.irena.org/-/media/Files/IRENA/Agency/Publication/2020/Dec/IRENA_Green_hydrogen_cost_2020.pdf](https://publications/2020/Dec/Green-hydrogen-cost-reduction%0Ahttps://www.irena.org/-/media/Files/IRENA/Agency/Publication/2020/Dec/IRENA_Green_hydrogen_cost_2020.pdf).
- [3] IRENA. *World energy transitions outlook: 1.5 degrees pathway*. 2021, pp. 1–54. ISBN: 9789292603342. URL: <https://irena.org/publications/2021/March/World-Energy-Transitions-Outlook>.
- [4] European Commission. "REPowerEU : Joint European action for more affordable , secure and sustainable energy". In: March (2022). DOI: 10.2775/31911.
- [5] Fuel Cells and Hydrogen Joint Undertaking (FCH). *Hydrogen Roadmap Europe*. 2019, p. 70. ISBN: 9789292463328. DOI: 10.2843/249013. URL: fch.europa.eu.
- [6] IEA. "Net Zero by 2050: A Roadmap for the Global Energy Sector". In: *International Energy Agency* (2021), p. 224.
- [7] David Caine et al. *Dolphyn Hydrogen | Phase 1- Final Report*. Tech. rep. October. Department for Business Energy and Industrial Strategy, 2019.
- [8] European Commision. "A hydrogen strategy for a climate-neutral Europe". In: (2020), pp. 5–24.
- [9] L Collins. *Ukraine war | Green hydrogen 'now cheaper than grey in Europe, Middle East and China': BNEF*. 2022. URL: <https://www.rechargenews.com/energy-transition/ukraine-war-green-hydrogen-now-cheaper-than-grey-in-europe-middle-east-and-china-bnef/2-1-1180320>.
- [10] Blake Matich. *Invasion of Ukraine an inadvertent boost for green hydrogen*. 2022. URL: <https://www.pv-magazine.com/2022/03/21/invasion-of-ukraine-an-inadvertent-boost-for-green-hydrogen/>.
- [11] Omar S. Ibrahim et al. "Dedicated large-scale floating offshore wind to hydrogen: Assessing design variables in proposed typologies". In: *Renewable and Sustainable Energy Reviews* 160.November 2021 (2022), p. 112310. ISSN: 13640321. DOI: 10.1016/j.rser.2022.112310. URL: <https://doi.org/10.1016/j.rser.2022.112310>.
- [12] IEA. "Offshore Wind Outlook 2019". In: (2019). URL: <https://www.iea.org/reports/africa-energy-outlook-2019>.
- [13] Kelly Eurek et al. "An improved global wind resource estimate for integrated assessment models". In: *Energy Economics* 64 (May 2017), pp. 552–567. ISSN: 0140-9883. DOI: 10.1016/J.ENECO.2016.11.015.
- [14] Musial Walter et al. "Offshore Wind Market Report: 2021 Edition". In: *Department of Energy* (2021). URL: <https://www.energy.gov/eere/wind/articles/offshore-wind-market-report-2021-edition-released>.

- [15] IRENA. *Future of Wind: Deployment, investment, technology, grid integration and socio-economic aspects*. 2019, pp. 1–88. ISBN: 9789292601553. URL: https://www.irena.org/-/media/Files/IRENA/Agency/Publication/2019/Oct/IRENA_Future_of_wind_2019.pdf.
- [16] Equinor. *Hywind Scotland remains the UKs best performing offshore wind farm*. 2021. URL: <https://www.equinor.com/en/news/20210323-hywind-scotland-uk-best-performing-offshore-wind-farm.html>.
- [17] Angeliki Spyroudi et al. “Offshore Wind and Hydrogen: Solving the Integration Challenge”. In: (2020), p. 87.
- [18] A Robertson et al. “Definition of the Semisubmersible Floating System for Phase II of OC4 Definition of the Semisubmersible Floating System for Phase II of OC4”. In: September (2014).
- [19] Zhixin Zhao et al. “Dynamic analysis of a novel semi-submersible platform for a 10 MW wind turbine in intermediate water depth”. In: *Ocean Engineering* 237.May (2021), p. 109688. ISSN: 00298018. DOI: 10.1016/j.oceaneng.2021.109688. URL: <https://doi.org/10.1016/j.oceaneng.2021.109688>.
- [20] Thomas P Mazarakos, Theodosios D Tsaousis, and Spyros A Mavrakos. “Analytical Investigation of Tension Loads Acting on a TLP Floating Wind Turbine”. In: (2022).
- [21] Mohammad Youssef Mahfouz et al. “CoreWind - D1.3 Public design and FAST models of the two 15MW floater-turbine concepts”. In: April (2020).
- [22] International Electrotechnical Commission. *IEC 61400-3. Wind turbines – Part 3: Design requirements for offshore wind turbines*. Tech. rep. 2009, pp. 1–11.
- [23] Gonçalo Calado and Rui Castro. “Hydrogen Production from Offshore Wind Parks : Current Situation and Future Perspectives”. In: (2021).
- [24] N. Barberis Negra, J. Todorovic, and T. Ackermann. “Loss evaluation of HVAC and HVDC transmission solutions for large offshore wind farms”. In: *Electric Power Systems Research* 76.11 (July 2006), pp. 916–927. ISSN: 0378-7796. DOI: 10.1016/J.EPSR.2005.11.004.
- [25] A Papadopoulos et al. “Collection and transmission losses of offshore wind farms for optimization purposes”. In: *2015 IEEE Energy Conversion Congress and Exposition (ECCE)*. 2015, pp. 6724–6732. DOI: 10.1109/ECCE.2015.7310601.
- [26] Abdulrahman Alassi et al. “HVDC Transmission: Technology Review, Market Trends and Future Outlook”. In: *Renewable and Sustainable Energy Reviews* 112 (Sept. 2019), pp. 530–554. ISSN: 1364-0321. DOI: 10.1016/J.RSER.2019.04.062.
- [27] Sofia G. Simoes et al. “Water availability and water usage solutions for electrolysis in hydrogen production”. In: *Journal of Cleaner Production* 315 (Sept. 2021), p. 128124. ISSN: 0959-6526. DOI: 10.1016/J.JCLEPRO.2021.128124.
- [28] European Commission. *The hydrogen strategy for a climate-neutral Europe*. Tech. rep. 2020, pp. 1–24.
- [29] Bin Miao, Lorenzo Giordano, and Siew Hwa Chan. “Long-distance renewable hydrogen transmission via cables and pipelines”. In: *International Journal of Hydrogen Energy* 46.36 (May 2021), pp. 18699–18718. ISSN: 0360-3199. DOI: 10.1016/J.IJHYDENE.2021.03.067.
- [30] Konrad Meier. “Hydrogen production with sea water electrolysis using Norwegian offshore wind energy potentials: Techno-economic assessment for an offshore-based hydrogen production approach with state-of-the-art technology”. In: *International Journal of Energy and Environmental Engineering* 5.2-3 (2014), pp. 1–12. ISSN: 22516832. DOI: 10.1007/s40095-014-0104-6.

- [31] Catrinus Jepma and Miralda Van Schot. "On the economics of offshore energy conversion: smart combinations_Converting offshore wind energy into green hydrogen on existing oil and gas platforms in the North Sea". In: *Energy Delta Institute* February (2017), pp. 1–54. URL: <https://www.gasmeetswind.eu/wp-content/uploads/2017/05/EDI-North-Sea-smart-combinations-final-report-2017.pdf>.
- [32] Patrick K. S. Ayivor. "Feasibility Of Demand Side Response From Electrolysers To Support Power System Stability". Doctoral dissertation. TU Delft, 2018. URL: <http://repository.tudelft.nl/>.
- [33] Yujing Guo et al. "Comparison between hydrogen production by alkaline water electrolysis and hydrogen production by PEM electrolysis". In: *IOP Conference Series: Earth and Environmental Science* 371.4 (2019). ISSN: 17551315. DOI: 10.1088/1755-1315/371/4/042022.
- [34] Jawad Mustafa et al. "Simultaneous treatment of reject brine and capture of carbon dioxide: A comprehensive review". In: *Desalination* 483.March (2020), p. 114386. ISSN: 00119164. DOI: 10.1016/j.desal.2020.114386. URL: <https://doi.org/10.1016/j.desal.2020.114386>.
- [35] Maha Mehanna et al. "Microbial electro dialysis cell for simultaneous water desalination and hydrogen gas production". In: *Environmental Science and Technology* 44.24 (2010), pp. 9578–9583. ISSN: 0013936X. DOI: 10.1021/es1025646.
- [36] Tamim Younos and Kimberly E Tulou. "Overview of Desalination Techniques". In: (2005).
- [37] Néstor González Díez et al. "Technical assessment of Hydrogen transport, compression, processing offshore". In: *North Sea Energy* (2020).
- [38] Nick Carter et al. "Flexibility of Hydrogen Electrolysers Opportunities in the Australian National Electricity Market". In: October (2020).
- [39] Charles A. Miller. "Risers Introduction". In: *Encyclopedia of Maritime and Offshore Engineering* (2017), pp. 1–11. DOI: 10.1002/9781118476406.emoe485.
- [40] Srinivasan Chandrasekaran. "Marine risers : Introduction". In: *Design of Marine Risers with Functionally Graded Materials*. 2021, pp. 1–23. ISBN: 9780128235379. DOI: 10.1016/B978-0-12-823537-9.00006-2.
- [41] A. Pacheco et al. "An evaluation of offshore wind power production by floatable systems: A case study from SW Portugal". In: *Energy* 131 (2017), pp. 239–250. ISSN: 03605442. DOI: 10.1016/j.energy.2017.04.149.
- [42] NREL. *NREL Market Report Finds U.S. Offshore Wind Industry Poised for Multigigawatt Surge*. 2017. URL: <https://www.nrel.gov/news/program/2017/nrel-market-report-finds-us-offshore-wind-industry-poised-multigigawatt-surge.html>.
- [43] International Renewable Energy Agency (IRENA). "Floating Foundations: A Game Changer for Offshore Wind Power". In: (2016), pp. 1–8. URL: http://www.irena.org/-/media/Files/IRENA/Agency/Publication/2016/IRENA_Offshore_Wind_Floating_Foundations_2016.pdf.
- [44] Peter Nico Veldman. "Essentials in Coupled Dynamics of Floating Offshore Wind Turbines". Doctoral dissertation. TU Delft, 2020. URL: <http://repository.tudelft.nl/>.
- [45] EDP. *WindFloat Atlantic-Floating offshore wind-power generating platform*. 2021. URL: <https://www.edp.com/pt-pt/windfloat>.
- [46] Evan Gaertner et al. "Definition of the IEA Wind 15-Megawatt Offshore Reference Wind Turbine -Technical Report". In: *National Renewable Energy Laboratory. NREL/TP-5000-75698* (2020). URL: <https://www.nrel.gov/docs/fy20osti/75698.pdf>.

- [47] Christopher Allen et al. "Definition of the UMaine VoltturnUS-S Reference Platform Developed for the IEA Wind 15-Megawatt Offshore Reference Wind Turbine". In: (2020), pp. 1–41.
- [48] Mehdi Jafari, Audun Botterud, and Apurba Sakti. "Estimating revenues from offshore wind-storage systems: The importance of advanced battery models". In: *Applied Energy* 276 (Oct. 2020), p. 115417. ISSN: 0306-2619. DOI: 10.1016/J.APENERGY.2020.115417.
- [49] Siemens Energy NEB. "Overview of the PEM Silyzer Family". In: (2020), pp. 12–27.
- [50] Culligan. *Culligan IW EVO Series Reverse Osmosis Desalination Specifications*. Tech. rep. 2021.
- [51] BEDU Pompen. *BEDU Pompen 3(L) M Series Centrifugal Pump Specification*. Tech. rep. 2018.
- [52] W F Breunis. "Hydrogen gas production from offshore wind energy". In: (2021).
- [53] Philip Thomas. "Turbo pumps and compressors". In: *Simulation of Industrial Processes for Control Engineers* (Jan. 1999), pp. 204–220. DOI: 10.1016/B978-075064161-6/50018-3.
- [54] J M Campbell. *Gas Conditioning and Processing: The equipment modules*. Gas Conditioning and Processing. Campbell Petroleum Series, 1984. URL: <https://books.google.nl/books?id=IJhQAQAIAAJ>.
- [55] ABB. *ABB to deliver power converters for the worlds largest offshore wind farm*. 2021. URL: <https://new.abb.com/news/detail/79198/abb-to-deliver-power-converters-for-the-worlds-largest-offshore-wind-farm>.
- [56] ABB. "ABB wind turbine converters PCS6000, full power converter, up to 12 MW". In: (2019), p. 12.
- [57] R. F. P. Bentvelsen. "Modeling and Scheduling of a Controllable Electrolyser in an Industrial Grid". In: (2019), p. 116.
- [58] Tesla. *Introducing Megapack: Utility-Scale Energy Storage*. 2019. URL: <https://www.tesla.com/blog/introducing-megapack-utility-scale-energy-storage>.
- [59] J M Jonkman. "Dynamics Modeling and Loads Analysis of an Offshore Floating Wind Turbine Dynamics Modeling and Loads Analysis of an Offshore Floating Wind Turbine". In: November (2007).
- [60] J.F. Manwell, J.G. McGowan, and A.L. Rogers. "Wind Turbine Design". In: *Wind Energy Explained* (2003), pp. 247–320. DOI: 10.1002/0470846127.ch6.
- [61] Kelsey Shaler, Emmanuel Branlard, and Andy Platt. "OLAF User's Guide and Theory Manual OLAF User's Guide and Theory Manual". In: June (2020).
- [62] J R Morison, J W Johnson, and S A Schaaf. "The Force Exerted by Surface Waves on Piles". In: *Journal of Petroleum Technology* 2.05 (May 1950), pp. 149–154. ISSN: 0149-2136. DOI: 10.2118/950149-G. URL: <https://doi.org/10.2118/950149-G>.
- [63] W E Cummins, DAVID TAYLOR MODEL BASIN WASHINGTON D C., and David W Taylor Model Basin. *The Impulse Response Function and Ship Motions*. Report (David W. Taylor Model Basin). Navy Department, David Taylor Model Basin, 1962. URL: <https://books.google.nl/books?id=GLLANwAACAAJ>.
- [64] Michael Borg and Maurizio Collu. "Offshore floating vertical axis wind turbines, dynamics modelling state of the art. Part III : Hydrodynamics and coupled modelling approaches". In: 46 (2015), pp. 296–310. DOI: 10.1016/j.rser.2014.10.100.
- [65] NREL. "OpenFAST Documentation Release v3.0.0". In: (2021), pp. 1–101. URL: <https://openfast.readthedocs.io/en/latest/index.html>.
- [66] International Electrotechnical Commission. *Wind Energy Generation Systems - Part 1: Design Requirements (IEC 61400-1:2019)*. Tech. rep. 2019.

- [67] G. Stewart et al. "Assessing fatigue and ultimate load uncertainty in floating offshore wind turbines due to varying simulation length". In: *Safety, Reliability, Risk and Life-Cycle Performance of Structures and Infrastructures - Proceedings of the 11th International Conference on Structural Safety and Reliability, ICOSSAR 2013 July* (2013), pp. 239–246. DOI: 10.1201/b16387-33.
- [68] Lorenz Haid et al. "Simulation-Length requirements in the loads analysis of offshore floating wind turbines". In: *Proceedings of the International Conference on Offshore Mechanics and Arctic Engineering - OMAE 8*. June (2013). DOI: 10.1115/OMAE2013-11397.
- [69] Jakob Mann. "Wind field simulation". In: *Probabilistic Engineering Mechanics* 13.4 (Oct. 1998), pp. 269–282. ISSN: 0266-8920. DOI: 10.1016/S0266-8920(97)00036-2.
- [70] International Electrotechnical Commission. *NVN-IEC / TS 61400-3-2.-Wind energy generation systems - Part 3-2: Design requirements for floating offshore wind turbines*. Tech. rep. 2019.
- [71] Michiel Zaayer and Axelle Vire. "Introduction to wind turbines: physics and technology". 2018.
- [72] Gordon M Stewart et al. "The creation of a comprehensive metocean data set for offshore wind turbine simulations". In: *Wind Energy* 19.6 (2016), pp. 1151–1159. DOI: <https://doi.org/10.1002/we.1881>. URL: <https://onlinelibrary.wiley.com/doi/abs/10.1002/we.1881>.
- [73] Lucie Barj et al. "Wind/wave misalignment in the loads analysis of a floating offshore wind turbine". In: *32nd ASME Wind Energy Symposium* February (2014). DOI: 10.2514/6.2014-0363.
- [74] Ingunn Sletvold Øistad. "Analysis of the Turbulence Intensity at Skipheia Measurement Station". Doctoral dissertation. NTNU, 2015. URL: <http://hdl.handle.net/11250/2454949>.
- [75] N. Bodini, J. K. Lundquist, and A. Kirincich. "Offshore Wind Turbines Will Encounter Very Low Atmospheric Turbulence". In: *Journal of Physics: Conference Series* 1452.1 (2020), pp. 1–7. ISSN: 17426596. DOI: 10.1088/1742-6596/1452/1/012023.
- [76] Kurt S. Hansen et al. "The impact of turbulence intensity and atmospheric stability on power deficits due to wind turbine wakes at Horns Rev wind farm". In: *Wind Energy* 15.1 (2012), pp. 183–196. DOI: 10.1002/we.512.
- [77] Jason M. Jonkman. "Influence of control on the pitch damping of a floating wind turbine". In: *46th AIAA Aerospace Sciences Meeting and Exhibit* March (2008). DOI: 10.2514/6.2008-1306.
- [78] Nikhar J. Abbas et al. "A reference open-source controller for fixed and floating offshore wind turbines". In: *Wind Energy Science* 7.1 (2022), pp. 53–73. ISSN: 23667451. DOI: 10.5194/wes-7-53-2022.
- [79] J Jonkman. "Definition of the Floating System for Phase IV of OC3". In: 1.May (2010), p. 31. URL: <http://scholar.google.com/scholar?hl=en&btnG=Search&q=intitle:Definition+of+the+Floating+System+for+Phase+IV+of+OC3#0>.
- [80] Xin Shen, Xiaocheng Zhu, and Zhaohui Du. "Wind turbine aerodynamics and loads control in wind shear flow". In: *Energy* 36.3 (2011), pp. 1424–1434. ISSN: 03605442. DOI: 10.1016/j.energy.2011.01.028. URL: <http://dx.doi.org/10.1016/j.energy.2011.01.028>.
- [81] K Chaviaropoulos. "Similarity rules for W/T up-scaling". In: *UpWind Report, WP 1B4* (2007), pp. 1–8.

A | ElastoDyn Inputs for Blade Twist Angle Profiles

A.1 Elastodyn Inputs for Twist Angle Profile #1

Table A.1: ElastoDyn OpenFAST input data for twist angle profile #1.

Blade Fraction r/R (-)	Twist Angle (deg)	Chord Length (m)	Mass Density (kg/m)	Flapwise Stiffness (Nm ²)	Edgewise Stiffness (Nm ²)
0.000000000000000E+00	1.559455301971170E+01	5.200000000000000E+00	3.179059159259060E+03	1.525336732671640E+11	1.524092444021610E+11
2.000000000000000E-02	1.559105026258910E+01	5.208280051053220E+00	2.844639124071310E+03	1.396059559125450E+11	1.371910901056170E+11
4.000000000000000E-02	1.542808288705690E+01	5.235714686841760E+00	2.505353762822230E+03	1.239755438005000E+11	1.211943594444680E+11
6.000000000000000E-02	1.498668187913840E+01	5.288938619667070E+00	2.150176072709730E+03	1.032257195889790E+11	1.030637624551030E+11
8.000000000000000E-02	1.432158034416250E+01	5.360587950371890E+00	1.807166613880170E+03	8.162835042138820E+10	8.436578661171380E+10
1.000000000000000E-01	1.348751138745820E+01	5.443298779798940E+00	1.689750275067180E+03	6.177531809788480E+10	6.862655814157260E+10
1.250000000000000E-01	1.229069721992210E+01	5.551024109038490E+00	1.296524292073250E+03	4.274720146392410E+10	5.134664996974550E+10
1.500000000000000E-01	1.102229252935760E+01	5.650144322056730E+00	9.822677239823060E+02	3.237301609568750E+10	3.898538145499410E+10
1.690340633511320E-01	1.007455100521850E+01	5.710964180985910E+00	7.966163346309950E+02	2.827287353472030E+10	3.195263357170140E+10
1.880681267022640E-01	9.194457415112660E+00	5.752111033293940E+00	6.645041811187670E+02	2.481852933449630E+10	2.695846118026080E+10
2.071021900533960E-01	8.429191400183100E+00	5.767237237684650E+00	5.764843213881020E+02	2.195610441457930E+10	2.376092222912670E+10
2.261362534045280E-01	7.777140178454870E+00	5.754540379641520E+00	5.250180685658330E+02	1.967142143571740E+10	2.208465213113590E+10
2.451703167556600E-01	7.182453068336750E+00	5.702616552569120E+00	4.925364059605150E+02	1.805224163293000E+10	2.106608767500110E+10
2.660887252285560E-01	6.526991264456790E+00	5.600650141179930E+00	4.671178249482400E+02	1.671838806704950E+10	2.035217171041800E+10
2.870071337014520E-01	5.530059716904850E+00	5.463153391746180E+00	4.526892330366370E+02	1.545040426884080E+10	1.996217848145590E+10
3.079255421743470E-01	4.785284799548210E+00	5.309456651571880E+00	4.478982718495180E+02	1.425262350769260E+10	1.971283876391980E+10
3.288439506472430E-01	4.103871106220670E+00	5.148771194775270E+00	4.434501720049930E+02	1.301246687693210E+10	1.913520606370910E+10
3.509110298069780E-01	3.450590793395070E+00	4.991052530953460E+00	4.383992071132160E+02	1.177142473319300E+10	1.830911869625890E+10
3.729781089667120E-01	2.861347589363740E+00	4.849825861125230E+00	4.303870023258640E+02	1.063075751402770E+10	1.726648597667800E+10
3.950451881264470E-01	2.332818123937610E+00	4.727623031975450E+00	4.199515443050740E+02	9.612894282647330E+09	1.605865945507700E+10
4.171122672861810E-01	1.861679026927760E+00	4.604744127582390E+00	4.077257161686330E+02	8.632215309868140E+09	1.470313795543420E+10
4.391793464459160E-01	1.444606928145140E+00	4.482053325831180E+00	3.924438241159640E+02	7.670161976417180E+09	1.306446466642580E+10
4.588777585784190E-01	1.115269316855070E+00	4.373759436309790E+00	3.781497498899630E+02	6.850238547683750E+09	1.161760885274030E+10
4.785761707109230E-01	8.240024602415340E-01	4.267298674782820E+00	3.635693457624110E+02	6.080518723471740E+09	1.023131799902930E+10
4.982745828434270E-01	5.684424108450440E-01	4.162982209701330E+00	3.49215062433850E+02	5.377222884634280E+09	8.957222703042520E+09
5.179729949759310E-01	3.462252212060900E-01	4.061706722205010E+00	3.360065859722420E+02	4.753629978034940E+09	7.881195883717870E+09
5.376714071084350E-01	1.549869438651680E-01	3.963536198880920E+00	3.236134228528660E+02	4.208216667668420E+09	6.945396072547720E+09
5.57786570700220E-01	-1.072534724028530E-02	3.866942578335680E+00	3.111722310592850E+02	3.718761715312920E+09	6.048539773187990E+09
5.778859070316100E-01	-1.491367616164960E-01	3.773008482150570E+00	2.987202701527960E+02	3.278832254292590E+09	5.213943536606200E+09
5.979931569931980E-01	-2.627615129814840E-01	3.681310369877000E+00	2.861632387471790E+02	2.885527839847520E+09	4.436841796990030E+09
6.181004069547860E-01	-3.541138150532750E-01	3.590736963146060E+00	2.737130089608080E+02	2.533674784416490E+09	3.759425782667440E+09
6.382076569163730E-01	-4.257078815498900E-01	3.500781512082170E+00	2.614646456667160E+02	2.220537999215230E+09	3.191905368536750E+09
6.572842562528320E-01	-4.776516499168790E-01	3.415119535682270E+00	2.500840447242680E+02	1.944279119832140E+09	2.760285285665830E+09
6.763608555892900E-01	-6.200000000000000E-01	3.328844727050610E+00	2.388570448427700E+02	1.679737195885030E+09	2.455134058468400E+09
6.954374549257480E-01	-7.252875829492340E-01	3.241551330883460E+00	2.271577540416740E+02	1.433783698230150E+09	2.232548383641040E+09
7.145140542622060E-01	-9.835362560574680E-01	3.155076129554680E+00	2.131533971390730E+02	1.206419926990950E+09	2.024234582445270E+09
7.335906535986650E-01	-1.281866800499370E+00	3.069529014714890E+00	1.958238132037810E+02	9.96613313774390E+08	1.813979597323180E+09
7.526672529351230E-01	-1.583187977449590E+00	2.983961316513780E+00	1.773270603421570E+02	8.171417199914880E+08	1.608810429907780E+09
7.717438522715810E-01	-1.875204470207720E+00	2.898006382996990E+00	1.580480684017000E+02	6.650427810101700E+08	1.409845591388380E+09
8.000000000000000E-01	-2.236867726960520E+00	2.768221228578390E+00	1.308803316436120E+02	4.763147533402140E+08	1.140413198030610E+09
8.187500000000000E-01	-2.407559875105570E+00	2.679571699358600E+00	1.080727916418520E+02	3.713141853435260E+08	8.700627225751990E+08
8.375000000000000E-01	-2.466589245326670E+00	2.588234998923030E+00	9.150936098622500E+01	2.893865993705260E+08	7.041913506235870E+08
8.562500000000000E-01	-2.476064619564120E+00	2.493925003782620E+00	7.607094692740400E+01	2.264130751951890E+08	5.507431587157230E+08
8.750000000000000E-01	-2.461185304881360E+00	2.397357498996970E+00	6.292540081449140E+01	1.723143761545730E+08	4.301476448844400E+08
8.937500000000000E-01	-2.418517957471360E+00	2.298574617144000E+00	5.242046309492390E+01	1.270110653335580E+08	3.401008599718350E+08
9.125000000000000E-01	-2.348882314259700E+00	2.197674647152620E+00	4.391521865519060E+01	8.934124860145950E+07	2.696896658521860E+08
9.312499999999990E-01	-2.251426912022270E+00	2.09474664459370E+00	3.657386444140900E+01	5.919208136594120E+07	2.083477806158130E+08
9.500000000000000E-01	-2.115172386244970E+00	1.989485429115940E+00	3.001364550193750E+01	3.618641447630920E+07	1.518776629006610E+08
9.750000000000000E-01	-1.867929958032100E+00	1.848333283013630E+00	2.133248407568760E+01	1.563569346208850E+07	8.893722670711870E+07
1.000000000000000E+00	-1.542387706272960E+00	5.000000000000000E-01	5.407971821081970E+00	1.888459826881500E+05	1.920687333755170E+06

A.2 Elastodyn Inputs for Twist Angle Profile #2

Table A.2: ElastoDyn OpenFAST input data for twist angle profile #2.

Blade Fraction r/R (-)	Twist Angle (deg)	Chord Length (m)	Mass Density (kg/m)	Flapwise Stiffness (Nm ²)	Edgewise Stiffness (Nm ²)
0.000000000000000E+00	1.459455301971170E+01	5.200000000000000E+00	3.179059159259060E+03	1.525336732671640E+11	1.524092444021610E+11
2.000000000000000E-02	1.459105026258910E+01	5.208280051053220E+00	2.844639124071310E+03	1.396059559125450E+11	1.371910901056170E+11
4.000000000000000E-02	1.442808288705690E+01	5.235714686841760E+00	2.505353762822230E+03	1.239755438005000E+11	1.211943594444680E+11
6.000000000000000E-02	1.398668187913840E+01	5.288938619667070E+00	2.150176072709730E+03	1.032257195889790E+11	1.030637624551030E+11
8.000000000000000E-02	1.332158034416250E+01	5.360587950371890E+00	1.807166613880170E+03	8.162835042138820E+10	8.436578661171380E+10
1.000000000000000E-01	1.248751138745820E+01	5.443298779798940E+00	1.689570275067180E+03	6.177531809788480E+10	6.862655814157260E+10
1.250000000000000E-01	1.129069721992210E+01	5.551024109038490E+00	1.296524292073250E+03	4.274720146392410E+10	5.134664996974550E+10
1.500000000000000E-01	1.002229252935760E+01	5.650144322056730E+00	9.822677239823060E+02	3.237301609568750E+10	3.898538145499410E+10
1.690340633511320E-01	9.074551005218500E+00	5.710964180985910E+00	7.966163346309950E+02	2.827287353472030E+10	3.195263357170140E+10
1.880681267022640E-01	8.194457415112660E+00	5.752111033293940E+00	6.645041811187670E+02	2.481852933449630E+10	2.695846118026080E+10
2.071021900533960E-01	7.429191400183100E+00	5.767237237684650E+00	5.764843213881020E+02	2.195610441457930E+10	2.376092222912670E+10
2.261362534045280E-01	6.777140178454870E+00	5.754540379641520E+00	5.250180685658330E+02	1.967142143571740E+10	2.20846521313590E+10
2.451703167556600E-01	6.182453068336750E+00	5.702616552569120E+00	4.925364059605150E+02	1.805224163293000E+10	2.106608767500110E+10
2.660887252285560E-01	5.526991264456790E+00	5.600650141179930E+00	4.671178249482400E+02	1.671838806704950E+10	2.035217171041800E+10
2.870071337014520E-01	4.894967665228040E+00	5.463153391746180E+00	4.526892330366370E+02	1.545040426884080E+10	1.996217848145590E+10
3.079255421743470E-01	4.294241247126910E+00	5.309456651571880E+00	4.478982718495180E+02	1.425262350769260E+10	1.971283876391980E+10
3.288439506472430E-01	3.734510589122640E+00	5.148771194775270E+00	4.434501720049930E+02	1.301246687693210E+10	1.913520606370910E+10
3.509110298069780E-01	3.200509221861600E+00	4.991052530953460E+00	4.383992071132160E+02	1.177142473319300E+10	1.830911869625890E+10
3.729781089667120E-01	2.725899877374300E+00	4.849825861125230E+00	4.303870023258640E+02	1.063075751402770E+10	1.726648597667800E+10
3.950451881264470E-01	2.306980159403290E+00	4.727623031975450E+00	4.199515443050740E+02	9.612894282647330E+09	1.605865945507700E+10
4.171122672861810E-01	1.919972991579770E+00	4.604744127582390E+00	4.077257161686330E+02	8.632215309868140E+09	1.470313795543420E+10
4.391793464459160E-01	1.561013760569930E+00	4.482053325831180E+00	3.924438241159640E+02	7.670161976417180E+09	1.306446466642580E+10
4.58877585784190E-01	1.261976958738840E+00	4.373759436309790E+00	3.781497498899630E+02	6.850238547683750E+09	1.161760885274030E+10
4.785761707109230E-01	9.803086132173600E-01	4.267298674782820E+00	3.635693457624110E+02	6.080518723471740E+09	1.023131799902930E+10
4.982745828434270E-01	9.318558488495230E-01	4.162982209701330E+00	3.492150624323850E+02	5.377222884634280E+09	8.95722703042520E+09
5.179729949759310E-01	7.932919574417950E-01	4.061706722205010E+00	3.360065859722420E+02	4.753629978034940E+09	7.881195883717870E+09
5.376714071084350E-01	5.956673907097070E-01	3.963536198880920E+00	3.236134228528660E+02	4.208216667668420E+09	6.945396072547720E+09
5.577786570700220E-01	3.887150256003910E-01	3.866942578335680E+00	3.111722310592850E+02	3.718761715312920E+09	6.048539773167900E+09
5.778859070316100E-01	2.331272946285590E-01	3.773008482150570E+00	2.987202701527960E+02	3.278832254292590E+09	5.213943536606200E+09
5.979931569931980E-01	1.300000000000000E-01	3.681310369877000E+00	2.861632387471790E+02	2.885527839847520E+09	4.436841796990030E+09
6.181004069547860E-01	-1.198096538142140E-01	3.590736963146060E+00	2.737130089608080E+02	2.533674784416490E+09	3.759425782667440E+09
6.382076569163730E-01	-3.140134479484750E-01	3.500781512082170E+00	2.614646456667160E+02	2.220537999215230E+09	3.191905368536750E+09
6.572842562528320E-01	-5.018950660288040E-01	3.415119535682270E+00	2.500840447242680E+02	1.944279119832140E+09	2.760285285665830E+09
6.763608555892900E-01	-7.032949456984740E-01	3.328844727050610E+00	2.388570448427700E+02	1.679737195885030E+09	2.455134058468400E+09
6.954374549257480E-01	-9.252875829492340E-01	3.241551330883460E+00	2.271577540416740E+02	1.433783698230150E+09	2.232548383641040E+09
7.145140542622060E-01	-1.183536256057470E+00	3.155076129554680E+00	2.131533971390730E+02	1.206419926990950E+09	2.024234582445270E+09
7.335906535986650E-01	-1.481866800499370E+00	3.069529014714890E+00	1.958238132037810E+02	9.966133137774390E+08	1.813979597323180E+09
7.526672529351230E-01	-1.783187977449590E+00	2.983961316513780E+00	1.773270603421570E+02	8.171417199914880E+08	1.608810429907780E+09
7.717438522715810E-01	-2.075204470207720E+00	2.898006382996990E+00	1.580480684017000E+02	6.650427810101700E+08	1.409845591388380E+09
8.000000000000000E-01	-2.436867726960520E+00	2.768221228578390E+00	1.308803316436120E+02	4.763147533402140E+08	1.140413198030610E+09
8.187500000000000E-01	-2.607559875105570E+00	2.679571699358600E+00	1.080727916418520E+02	3.713141853435260E+08	8.700627225751990E+08
8.375000000000000E-01	-2.666589245326670E+00	2.588234998923030E+00	9.150936098622500E+01	2.893865993705260E+08	7.041913506235870E+08
8.562500000000000E-01	-2.676064619564120E+00	2.493925003782620E+00	7.607094692740400E+01	2.264130751951890E+08	5.507431587157230E+08
8.750000000000000E-01	-2.661185304881360E+00	2.397357498996970E+00	6.292540081449140E+01	1.723143761545730E+08	4.301476448844400E+08
8.937500000000000E-01	-2.618517957471360E+00	2.298574617144000E+00	5.242046309492390E+01	1.270110653335580E+08	3.401008599718350E+08
9.125000000000000E-01	-2.548882314259700E+00	2.197674647152620E+00	4.391521865519060E+01	8.934124860145950E+07	2.696896658521860E+08
9.312499999999990E-01	-2.451426912022270E+00	2.09474664459370E+00	3.657386444140900E+01	5.919208136594120E+07	2.083477806158130E+08
9.500000000000000E-01	-2.315172386244970E+00	1.989485429115940E+00	3.001364550193750E+01	3.618641447630920E+07	1.518776629006610E+08
9.750000000000000E-01	-2.067929958032100E+00	1.848333283013630E+00	2.133248407568760E+01	1.563569346208850E+07	8.893722670711870E+07
1.000000000000000E+00	-1.742387706272960E+00	5.000000000000000E-01	5.407971821081970E+00	1.888459826881500E+05	1.920687333755170E+06

A.3 Elastodyn Inputs for Twist Angle Profile #3

Table A.3: ElastoDyn OpenFAST input data for twist angle profile #3.

Blade Fraction r/R (-)	Twist Angle (deg)	Chord Length (m)	Mass Density (kg/m)	Flapwise Stiffness (Nm ²)	Edgewise Stiffness (Nm ²)
0.000000000000000E+00	1.559455301971170E+01	5.200000000000000E+00	3.179059159259060E+03	1.525336732671640E+11	1.524092444021610E+11
2.000000000000000E-02	1.559105026258910E+01	5.208280051053220E+00	2.844639124071310E+03	1.396059559125450E+11	1.371910901056170E+11
4.000000000000000E-02	1.542808288705690E+01	5.235714686841760E+00	2.505353762822230E+03	1.239755438005000E+11	1.211943594444680E+11
6.000000000000000E-02	1.498668187913840E+01	5.288938619667070E+00	2.150176072709730E+03	1.032257195889790E+11	1.030637624551030E+11
8.000000000000000E-02	1.432158034416250E+01	5.360587950371890E+00	1.807166613880170E+03	8.162835042138820E+10	8.436578661171380E+10
1.000000000000000E-01	1.348751138745820E+01	5.443298779798940E+00	1.689750275067180E+03	6.177531809788480E+10	6.862655814157260E+10
1.250000000000000E-01	1.229069721992210E+01	5.551024109038490E+00	1.296524292073250E+03	4.274720146392410E+10	5.134664996974550E+10
1.500000000000000E-01	1.10222952935760E+01	5.650144322056730E+00	9.822677239823060E+02	3.237301609568750E+10	3.898538145499410E+10
1.690340633511320E-01	1.007455100521850E+01	5.710964180985910E+00	7.966163346309950E+02	2.827287353472030E+10	3.195263357170140E+10
1.880681267022640E-01	9.194457415112660E+00	5.752111033293940E+00	6.645041811187670E+02	2.481852933449630E+10	2.695846118026080E+10
2.071021900533960E-01	8.429191400183100E+00	5.767237237684650E+00	5.764843213881020E+02	2.195610441457930E+10	2.376025222912670E+10
2.261362534045280E-01	7.777140178454870E+00	5.754540379641520E+00	5.250180685658330E+02	1.967142143571740E+10	2.20846521313590E+10
2.451703167556600E-01	7.182453068336750E+00	5.702616552569120E+00	4.925364059605150E+02	1.805224163293000E+10	2.106608767500110E+10
2.660887252285560E-01	6.526991264456790E+00	5.600650141179930E+00	4.671178249482400E+02	1.671838806704950E+10	2.035217171041800E+10
2.870071337014520E-01	5.530059716904850E+00	5.463153391746180E+00	4.526892330366370E+02	1.545040426884080E+10	1.996217848145590E+10
3.079255421743470E-01	4.785284799548210E+00	5.309456651571880E+00	4.478982718495180E+02	1.425262350769260E+10	1.971283876391980E+10
3.288439506472430E-01	4.103871106220670E+00	5.148771194775270E+00	4.434501720049930E+02	1.301246687693210E+10	1.913520606370910E+10
3.509110298069780E-01	3.450590793395070E+00	4.991052530953460E+00	4.383992071132160E+02	1.177142473319300E+10	1.830911869625890E+10
3.729781089667120E-01	2.861347589363740E+00	4.849825861125230E+00	4.303870023258640E+02	1.063075751402770E+10	1.726648597667800E+10
3.950451881264470E-01	2.332818123937610E+00	4.727623031975450E+00	4.199515443050740E+02	9.612894282647330E+09	1.605865945507700E+10
4.171122672861810E-01	1.861679026297760E+00	4.604744127582390E+00	4.077257161686330E+02	8.632215309868140E+09	1.470313795543420E+10
4.391793464459160E-01	1.444606928145140E+00	4.482053325831180E+00	3.924438241159640E+02	7.670161976417180E+09	1.306446466642580E+10
4.588777585784190E-01	1.115269316855070E+00	4.373759436309790E+00	3.781497498899630E+02	6.850238547683750E+09	1.161760885274030E+10
4.785761707109230E-01	8.240024602415340E-01	4.267298674782820E+00	3.635693457624110E+02	6.080518723471740E+09	1.023131799902930E+10
4.982745828434270E-01	5.684424108450440E-01	4.162982209701330E+00	3.492150624323850E+02	5.377222884634280E+09	8.957222703042520E+09
5.179729949759310E-01	3.462252212060900E-01	4.061706722205010E+00	3.360065859722420E+02	4.753629978034940E+09	7.881195883717870E+09
5.376714071084350E-01	1.549869438651680E-01	3.963536198880920E+00	3.236134228528660E+02	4.208216667668420E+09	6.945396072547720E+09
5.577786570700220E-01	-1.072534724028530E-02	3.866942578335680E+00	3.111722310592850E+02	3.718761715312920E+09	6.048539773187900E+09
5.778859070316100E-01	-1.491367616164960E-01	3.773008482150570E+00	2.987202701527960E+02	3.278832254292590E+09	5.213943536606200E+09
5.979931569931980E-01	-2.627615129814840E-01	3.681310369877000E+00	2.861632387471790E+02	2.885527839847520E+09	4.436841796990030E+09
6.181004069547860E-01	-3.541138150532750E-01	3.590736963146060E+00	2.737130089608080E+02	2.533674784416490E+09	3.759425782667440E+09
6.382076569163730E-01	-4.257078815498900E-01	3.500781512082170E+00	2.614646456667160E+02	2.220537999215230E+09	3.191905368536750E+09
6.572842562528320E-01	-4.776516499168790E-01	3.415119535682270E+00	2.500840447242680E+02	1.944279119832140E+09	2.760285285665830E+09
6.763608555892900E-01	-6.000000000000000E-01	3.328844727050610E+00	2.388570448427700E+02	1.679737195885030E+09	2.455134058468400E+09
6.954374549257480E-01	-8.000000000000000E-01	3.241551330883460E+00	2.271577540416740E+02	1.433783698230150E+09	2.232548383641040E+09
7.145140542622060E-01	-1.183536256057470E+00	3.155076129554680E+00	2.131533971390730E+02	1.206419926990950E+09	2.024234582445270E+09
7.335906535986650E-01	-1.481866800499370E+00	3.069529014714890E+00	1.958238132037810E+02	9.966133137774390E+08	1.813979597323180E+09
7.526672529351230E-01	-1.783187977449590E+00	2.983961316513780E+00	1.773270603421570E+02	8.171417199914880E+08	1.608810429907780E+09
7.717438522715810E-01	-2.075204470207720E+00	2.898006382996990E+00	1.580480684017000E+02	6.650427810101700E+08	1.409845591388380E+09
8.000000000000000E-01	-2.436867726960520E+00	2.768221228578390E+00	1.308803316436120E+02	4.763147533402140E+08	1.140413198030610E+09
8.187500000000000E-01	-2.607559875105570E+00	2.679571699358600E+00	1.080727916418520E+02	3.713141853435260E+08	8.700627225751990E+08
8.375000000000000E-01	-2.666589245326670E+00	2.588234998923030E+00	9.150936098622500E+01	2.893865993705260E+08	7.041913506235870E+08
8.562500000000000E-01	-2.676064619564120E+00	2.493925003782620E+00	7.607094692740400E+01	2.264130751951890E+08	5.507431587157230E+08
8.750000000000000E-01	-2.661185304881360E+00	2.397357498996970E+00	6.292540081449140E+01	1.723143761545730E+08	4.301476448844400E+08
8.937500000000000E-01	-2.618517957471360E+00	2.298574617144000E+00	5.242046309492390E+01	1.270110653335580E+08	3.401008599718350E+08
9.125000000000000E-01	-2.548882314259700E+00	2.197674647152620E+00	4.391521865519060E+01	8.934124860145950E+07	2.696896658521860E+08
9.312499999999990E-01	-2.451426912022270E+00	2.09474664459370E+00	3.657386444140900E+01	5.919208136594120E+07	2.083477806158130E+08
9.500000000000000E-01	-2.315172386244970E+00	1.989485429115940E+00	3.001364550193750E+01	3.618641447630920E+07	1.518776629006610E+08
9.750000000000000E-01	-2.067929958032100E+00	1.848333283013630E+00	2.133248407568760E+01	1.563569346208850E+07	8.893722670711870E+07
1.000000000000000E+00	-1.742387706272960E+00	5.000000000000000E-01	5.407971821081970E+00	1.888459826881500E+05	1.920687333755170E+06

A.4 Elastodyn Inputs for Twist Angle Profile #4

Table A.4: ElastoDyn OpenFAST input data for twist angle profile #4.

Blade Fraction r/R (-)	Twist Angle (deg)	Chord Length (m)	Mass Density (kg/m)	Flapwise Stiffness (Nm ²)	Edgewise Stiffness (Nm ²)
0.00000000000000E+00	1.559455301971170E+01	5.20000000000000E+00	3.179059159259060E+03	1.525336732671640E+11	1.524092444021610E+11
2.00000000000000E-02	1.559105026258910E+01	5.208280051053220E+00	2.844639124071310E+03	1.396059559125450E+11	1.371910901056170E+11
4.00000000000000E-02	1.542808288705690E+01	5.235714686841760E+00	2.505353762822230E+03	1.239755438005000E+11	1.211943594444680E+11
6.00000000000000E-02	1.498668187913840E+01	5.288938619667070E+00	2.150176072709730E+03	1.032257195889790E+11	1.030637624551030E+11
8.00000000000000E-02	1.432158034416250E+01	5.360587950371890E+00	1.807166613880170E+03	8.162835042138820E+10	8.436578661171380E+10
1.00000000000000E-01	1.348751138745820E+01	5.443298779798940E+00	1.689750275067180E+03	6.177531809788480E+10	6.862655814157260E+10
1.25000000000000E-01	1.229069721992210E+01	5.551024109038490E+00	1.296524292073250E+03	4.274720146392410E+10	5.134664996974550E+10
1.50000000000000E-01	1.10222952935760E+01	5.650144322056730E+00	9.822677239823060E+02	3.237301609568750E+10	3.898538145499410E+10
1.690340633511320E-01	1.007455100521850E+01	5.710964180985910E+00	7.966163346309950E+02	2.827287353472030E+10	3.195263357170140E+10
1.880681267022640E-01	9.194457415112660E+00	5.752111033293940E+00	6.645041811187670E+02	2.481852933449630E+10	2.695846118026080E+10
2.071021900533960E-01	8.429191400183100E+00	5.767237237684650E+00	5.764843213881020E+02	2.195610441457930E+10	2.376092222912670E+10
2.261362534045280E-01	7.777140178454870E+00	5.754540379641520E+00	5.250180685658330E+02	1.967142143571740E+10	2.20846521313590E+10
2.451703167556600E-01	7.182453068336750E+00	5.702616552569120E+00	4.925364059605150E+02	1.805224163293000E+10	2.106608767500110E+10
2.660887252285560E-01	6.526991264456790E+00	5.600650141179930E+00	4.671178249482400E+02	1.671838806704950E+10	2.035217171041800E+10
2.870071337014520E-01	5.530059716904850E+00	5.463153391746180E+00	4.526892330366370E+02	1.545040426884080E+10	1.996217848145590E+10
3.079255421743470E-01	4.785284799548210E+00	5.309456651571880E+00	4.478982718495180E+02	1.425262350769260E+10	1.971283876391980E+10
3.288439506472430E-01	4.103871106220670E+00	5.148771194775270E+00	4.434501720049930E+02	1.301246687693210E+10	1.913520606370910E+10
3.509110298069780E-01	3.450590793395070E+00	4.991052530953460E+00	4.383992071132160E+02	1.177142473319300E+10	1.830911869625890E+10
3.729781089667120E-01	2.861347589363740E+00	4.849825861125230E+00	4.303870023258640E+02	1.063075751402770E+10	1.726648597667800E+10
3.950451881264470E-01	2.332818123937610E+00	4.727623031975450E+00	4.199515443050740E+02	9.612894282647330E+09	1.605865945507700E+10
4.171122672861810E-01	1.861679026927760E+00	4.604744127582390E+00	4.077257161686330E+02	8.632215309868140E+09	1.470313795543420E+10
4.391793464459160E-01	1.444606928145140E+00	4.482053325831180E+00	3.924438241159640E+02	7.670161976417180E+09	1.306446466642580E+10
4.588777585784190E-01	1.115269316855070E+00	4.373759436309790E+00	3.781497498899630E+02	6.850238547683750E+09	1.161760885274030E+10
4.785761707109230E-01	8.240024602415340E-01	4.267298674782820E+00	3.635693457624110E+02	6.080518723471740E+09	1.023131799902930E+10
4.982745828434270E-01	5.684424108450440E-01	4.162982209701330E+00	3.492150624323850E+02	5.377222884634280E+09	8.957222703042520E+09
5.179729949759310E-01	3.462252212060900E-01	4.061706722205010E+00	3.360065859722420E+02	4.753629978034940E+09	7.881195883717870E+09
5.376714071084350E-01	1.549869438651680E-01	3.963536198880920E+00	3.236134228528660E+02	4.208216667668420E+09	6.945396072547720E+09
5.577786570700220E-01	-1.072534724028530E-02	3.866942578335680E+00	3.111722310592850E+02	3.718761715312920E+09	6.048539773187900E+09
5.778859070316100E-01	-1.491367616164960E-01	3.773008482150570E+00	2.987202701527960E+02	3.278832254292590E+09	5.213943536606200E+09
5.979931569931980E-01	-2.627615129814840E-01	3.681310369877000E+00	2.861632387471790E+02	2.885527839847520E+09	4.436841796990030E+09
6.181004069547860E-01	-3.541138150532750E-01	3.590736963146060E+00	2.737130089608080E+02	2.533674784416490E+09	3.759425782667440E+09
6.382076569163730E-01	-4.257078815498900E-01	3.500781512082170E+00	2.614646456667160E+02	2.220537999215230E+09	3.191905368536750E+09
6.572842562528320E-01	-4.776516499168790E-01	3.415119535682270E+00	2.500840447242680E+02	1.944279119832140E+09	2.760285285665830E+09
6.763608555892900E-01	-5.162209409894910E-01	3.328844727050610E+00	2.388570448427700E+02	1.679737195885030E+09	2.455134058468400E+09
6.954374549257480E-01	-6.00000000000000E-01	3.241551330883460E+00	2.271577540416740E+02	1.433783698230150E+09	2.232548383641040E+09
7.145140542622060E-01	-6.835362560574680E-01	3.155076129554680E+00	2.131533971390730E+02	1.206419926990950E+09	2.024234582445270E+09
7.335906535986650E-01	-9.818668004993730E-01	3.069529014714890E+00	1.958238132037810E+02	9.966133137774390E+08	1.813979597323180E+09
7.526672529351230E-01	-1.283187977449590E+00	2.983961316513780E+00	1.773270603421570E+02	8.171417199914880E+08	1.608810429907780E+09
7.717438522715810E-01	-1.575204470207720E+00	2.898006382996990E+00	1.580480684017000E+02	6.650427810101700E+08	1.409845591388380E+09
8.00000000000000E-01	-1.936867726960520E+00	2.768221228578390E+00	1.308803316436120E+02	4.763147533402140E+08	1.140413198030610E+09
8.18750000000000E-01	-2.107559875105570E+00	2.679571699358600E+00	1.080727916418520E+02	3.713141853435260E+08	8.700627225751990E+08
8.37500000000000E-01	-2.166589245326670E+00	2.588234998923030E+00	9.150936098622500E+01	2.893865993705260E+08	7.041913506235870E+08
8.56250000000000E-01	-2.176064619564120E+00	2.493925003782620E+00	7.607094692740400E+01	2.264130751951890E+08	5.507431587157230E+08
8.75000000000000E-01	-2.161185304881360E+00	2.397357498996970E+00	6.292540081449140E+01	1.723143761545730E+08	4.301476448844400E+08
8.93750000000000E-01	-2.118517957471360E+00	2.298574617144000E+00	5.242046309492390E+01	1.270110653335580E+08	3.401008599718350E+08
9.12500000000000E-01	-2.048882314259700E+00	2.197674647152620E+00	4.391521865519060E+01	8.934124860145950E+07	2.696896658521860E+08
9.31249999999999E-01	-1.951426912022270E+00	2.09474664459370E+00	3.657386444140900E+01	5.919208136594120E+07	2.083477806158130E+08
9.50000000000000E-01	-1.815172386244970E+00	1.989485429115940E+00	3.001364550193750E+01	3.618641447630920E+07	1.518776629006610E+08
9.75000000000000E-01	-1.567929958032100E+00	1.848333283013630E+00	2.133248407568760E+01	1.563569346208850E+07	8.893722670711870E+07
1.00000000000000E+00	-1.242387706272960E+00	5.00000000000000E-01	5.407971821081970E+00	1.888459826881500E+05	1.920687333755170E+06

B | Supportive Figures For Blade Twist

B.1 Power Curves of Twist Profiles 1-4

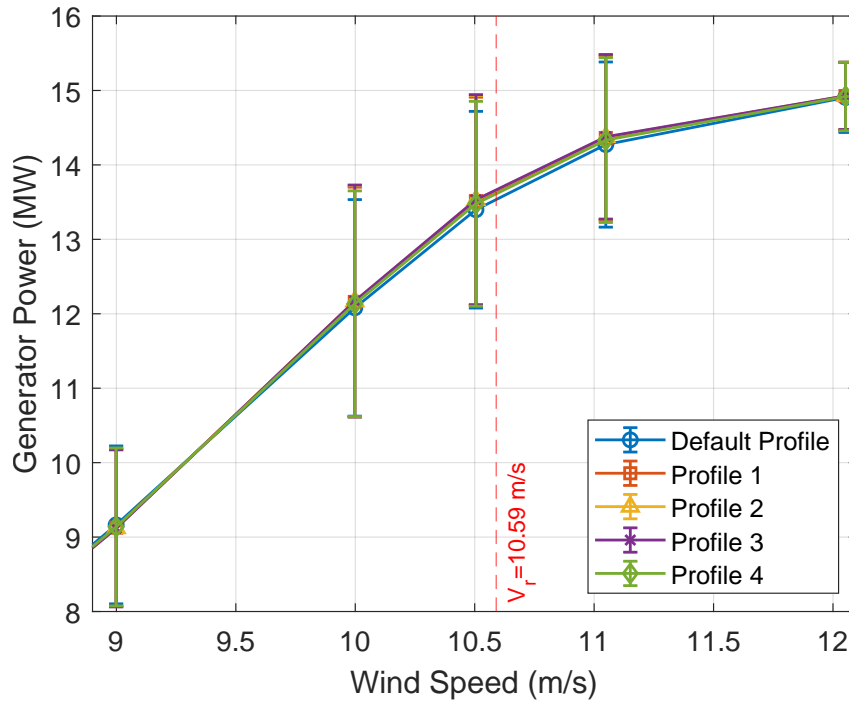


Figure B.1: Power Curves of the IEA 15 MW FOWT according to the original and redesigned blade twist angle profiles for average wind speeds between 9 and 12 m/s. Blue curve: Original blade twist angle profile. Orange curve: Blade twist profile 1. Orange curve: Blade twist profile 2. Purple curve: Blade twist profile 3. Green curve: Blade twist profile 4.

C | ElastoDyn Inputs for Blade Chord Length Profiles

C.1 Elastodyn Inputs for Profile #1

Table C.1: ElastoDyn OpenFAST input data for chord length profile #1.

Blade Fraction r/R (-)	Twist Angle (deg)	Chord Length (m)	Mass Density (kg/m)	Flapwise Stiffness (Nm ²)	Edgewise Stiffness (Nm ²)
0.00000000000000E+00	1.559455301971170E+01	5.20000000000000E+00	3.179059159259060E+03	1.525336732671640E+11	1.524092444021610E+11
2.00000000000000E-02	1.559105026258910E+01	5.208280051053220E+00	2.844639124071310E+03	1.396059559125450E+11	1.371910901056170E+11
4.00000000000000E-02	1.542808288705690E+01	5.235714686841760E+00	2.505353762822230E+03	1.239755438005000E+11	1.211943594444680E+11
6.00000000000000E-02	1.498668187913840E+01	5.288938619667070E+00	2.150176072709730E+03	1.032257195889790E+11	1.030637624551030E+11
8.00000000000000E-02	1.432158034416250E+01	5.360587950371890E+00	1.807166613880170E+03	8.162835042138820E+10	8.436578661171380E+10
1.00000000000000E-01	1.348751138745820E+01	5.443298779798940E+00	1.689750275067180E+03	6.177531809788480E+10	6.862655814157260E+10
1.25000000000000E-01	1.229069721992210E+01	5.551024109038490E+00	1.296524292073250E+03	4.274720146392410E+10	5.134664996974550E+10
1.50000000000000E-01	1.102229252935760E+01	5.650144322056730E+00	9.822677239823060E+02	3.237301609568750E+10	3.898538145499410E+10
1.690340633511320E-01	1.007455100521850E+01	5.710964180985910E+00	7.966163346309950E+02	2.827287353472030E+10	3.195263357170140E+10
1.880681267022640E-01	9.194457415112660E+00	5.752111033293940E+00	6.645041811187670E+02	2.481852933449630E+10	2.695846118026080E+10
2.071021900533960E-01	8.429191400183100E+00	5.767237237684650E+00	5.764843213881020E+02	2.195610441457930E+10	2.376092222912670E+10
2.261362534045280E-01	7.777140178454870E+00	5.754540379641520E+00	5.250180685658330E+02	1.967142143571740E+10	2.208465213113590E+10
2.451703167556600E-01	7.182453068336750E+00	5.702616552569120E+00	4.925364059605150E+02	1.805224163293000E+10	2.106608767500110E+10
2.660887252285560E-01	6.526991264456790E+00	5.66000000000000E+00	4.770703368896240E+02	1.743838853733650E+10	2.122866609158050E+10
2.870071337014520E-01	5.894967665228040E+00	5.60000000000000E+00	4.756521125901480E+02	1.705761771854220E+10	2.203872490590380E+10
3.079255421743470E-01	5.294241247126910E+00	5.50000000000000E+00	4.806230631115860E+02	1.641138574136200E+10	2.269862813939840E+10
3.288439506472430E-01	4.734510589122640E+00	5.414446068980050E+00	4.903946309802120E+02	1.591334194951280E+10	2.340102612718320E+10
3.509110298069780E-01	4.200509221861600E+00	5.285993253273950E+00	4.917435671260010E+02	1.481040329090120E+10	2.303590584306610E+10
3.729781089667120E-01	3.725899877374300E+00	5.157567059620720E+00	4.867395363385150E+02	1.359687690597750E+10	2.20840597785580E+10
3.950451881264470E-01	3.306980159403290E+00	5.029277742286680E+00	4.752528649287380E+02	1.231133894372830E+10	2.056650096425630E+10
4.171122672861810E-01	2.919972991579770E+00	4.901235555381600E+00	4.619215774270670E+02	1.107956105402360E+10	1.887166953270230E+10
4.391793464459160E-01	2.561013760569930E+00	4.773550753641490E+00	4.451501758651430E+02	9.868761103075070E+09	1.680930352304580E+10
4.58877585784190E-01	2.261976958738840E+00	4.659963268248410E+00	4.292586143884680E+02	8.827060415688810E+09	1.497018454396080E+10
4.785761707109230E-01	1.980308613217360E+00	4.546826842784360E+00	4.127603836580280E+02	7.837221616102670E+09	1.318721481338190E+10
4.982745828434270E-01	1.713584420221960E+00	4.434219902245020E+00	3.962035033643260E+02	6.921635512452360E+09	1.152986068914650E+10
5.179729949759310E-01	1.457959216148460E+00	4.32220871626090E+00	3.804911667123080E+02	6.095634958787730E+09	1.010614906246950E+10
5.376714071084350E-01	1.215627353698100E+00	4.210908175923290E+00	3.652686600726060E+02	5.361296933567300E+09	8.848482292332020E+09
5.57786570700220E-01	9.878931973599970E-01	4.098074493493870E+00	3.494822190919760E+02	4.690799316243830E+09	7.629552094051390E+09
5.778859070316100E-01	7.751486517583760E-01	3.986121055525530E+00	3.334188105122500E+02	4.084792570171320E+09	6.495567985138300E+09
5.979931569931980E-01	5.753772042113690E-01	3.875131272163140E+00	3.170894642096510E+02	3.542918876217880E+09	5.447658600368620E+09
6.181004069547860E-01	3.801903461857860E-01	3.765188553551550E+00	3.009551044187390E+02	3.063115823160410E+09	4.545001857267910E+09
6.382076569163730E-01	1.859865520515250E-01	3.656376309835630E+00	2.852231242401380E+02	2.642419271615530E+09	3.798337277711710E+09
6.572842562528320E-01	-1.895066028803550E-03	3.504262358235950E+00	2.633100243059760E+02	2.155367991139850E+09	3.059967311510340E+09
6.763608555892900E-01	-2.032949456984740E-01	3.373312269283780E+00	2.452810917253120E+02	1.771305089827830E+09	2.588971337080740E+09
6.954374549257480E-01	-4.252875829492340E-01	3.241551330883460E+00	2.271577540416740E+02	1.433783698230150E+09	2.232548383641040E+09
7.145140542622060E-01	-6.835362560574680E-01	3.155076129554680E+00	2.131533971390730E+02	1.206419926990950E+09	2.024234582445270E+09
7.335906535986650E-01	-9.818668040993730E-01	3.069529014714890E+00	1.958238132037810E+02	9.96613313774390E+08	1.813979597323180E+09
7.526672529351230E-01	-1.283187977449590E+00	2.983961316513780E+00	1.773270603421570E+02	8.171417199914880E+08	1.608810429907780E+09
7.717438522715810E-01	-1.575204470207720E+00	2.898006382996990E+00	1.580480684017000E+02	6.650427810101700E+08	1.409845591388380E+09
8.00000000000000E-01	-1.936867726960520E+00	2.768221228578390E+00	1.308803316436120E+02	4.763147533402140E+08	1.140413198030610E+09
8.18750000000000E-01	-2.107559875105570E+00	2.679571699358600E+00	1.080727916418520E+02	3.713141853435260E+08	8.700627225751990E+08
8.37500000000000E-01	-2.166589245326670E+00	2.588234998923030E+00	9.150936098622500E+01	2.893865993705260E+08	7.041913506235870E+08
8.56250000000000E-01	-2.176064619564120E+00	2.493925003782620E+00	7.607094692740400E+01	2.264130751951890E+08	5.507431587157230E+08
8.75000000000000E-01	-2.161185304881360E+00	2.397357498996970E+00	6.292540081449140E+01	1.723143761545730E+08	4.301476448844400E+08
8.93750000000000E-01	-2.118517957471360E+00	2.298574617144000E+00	5.242046309492390E+01	1.270110653335580E+08	3.401008599718350E+08
9.12500000000000E-01	-2.048882314259700E+00	2.197674647152620E+00	4.391521865519060E+01	8.934124860145950E+07	2.696896658521860E+08
9.31249999999999E-01	-1.951426912022270E+00	2.09474664459370E+00	3.657386444140900E+01	5.919208136594120E+07	2.083477806158130E+08
9.50000000000000E-01	-1.815172386244970E+00	1.989485429115940E+00	3.001364550193750E+01	3.618641447630920E+07	1.518776629006610E+08
9.75000000000000E-01	-1.567929958032100E+00	1.848333283013630E+00	2.133248407568760E+01	1.563569346208850E+07	8.893722670711870E+07
1.00000000000000E+00	-1.242387706272960E+00	5.00000000000000E-01	5.407971821081970E+00	1.888459826881500E+05	1.920687333755170E+06

C.2 Elastodyn Inputs for Profile #2

Table C.2: ElastoDyn OpenFAST input data for chord length profile #2.

Blade Fraction r/R (-)	Twist Angle (deg)	Chord Length (m)	Mass Density (kg/m)	Flapwise Stiffness (Nm ²)	Edgewise Stiffness (Nm ²)
0.000000000000000E+00	1.559455301971170E+01	5.200000000000000E+00	3.179059159259060E+03	1.525336732671640E+11	1.524092444021610E+11
2.000000000000000E-02	1.559105026258910E+01	5.208280051053220E+00	2.844639124071310E+03	1.396059559125450E+11	1.371910901056170E+11
4.000000000000000E-02	1.542808288705690E+01	5.235714686841760E+00	2.505353762822230E+03	1.239755438005000E+11	1.211943594444680E+11
6.000000000000000E-02	1.498668187913840E+01	5.288938619667070E+00	2.150176072709730E+03	1.032257195889790E+11	1.030637624551030E+11
8.000000000000000E-02	1.432158034416250E+01	5.360587950371890E+00	1.807166613880170E+03	8.162835042138820E+10	8.436578661171380E+10
1.000000000000000E-01	1.348751138745820E+01	5.443298779798940E+00	1.689750275067180E+03	6.177531809788480E+10	6.862655814517260E+10
1.250000000000000E-01	1.229069721992210E+01	5.551024109038490E+00	1.296524292073250E+03	4.274720146392410E+10	5.134664996974550E+10
1.500000000000000E-01	1.10229252935760E+01	5.650144322056730E+00	9.822677239823060E+02	3.237301609568750E+10	3.898538145499410E+10
1.690340633511320E-01	1.007455100521850E+01	5.710964180985910E+00	7.966163346309950E+02	2.827287353472030E+10	3.195263357170140E+10
1.880681267022640E-01	9.194457415112660E+00	5.752111033293940E+00	6.645041811187670E+02	2.481852933449630E+10	2.695846118026080E+10
2.071021900533960E-01	8.429191400183100E+00	5.767237237684650E+00	5.764843213881020E+02	2.195610441457930E+10	2.376092222912670E+10
2.261362534045280E-01	7.777140178454870E+00	5.754540379641520E+00	5.250180685658330E+02	1.967142143571740E+10	2.20846521313590E+10
2.451703167556600E-01	7.182453068336750E+00	5.720000000000000E+00	4.955438080910410E+02	1.827336679785240E+10	2.132412998388020E+10
2.660887252285560E-01	6.526991264456790E+00	5.660000000000000E+00	4.770703368896240E+02	1.743838853733650E+10	2.122866609158050E+10
2.870071337014520E-01	5.894967665228040E+00	5.600000000000000E+00	4.756521125901480E+02	1.705761771854220E+10	2.203872490590380E+10
3.079255421743470E-01	5.294241247126910E+00	5.500000000000000E+00	4.806230631115860E+02	1.641138574136200E+10	2.269862813939840E+10
3.288439506472430E-01	4.734510589122640E+00	5.404618988058360E+00	4.886161390177730E+02	1.579812686096880E+10	2.323159903224500E+10
3.509110298069780E-01	4.200509221861600E+00	5.267037282029350E+00	4.882230317367100E+02	1.459909842510450E+10	2.270724503414950E+10
3.729781089667120E-01	3.725899877374300E+00	5.133041949405840E+00	4.821214834495360E+02	1.334009388527780E+10	2.166699256320900E+10
3.950451881264470E-01	3.306980159403290E+00	5.002398864539460E+00	4.701864802884000E+02	1.205025051106350E+10	2.013034405827730E+10
4.171122672861810E-01	2.919972991579770E+00	4.874873901781880E+00	4.569659824299160E+02	1.084310837793040E+10	1.846892282264800E+10
4.391793464459160E-01	2.561013760569930E+00	4.750232935484740E+00	4.408118627439150E+02	9.677341881613760E+09	1.6483326221349530E+10
4.588777585784190E-01	2.261976958738840E+00	4.641216415200210E+00	4.258117798035840E+02	8.685871575066730E+09	1.473073624645340E+10
4.785761707109230E-01	1.980308613217360E+00	4.534144889798160E+00	4.104610624789540E+02	7.750148832544380E+09	1.304070275114510E+10
4.982745828434270E-01	1.713584420221960E+00	4.428851823292470E+00	3.952447938966360E+02	6.888178922893330E+09	1.147412966776350E+10
5.179729949759310E-01	1.457959216148460E+00	4.325170679697040E+00	3.810106954197210E+02	6.112292477631850E+09	1.013376609819880E+10
5.376714071084350E-01	1.215627353698100E+00	4.222934923025770E+00	3.673581224952890E+02	5.422809294239410E+09	8.950004562206480E+09
5.577786570700220E-01	9.878931973599970E-01	4.119895028995690E+00	3.532138211011070E+02	4.791506281344780E+09	7.793351264442410E+09
5.778859070316100E-01	7.751486517583760E-01	4.018010499554340E+00	3.387749304812880E+02	4.217084871740640E+09	6.705936963242350E+09
5.979931569931980E-01	5.753772042113690E-01	3.917104212719100E+00	3.239956846884450E+02	3.698929344042670E+09	5.687543225584910E+09
6.181004069547860E-01	3.801903461857860E-01	3.816999046507380E+00	3.092946138522310E+02	3.235226607305520E+09	4.800377063024340E+09
6.382076569163730E-01	1.859865520515250E-01	3.717517878936560E+00	2.948418256056120E+02	2.823647284351010E+09	4.058842915077100E+09
6.572842562528320E-01	-1.895066028803550E-03	3.623551785953170E+00	2.815419477302320E+02	2.464182472619700E+09	3.498389995030680E+09
6.763608555892900E-01	-2.032949456984740E-01	3.529836674386730E+00	2.685716706872620E+02	2.123663149313340E+09	3.103984206199790E+09
6.954374549257480E-01	-4.252875829492340E-01	3.436221286600930E+00	2.552607303183240E+02	1.810491628441840E+09	2.819121296791750E+09
7.145140542622060E-01	-6.835362560574680E-01	3.342554364959510E+00	2.392376523278610E+02	1.519753137758150E+09	2.549971854247100E+09
7.335906535986650E-01	-9.818668004993730E-01	3.248684651826160E+00	2.193497433787760E+02	1.250460390473060E+09	2.276017793683080E+09
7.526672529351230E-01	-1.283187977449590E+00	3.154460889564630E+00	1.981704663972010E+02	1.020528689483080E+09	2.009244124357760E+09
7.717438522715810E-01	-1.575204470207720E+00	3.059731820538610E+00	1.761802586542230E+02	8.263912025563940E+08	1.751893302136990E+09
8.000000000000000E-01	-1.936867726960520E+00	2.918168613893400E+00	1.453632356205660E+02	5.882099720429340E+08	1.408317526649960E+09
8.187500000000000E-01	-2.107559875105570E+00	2.823195235580150E+00	1.199685556482590E+02	4.575553750716160E+08	1.072142921217560E+09
8.375000000000000E-01	-2.166589245326670E+00	2.727227524418350E+00	1.016016718253390E+02	3.567377587068180E+08	8.680831962109550E+08
8.562500000000000E-01	-2.176064619564120E+00	2.630121859307410E+00	8.460651081562570E+01	2.800731196005650E+08	6.812696414604380E+08
8.750000000000000E-01	-2.161185304881360E+00	2.531734619146740E+00	7.017731491264760E+01	2.143201605202640E+08	5.350065058782380E+08
8.937500000000000E-01	-2.118517957471360E+00	2.431922182835770E+00	5.867903844297830E+01	1.591497018446310E+08	4.261593296573910E+08
9.125000000000000E-01	-2.048882314259700E+00	2.330540929273890E+00	4.938575780321430E+01	1.129861897834630E+08	3.410653896784250E+08
9.312499999999990E-01	-1.951426912022270E+00	2.227447237360540E+00	4.135449166048030E+01	7.567758822181250E+07	2.663744403731080E+08
9.500000000000000E-01	-1.815172386244970E+00	2.122497485995120E+00	3.416107998405240E+01	4.687823376102150E+07	1.967521979608130E+08
9.750000000000000E-01	-1.567929958032100E+00	1.979429046581450E+00	2.446587429702470E+01	2.056628109612310E+07	1.169828513716530E+08
1.000000000000000E+00	-1.242387706272960E+00	5.000000000000000E-01	5.407971821081970E+00	1.888459826881500E+05	1.920687333755170E+06

C.3 Elastodyn Inputs for Profile #3

Table C.3: ElastoDyn OpenFAST input data for chord length profile #3.

Blade Fraction r/R (-)	Twist Angle (deg)	Chord Length (m)	Mass Density (kg/m)	Flapwise Stiffness (Nm ²)	Edgewise Stiffness (Nm ²)
0.00000000000000E+00	1.559455301971170E+01	5.20000000000000E+00	3.179059159259060E+03	1.525336732671640E+11	1.524092444021610E+11
2.00000000000000E-02	1.559105026258910E+01	5.208280051053220E+00	2.844639124071310E+03	1.396059559125450E+11	1.371910901056170E+11
4.00000000000000E-02	1.542808288705690E+01	5.235714686841760E+00	2.505353762822230E+03	1.239755438005000E+11	1.211943594444680E+11
6.00000000000000E-02	1.498668187913840E+01	5.288938619667070E+00	2.150176072709730E+03	1.032257195889790E+11	1.030637624551030E+11
8.00000000000000E-02	1.432158034416250E+01	5.360587950371890E+00	1.807166613880170E+03	8.162835042138820E+10	8.436578661171380E+10
1.00000000000000E-01	1.348751138745820E+01	5.443298779798940E+00	1.689750275067180E+03	6.177531809788480E+10	6.862655814157260E+10
1.25000000000000E-01	1.229069721992210E+01	5.551024109038490E+00	1.296524292073250E+03	4.274720146392410E+10	5.134664996974550E+10
1.50000000000000E-01	1.102229252935760E+01	5.650144322056730E+00	9.822677239823060E+02	3.237301609568750E+10	3.898538145499410E+10
1.690340633511320E-01	1.007455100521850E+01	5.710964180985910E+00	7.966163346309950E+02	2.827287353472030E+10	3.195263357170140E+10
1.880681267022640E-01	9.194457415112660E+00	5.752111033293940E+00	6.645041811187670E+02	2.481852933449630E+10	2.695846118026080E+10
2.071021900533960E-01	8.429191400183100E+00	5.767237237684650E+00	5.764843213881020E+02	2.195610441457930E+10	2.376092222912670E+10
2.261362534045280E-01	7.777140178454870E+00	5.754540379641520E+00	5.250180685658330E+02	1.967142143571740E+10	2.208465213113590E+10
2.451703167556600E-01	7.182453068336750E+00	5.72000000000000E+00	4.955438080910410E+02	1.827336679785240E+10	2.132412998388020E+10
2.660887252285560E-01	6.526991264456790E+00	5.66000000000000E+00	4.770703368896240E+02	1.743838853733650E+10	2.122866609158050E+10
2.870071337014520E-01	5.894967665228040E+00	5.61000000000000E+00	4.773523868829210E+02	1.717978459127930E+10	2.21965663099440E+10
3.079255421743470E-01	5.294241247126910E+00	5.56000000000000E+00	4.911665826051680E+02	1.713932293875850E+10	2.370543987443030E+10
3.288439506472430E-01	4.734510589122640E+00	5.49000000000000E+00	5.041761889570350E+02	1.682033510822160E+10	2.473478560218590E+10
3.509110298069780E-01	4.200509221861600E+00	5.39000000000000E+00	5.112849494208100E+02	1.601089197715720E+10	2.490313010422100E+10
3.729781089667120E-01	3.725899877374300E+00	5.297629921134300E+00	5.135350490606030E+02	1.513512796868490E+10	2.458248854624800E+10
3.950451881264470E-01	3.306980159403290E+00	5.152505591126250E+00	4.988275674545980E+02	1.356302911343980E+10	2.265749100197550E+10
4.171122672861810E-01	2.919972991579770E+00	5.012689906074850E+00	4.831686828931280E+02	1.212226043799550E+10	2.064768557704950E+10
4.3917934644459160E-01	2.561013760569930E+00	4.877775836782310E+00	4.648010883955390E+02	1.075929487230510E+10	1.832613550105840E+10
4.588777585784190E-01	2.261976958738840E+00	4.761152475129430E+00	4.481033723502880E+02	9.619101004692070E+09	1.631343962836150E+10
4.785761707109230E-01	1.9803086132121360E+00	4.647821069017550E+00	4.313005158657720E+02	8.557089373051820E+09	1.439842938254130E+10
4.982745828434270E-01	1.713584420221960E+00	4.537492094384250E+00	4.148734285293220E+02	7.589328369214940E+09	1.264208418137760E+10
5.179729949759310E-01	1.457959216148460E+00	4.429876027167130E+00	3.996812834465000E+02	6.726008563888260E+09	1.115126571746340E+10
5.376714071084350E-01	1.215627353698100E+00	4.32468334303760E+00	3.852738175965600E+02	5.964637171438560E+09	9.844257284317590E+09
5.57786570700220E-01	9.878931973599970E-01	4.219506084803310E+00	3.75003499030880E+02	5.271982121167630E+09	8.574841838376620E+09
5.778859070316100E-01	7.751486517583760E-01	4.116244252798800E+00	3.555424043261080E+02	4.644859928675660E+09	7.386177616086870E+09
5.979931569931980E-01	5.753772042113690E-01	4.014589919393420E+00	3.403230412296190E+02	4.081128703644750E+09	6.275220138643190E+09
6.181004069547860E-01	3.801903461857860E-01	3.914235156690330E+00	3.252535765968980E+02	3.577701913202510E+09	5.308536398561400E+09
6.382076569163730E-01	1.859865520515250E-01	3.814872036792700E+00	3.104866343186400E+02	3.131252442098540E+09	4.501008982377430E+09
6.572842562528320E-01	-1.895066028803550E-03	3.721238946385580E+00	2.969267202123000E+02	2.740849600462380E+09	3.891173209241970E+09
6.763608555892900E-01	-2.032949456984740E-01	3.627958313451950E+00	2.837105953642850E+02	2.369825344321360E+09	3.463779292212090E+09
6.954374549257480E-01	-4.252875829492340E-01	3.534767175455290E+00	2.701116939553850E+02	2.027287203963410E+09	3.156694260069740E+09
7.145140542622060E-01	-6.835362560574680E-01	3.441402569859070E+00	2.535966604776890E+02	1.707658582358010E+09	2.865255687578240E+09
7.335906535986650E-01	-9.818668004993730E-01	3.3476011534126760E+00	2.329107499576640E+02	1.409855964136200E+09	2.566140667350740E+09
7.526672529351230E-01	-1.283187977449590E+00	3.253101105721870E+00	2.107578500467990E+02	1.154289844134410E+09	2.272596656060350E+09
7.717438522715810E-01	-1.575204470207720E+00	3.157638322107860E+00	1.876356194660500E+02	9.373499691935020E+08	1.987118361991940E+09
8.00000000000000E-01	-1.936867726960520E+00	3.013910296242460E+00	1.550581011813660E+02	6.692866201481340E+08	1.602434712613360E+09
8.18750000000000E-01	-2.107559875105570E+00	2.916633785254180E+00	1.280411039062280E+02	5.212038566146320E+08	1.221283927203800E+09
8.37500000000000E-01	-2.166589245326670E+00	2.817547590923340E+00	1.08442774674810E+02	4.063952616728940E+08	9.889194206883120E+08
8.56250000000000E-01	-2.176064619564120E+00	2.716402026888100E+00	9.024852969278480E+01	3.186721637163970E+08	7.751606831391680E+08
8.75000000000000E-01	-2.161185304881360E+00	2.612947406786580E+00	7.475181186648510E+01	2.431716706194870E+08	6.070284079243430E+08
8.93750000000000E-01	-2.118517957471360E+00	2.506934044256920E+00	6.235473766708170E+01	1.797126983543760E+08	4.812214045891750E+08
9.12500000000000E-01	-2.048882314259700E+00	2.398112252937270E+00	5.229103879094490E+01	1.266707837437060E+08	3.823743441673430E+08
9.31249999999999E-01	-1.951426912022270E+00	2.286232346465750E+00	4.356608814326170E+01	8.398834841301580E+07	2.956271444698380E+08
9.50000000000000E-01	-1.815172386244970E+00	2.171044638480490E+00	3.574166082374840E+01	5.131655745823110E+07	2.153802449802300E+08
9.75000000000000E-01	-1.567929958032100E+00	2.011884002137300E+00	2.527474233141400E+01	2.194864735541660E+07	1.248458746327040E+08
1.00000000000000E+00	-1.242387706272960E+00	5.00000000000000E-01	5.407971821081970E+00	1.888459826881500E+05	1.920687333755170E+06

C.4 Elastodyn Inputs for Profile #4

Table C.4: ElastoDyn OpenFAST input data for chord length profile #4.

Blade Fraction r/R (-)	Twist Angle (deg)	Chord Length (m)	Mass Density (kg/m)	Flapwise Stiffness (Nm ²)	Edgewise Stiffness (Nm ²)
0.000000000000000E+00	1.559455301971170E+01	5.200000000000000E+00	3.179059159259060E+03	1.525336732671640E+11	1.524092444021610E+11
2.000000000000000E-02	1.559105026258910E+01	5.208280051053220E+00	2.844639124071310E+03	1.396059559125450E+11	1.371910901056170E+11
4.000000000000000E-02	1.542808288705690E+01	5.235714686841760E+00	2.505353762822230E+03	1.239755438005000E+11	1.211943594444680E+11
6.000000000000000E-02	1.498668187913840E+01	5.288938619667070E+00	2.150176072709730E+03	1.032257195889790E+11	1.030637624551030E+11
8.000000000000000E-02	1.432158034416250E+01	5.360587950371890E+00	1.807166613880170E+03	8.162835042138820E+10	8.436578661171380E+10
1.000000000000000E-01	1.348751138745820E+01	5.443298779798940E+00	1.689750275067180E+03	6.177531809788480E+10	6.862655814157260E+10
1.250000000000000E-01	1.229069721992210E+01	5.551024109038490E+00	1.296524292073250E+03	4.274720146392410E+10	5.134664996974550E+10
1.500000000000000E-01	1.102229252935760E+01	5.650144322056730E+00	9.822677239823060E+02	3.237301609568750E+10	3.898538145499410E+10
1.690340633511320E-01	1.007455100521850E+01	5.710964180985910E+00	7.966163346309950E+02	2.827287353472030E+10	3.195263357170140E+10
1.880681267022640E-01	9.194457415112660E+00	5.752111033293940E+00	6.645041811187670E+02	2.481852933449630E+10	2.695846118026080E+10
2.071021900533960E-01	8.429191400183100E+00	5.767237237684650E+00	5.764843213881020E+02	2.195610441457930E+10	2.376092222912670E+10
2.261362534045280E-01	7.777140178454870E+00	5.754540379641520E+00	5.250180685658330E+02	1.967142143571740E+10	2.208465213113590E+10
2.451703167556600E-01	7.182453068336750E+00	5.710000000000000E+00	4.938126520056330E+02	1.814591572823210E+10	2.117540078661550E+10
2.660887252285560E-01	6.526991264456790E+00	5.660000000000000E+00	4.770703368896240E+02	1.743838853733650E+10	2.122866609158050E+10
2.870071337014520E-01	5.894967665228040E+00	5.610000000000000E+00	4.773523868829210E+02	1.717978459127930E+10	2.21965663099440E+10
3.079255421743470E-01	5.294241247126910E+00	5.560000000000000E+00	4.911665826051680E+02	1.713932293875850E+10	2.370543987443030E+10
3.28843956472430E-01	4.734510589122640E+00	5.510000000000000E+00	5.078562949145650E+02	1.706678280133170E+10	2.509719400915350E+10
3.509110298069780E-01	4.200509221861600E+00	5.440000000000000E+00	5.20814752779300E+02	1.661330604071580E+10	2.584011698932500E+10
3.729781089667120E-01	3.725899877374300E+00	5.360000000000000E+00	5.256981352982320E+02	1.586056999189000E+10	2.576075213696910E+10
3.950451881264470E-01	3.306980159403290E+00	5.250976438933890E+00	5.180762008689010E+02	1.462995821019820E+10	2.443983152542070E+10
4.171122672861810E-01	2.919972991579770E+00	5.155426104351990E+00	5.110768758278300E+02	1.356308609067360E+10	2.310182481947970E+10
4.391793464459160E-01	2.561013760569930E+00	5.015210892552290E+00	4.913623323018480E+02	1.202411879866720E+10	2.048048993920620E+10
4.588777585784190E-01	2.261976958738840E+00	4.894194900762370E+00	4.734962599414290E+02	1.074017026213350E+10	1.821470832712680E+10
4.785761707109230E-01	1.980308613217360E+00	4.776766837000510E+00	4.556385859761220E+02	9.546949799856560E+09	1.606407015014190E+10
4.982745828434270E-01	1.713584420221960E+00	4.662613847593840E+00	4.380692366285480E+02	8.461699829541370E+09	1.409525538472340E+10
5.179729949759310E-01	1.457959216148460E+00	4.551423078869500E+00	4.219151121506900E+02	7.495143562855680E+09	1.242643934601560E+10
5.376714071084350E-01	1.215627353698100E+00	4.442881677154600E+00	4.066215238917430E+02	6.643940973556080E+09	1.096540534580930E+10
5.57786570700220E-01	9.878931973599970E-01	4.334495038943060E+00	3.909690759941340E+02	5.870586609274010E+09	9.548467827858870E+09
5.778859070316100E-01	7.751486517583760E-01	4.228210168106110E+00	3.751476781239520E+02	5.171235755373620E+09	8.223211543590960E+09
5.979931569931980E-01	5.753772042113690E-01	4.123694324170640E+00	3.590723004129650E+02	4.543195149120860E+09	6.985702182851560E+09
6.181004069547860E-01	3.801903461857860E-01	4.020614766663540E+00	3.431730550356650E+02	3.982780327509930E+09	5.909585216711150E+09
6.382076569163730E-01	1.859865520515250E-01	3.918638755117000E+00	3.276071853262190E+02	3.486094050247610E+09	5.011074936858500E+09
6.572842562528320E-01	-1.895066028803550E-03	3.822607604567520E+00	3.133239585606740E+02	3.051924968309620E+09	4.332805664090310E+09
6.763608555892900E-01	-2.032949456984740E-01	3.726986113464610E+00	2.994101562423800E+02	2.639357901546820E+09	3.857732919441060E+09
6.954374549257480E-01	-4.252875829492340E-01	3.631490129961870E+00	2.850962441650820E+02	2.258455293719930E+09	3.516646703225830E+09
7.145140542622060E-01	-6.835362560574680E-01	3.535835502218190E+00	2.677051198039240E+02	1.902949831507640E+09	3.192932055759260E+09
7.335906535986650E-01	-9.818668004993730E-01	3.439738078392470E+00	2.459808611355940E+02	1.571597066611320E+09	2.860532740868590E+09
7.526672529351230E-01	-1.283187977449590E+00	3.342913706643620E+00	2.225558267117360E+02	1.287138536835760E+09	2.534152708319890E+09
7.717438522715810E-01	-1.575204470207720E+00	3.245078235130510E+00	1.981713465067240E+02	1.045569531709650E+09	2.216536494888020E+09
8.000000000000000E-01	-1.936867726960520E+00	3.097701044380410E+00	1.637995941634450E+02	7.468766173660700E+08	1.788204009579250E+09
8.187500000000000E-01	-2.107559875105570E+00	2.997884618326650E+00	1.352743429082170E+02	5.817543872184220E+08	1.363165820193600E+09
8.375000000000000E-01	-2.166589245326670E+00	2.896140509635760E+00	1.145769792576990E+02	4.536721372399580E+08	1.103962642908170E+09
8.562500000000000E-01	-2.176064619564120E+00	2.792198912424540E+00	9.535528108955970E+01	3.557569229600630E+08	8.653682713204660E+08
8.750000000000000E-01	-2.161185304881360E+00	2.685790020809730E+00	7.897770303810800E+01	2.714429261704640E+08	6.776018230076580E+08
8.937500000000000E-01	-2.118517957471360E+00	2.576644028908120E+00	6.587073166584500E+01	2.005509978073300E+08	5.37026654306460E+08
9.125000000000000E-01	-2.048882314259700E+00	2.464491130836480E+00	5.522589621404030E+01	1.412887111920200E+08	4.265007027161630E+08
9.312499999999990E-01	-1.951426912022270E+00	2.349061520711570E+00	4.599351671982150E+01	9.360846950420260E+07	3.294886143210640E+08
9.500000000000000E-01	-1.815172386244970E+00	2.230085392650150E+00	3.771205592705550E+01	5.713055911763130E+07	2.397821371519010E+08
9.750000000000000E-01	-1.567929958032100E+00	2.065467418399750E+00	2.663897801663480E+01	2.43820044902370E+07	1.386870280179540E+08
1.000000000000000E+00	-1.242387706272960E+00	5.000000000000000E-01	5.407971821081970E+00	1.888459826881500E+05	1.920687333755170E+06

D | Supportive Figures for Blade Twist and Chord Length Redesign

D.1 Relative Wind Speed Variation

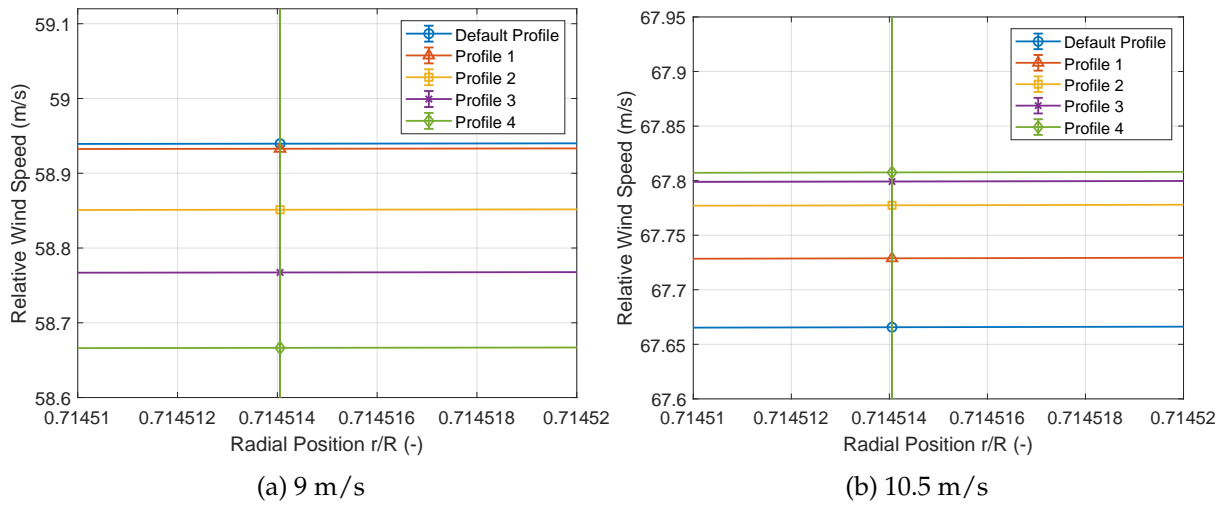


Figure D.1: Relative wind speed variation of the original and the redesigned FOWT at the radial position of 0.715, according to blade twist profile 2, chord length profile 2 and the combination of the two profiles, for wind speeds 9 m/s and 10.5 m/s. Blue curves: Original profiles, Orange curves: Blade twist profile 2. Yellow curves: Chord length profile 2. Purple curves: Combination of the two profiles.

D.2 Inflow Angle Variation

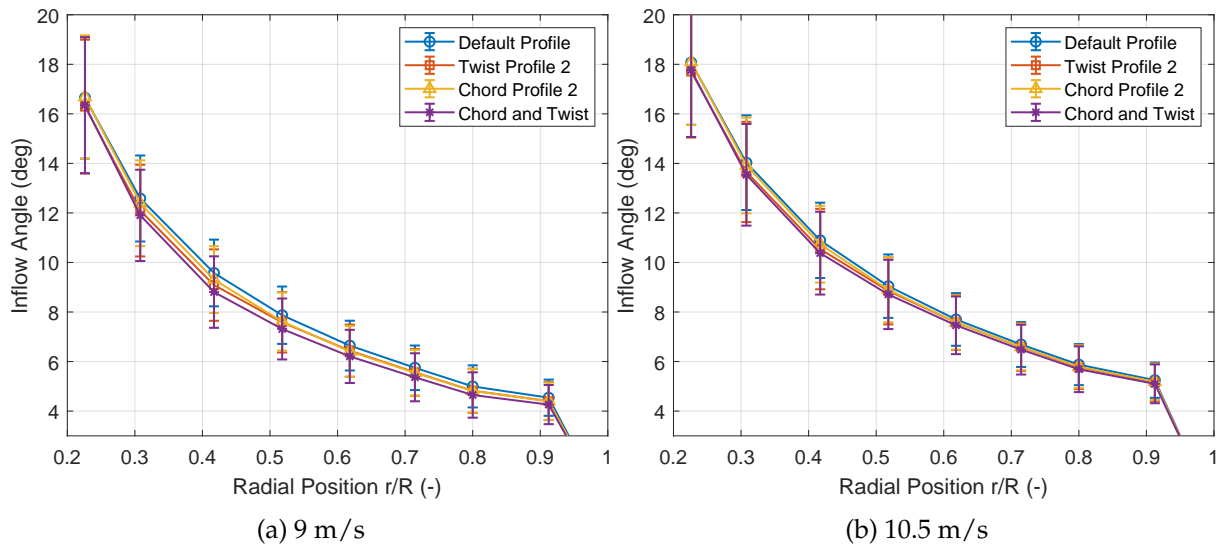


Figure D.2: Spanwise inflow angle variation of the original and the redesigned FOWT, according to blade twist profile 2, chord length profile 2 and the combination of the two profiles, for wind speeds 9 m/s and 10.5 m/s. Blue curves: Original profiles, Orange curves: Blade twist profile 2. Yellow curves: Chord length profile 2. Purple curves: Combination of the two profiles.

D.3 Axial Induction Factor Variation

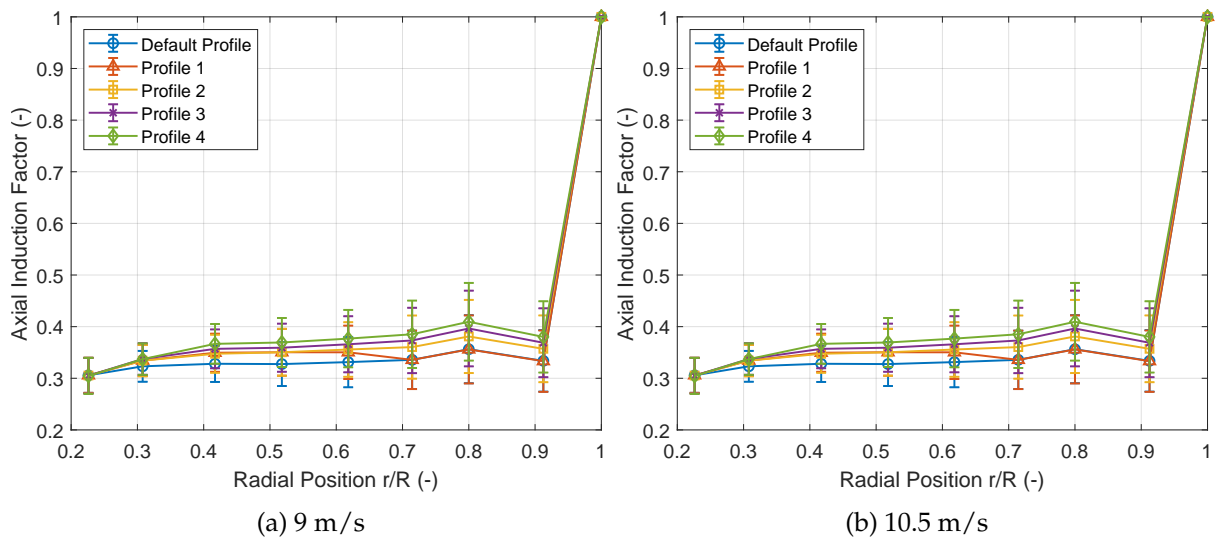


Figure D.3: Spanwise axial induction factor variation of the original and the redesigned FOWT, according to blade twist profile 2, chord length profile 2 and the combination of the two profiles, for wind speeds 9 m/s and 10.5 m/s. Blue curves: Original profiles, Orange curves: Blade twist profile 2. Yellow curves: Chord length profile 2. Purple curves: Combination of the two profiles.

D.4 Angle of Attack Variation

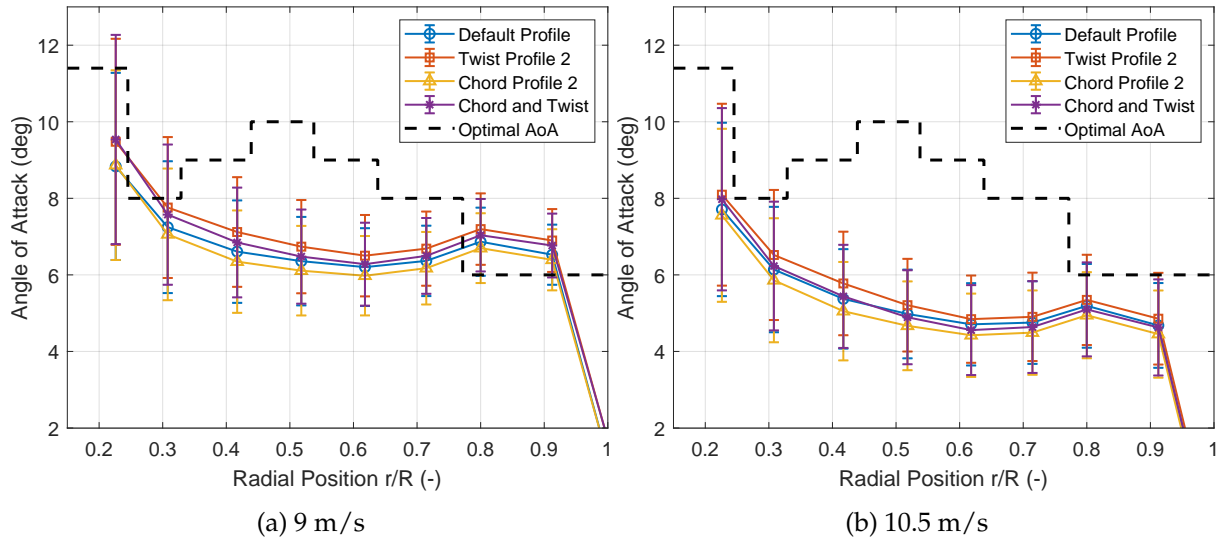


Figure D.4: Spanwise angle of attack variation of the original and the redesigned FOWT, according to blade twist profile 2, chord length profile 2 and the combination of the two profiles, for wind speeds 9 m/s and 10.5 m/s. Blue curves: Original profiles, Orange curves: Blade twist profile 2. Yellow curves: Chord length profile 2. Purple curves: Combination of the two profiles. Dashed black line: Spanwise optimal AoA.

D.5 Aerodynamic Torque and Thrust Variation

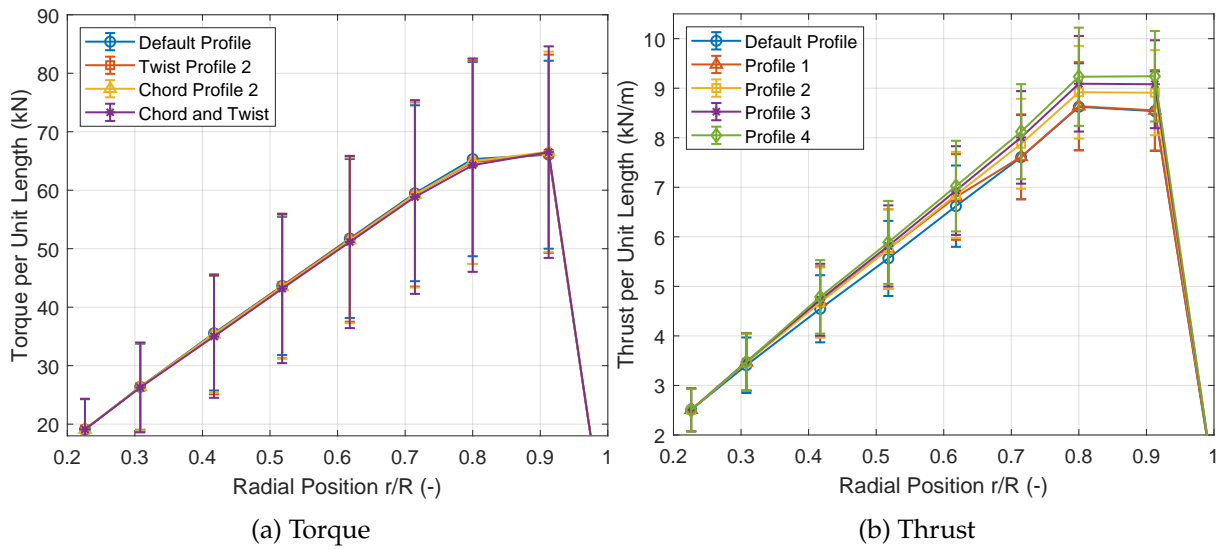


Figure D.5: Spanwise torque and thrust per unit length variation of the original and the redesigned FOWT, according to blade twist profile 2, chord length profile 2 and the combination of the two profiles, for a wind speed of 9 m/s. Blue curves: Original profiles, Orange curves: Blade twist profile 2. Yellow curves: Chord length profile 2. Purple curves: Combination of the two profiles.

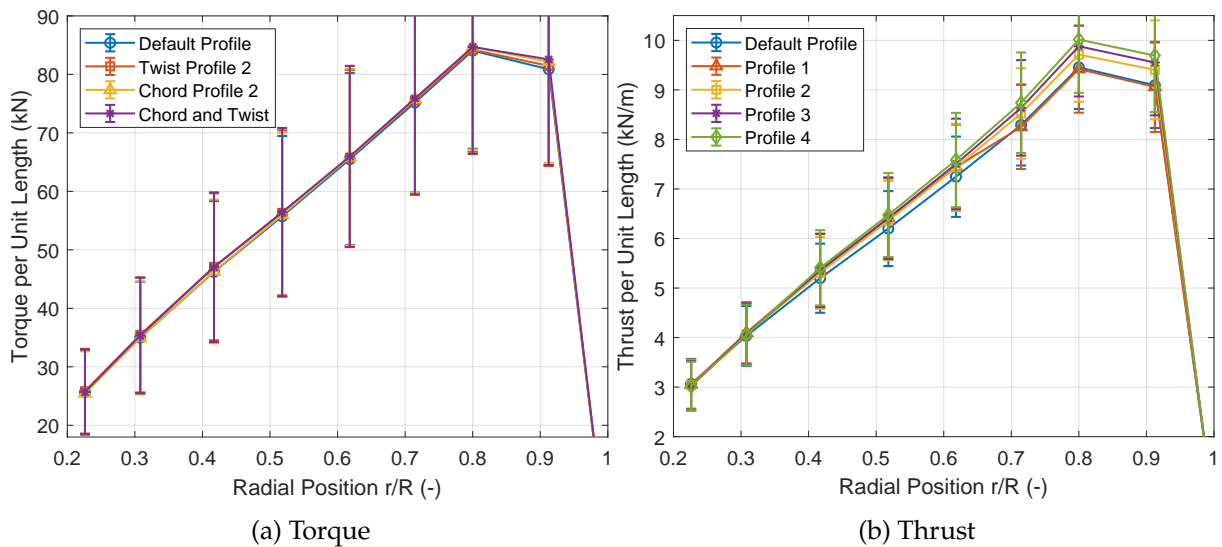


Figure D.6: Spanwise torque and thrust per unit length variation of the original and the redesigned FOWT, according to blade twist profile 2, chord length profile 2 and the combination of the two profiles, for a wind speed of 10.5 m/s. Blue curves: Original profiles, Orange curves: Blade twist profile 2. Yellow curves: Chord length profile 2. Purple curves: Combination of the two profiles.